



Norwegian University of  
Science and Technology

# Ductile-Brittle Transition in Offshore Steel

**Gry Myrmo Hellum**

Civil and Environmental Engineering

Submission date: June 2017

Supervisor: Odd Sture Hopperstad, KT

Co-supervisor: Tore Børvik, KT  
Sondre Bergo, KT


Norwegian University of Science and Technology  
Department of Structural Engineering





## MASTER THESIS 2017

SUBJECT AREA: Computational Mechanics	DATE: June 11, 2017	NO. OF PAGES: 9+82+3
--	---------------------	-------------------------

TITLE: <b>Ductile-Brittle Transition in Offshore Steel</b>	
BY:  Gry Myrmo Hellum	

### SUMMARY:

The main objective of this thesis was to investigate experimentally and numerically the main effects and interaction effects of temperature, strain rate and stress triaxiality on an offshore X65 steel.

During preliminary simulations smooth test specimens, and specimens with different round and sharp notches, were modelled using Abaqus/Standard and Abaqus/Explicit. The models were implemented with Johnson-Cook material model, and material parameters from a material expected to have similar values as the X65 steel of this thesis. Tension tests were run at quasi-static and dynamic simulations. The stress triaxiality and stress intensification factor  $R = \sigma_1/\sigma_0$  were found, and used to decide which specimens to use in the experimental work.

Further, a MATLAB model implemented with the Johnson-Cook material model, the Cockcroft-Latham failure criterion and the Ritchie-Knott-Rice brittle fracture criterion was made. Here the stress triaxiality, strain rate and maximum stress intensification were varied to see how this affected the ductile to brittle transition temperature.

Tension tests were performed experimentally to study the behaviour of the steel. Smooth specimens, specimens with round notches of radii 2.0 mm (R2) and 0.8 mm (R0.8) and sharp-notched specimens were used to see the effect of stress triaxiality. The effect of strain rate was studied through quasi-static tests and dynamic tests using split-Hopkinson tension bar. Tests were run at room temperature, -30°C, -60°C and -90°C. The specimens that showed the least ductile behaviour, were studied using Scanning Electron Microscope, but none of them had fractured due to cleavage.

The Johnson-Cook material parameters were calibrated for the steel, and simulations imitating the experimental tests were performed using Abaqus/Standard and Abaqus/Explicit. The stress and strain of the experimental and numerical results were compared. It turned out that the model was able to produce the same results as in the experiments for the smooth specimen and R2, but it overestimated the stress level for R0.8 and the V-notch.

At last the graphs with stress triaxiality, Cockcroft-Latham failure criterion and Ritchie-Knott-Rice fracture criterion were made and compared with the preliminary simulations.

The material turned out to have a higher yield strength and a higher ductility than the material from the preliminary work. The results showed that it obtained a less ductile behaviour for low temperatures, high strain rates and high values of stress triaxiality. A combination of the factors seemed to lead to interaction effects, giving even lower ductility. Although the material showed a less ductile behaviour with lower fracture strains, cleavage did not occur. Further studies are needed to find the maximum stress intensification, and to find the ductile to brittle transition.

RESPONSIBLE TEACHER: Professor Odd Sture Hopperstad

SUPERVISOR(S): Professor Odd Sture Hopperstad, professor Tore Børvik and PhD Candidate Sondre Bergo

CARRIED OUT AT: SIMLab, The Department of Structural Engineering, NTNU





## MASTEROPPGAVE 2017

FAGOMRÅDE: Beregningsmekanikk	DATO: 11. juni 2017	ANTALL SIDER: 9+82+3
----------------------------------	------------------------	-------------------------

TITTEL:

**Overgang fra duktil til sprø oppførsel for offshore stål**

UTFØRT AV:

Gry Myrmo Hellum



SAMMENDRAG:

Hovedmålet med denne avhandlingen var å undersøke eksperimentelt og numerisk hovedeffektene og interaksjonseffektene temperatur, tøyningshastighet og spenningsstriaksialitet har på et offshore X65 stål.

Under innledende simuleringer ble glatte prøvestykker og prøvestykker med forskjellige runde og skarpe kjerver modellert i Abaqus/Standard og Abaqus/Explicit. Modellene var implementert med Johnson-Cook material modell, og materialparametere fra et materiale som var forventet å ha samme egenskaper som stålet som ble undersøkt i denne avhandlingen. Strekktester ble kjørt i kvasi-statiske og dynamiske simuleringer. Spenningsstriaksialiteten og spenningsintensiveringsfaktoren  $R = \sigma_1/\sigma_0$  ble funnet, og brukt til å bestemme hvilke prøvestykker som skulle bli brukt i det eksperimentelle arbeidet.

Videre ble det laget en MATLAB-modell, som var implementert med Johnson-Cook material modell, Cockcroft-Latham bruddkriterium og Ritchie-Knott-Rice sprøbruddkriterium. I modellen ble spenningsstriaksialiteten, tøyningshastigheten og den maksimale spenningsintensiveringsfaktoren  $R_{max}$  variert, for å se hvordan dette påvirker den duktile til sprø omslagstemperaturen.

Strekktester ble utført eksperimentelt for å studere oppførselen til stålet. Glatte prøver, prøver med kjerver med radier 2,0 mm (R2) og 0,8 mm (R0.8) og prøver med skarpe kjerver ble brukt for å se effekten av triaksialitet. Effekten av tøyningshastighet ble undersøkt ved kvasi-statiske tester og dynamiske tester. De dynamiske testene brukte split-Hopkinson tension bar. Testene ble utført ved romtemperatur, -30 °C, -60 °C og -90 °C. Prøvestykkene som viste minst duktil oppførsel, ble studert med Scanning Electron Microscope. Det viste seg at ingen av prøvene hadde oppnådd sprøtt brudd.

Johnson-Cook materialparameterne ble kalibrert for stålet, og simuleringer som etterlignet eksperimentene ble kjørt i Abaqus/Standard og Abaqus/Explicit. Spenning og tøyning fra eksperimentene og de numeriske simuleringene ble sammenlignet. Det viste seg at modellen klarte å gi de samme resultatene som eksperimentene for de glatte prøvestykkene og R2, men overestimerte spenningene for R0.8 og prøven med skarp kjerv.

Til slutt ble grafer med spenningsstriaksialitet, Cockcroft-Latham bruddkriterium og Ritchie-Knott-Rice bruddkriterium laget, og sammenliknet med de innledende simuleringene.

Materialet viste seg å ha høyere flytespenning og høyere duktilitet enn materialet fra de innledende simuleringene. Resultatene viste en mindre duktil oppførsel for lave temperaturer, høye tøyningshastigheter og høye spenningsstriaksialiteter. Det virket som om en kombinasjon av disse faktorene førte til interaksjonseffekter, som ga en enda mindre duktil oppførsel. Selv om materialet viste en mindre duktil oppførsel med lavere bruddtøyninger, oppstod det ikke sprøtt brudd. Videre studier er nødvendig for å finne den maksimale spenningsintensiveringsfaktoren, og for å finne overgangen fra duktil til sprøtt brudd.

FAGLÆRER: Professor Odd Sture Hopperstad

VEILEDER(E): Professor Odd Sture Hopperstad, professor Tore Børvik og stipendiat Sondre Bergo

UTFØRT VED: SIMLab, Institutt for konstruksjonsteknikk, NTNU



## **MASTER'S THESIS 2017**

for

*Gry Myrmo Hellum*

### **Ductile-Brittle Transition in Offshore Steel**

Under normal circumstances, most steels have good ductility, i.e., large plastic deformations may develop before fracture occurs in the material. However, it is well known that steels have a transition temperature, and for temperatures lower than this, brittle fracture is the predominant fracture mode. Brittle fracture implies that fracture occurs without significant plastic deformations. Other parameters that affect the transition from ductile to brittle fracture is stress state and strain rate. High stress triaxiality and high strain rate will promote brittle fracture. In this study, the transition from ductile to brittle fracture of an offshore steel is studied through quasi-static and dynamic tests in the laboratory at various temperatures and stress conditions. The latter is achieved by using notches specimens. The experiments are complemented with numerical simulations using the nonlinear finite element (FE) code ABAQUS.

The objective is to investigate experimentally the main effects and interaction effects of temperature, strain rate and stress triaxiality on the ductility of an offshore steel. The tests are conducted in a universal tensile machine at quasi-static strain rate and in the split-Hopkinson tension bar (SHTB) at high strain rate. In both cases, a temperature chamber is used to obtain low temperature, while smooth and notched tensile specimens are employed to vary the stress triaxiality. Nonlinear FE simulations with ABAQUS are used to define appropriate specimen geometries and to evaluate simple fracture criteria for the ductile-brittle transition.

The main tasks of the research project are as follows:

1. Literature study on fracture of steels with emphasis on the ductile-brittle transition, including models for ductile and brittle fracture.
2. Numerical study with ABAQUS is used to design the tensile specimens to obtain the desired levels of stress triaxiality, adopting simple ductile and brittle fracture criteria.
3. Experimental study on the main effects and interaction effects of temperature, strain rate and stress triaxiality on the ductility of an offshore steel.
4. Parameter identification of material model (elastic/plastic) and failure criteria (ductile/brittle) based on the experimental data.
5. Numerical study on the influence of the model parameters on the predicted ductility.

*Supervisors:* Odd Sture Hopperstad, Tore Børvik, Sondre Bergo (NTNU)

The thesis must be written according to current requirements and submitted to the Department of Structural Engineering, NTNU, no later than June 11<sup>th</sup>, 2017.

NTNU, January 15<sup>th</sup>, 2017.

Odd Sture Hopperstad  
Professor





---

## Preface

This thesis was written at the Structural Impact Laboratory (SIMLab), located at the Department of Structural Engineering at the Norwegian University of Science and Technology (NTNU). It was written the spring 2017 to fulfil the degree Master of Science, after 5 years at the master programme Civil and Environmental Engineering.

## Acknowledgements

I want to thank Tore Andre Kristensen, Engineer at SINTEF for conducting the quasi-static tension tests, and to thank Trond Auestad, Senior Engineer at SIMLab for conducting the dynamic tension test.

Further, I would like to thank PhD Candidate Christian Oen Paulsen from the Department of Materials Science and Engineering, for providing pictures of the fractures surfaces of several specimens using Scanning Electron Microscope.

The MATLAB script was made in collaboration with Piraveena Gunathasan, who also used the script for her Master thesis. I want to thank her for the collaboration, and for discussions and help trough the semester.

I would like to express my gratitude to my supervisors, professor Odd Sture Hopperstad, professor Tore Børvik and PhD Candidate Sondre Bergo. Their weekly guidance has been essential, and whenever I went to their offices, I got help.

*Gry Hellum*

Gry Hellum, June 11, 2017, Trondheim

---

## Abstract

The main objective of this thesis was to investigate experimentally and numerically the main effects and interaction effects of temperature, strain rate and stress triaxiality on an offshore X65 steel.

During preliminary simulations smooth test specimens, and specimens with different round and sharp notches, were modelled using Abaqus/Standard and Abaqus/Explicit. The models were implemented with Johnson-Cook material model, and material parameters from a material expected to have similar values as the X65 steel of this thesis. Tension tests were run at quasi-static and dynamic simulations. The stress triaxiality and stress intensification factor ( $R = \sigma_1/\sigma_0$ ) were found, and used to decide which specimens to use in the experimental work.

Further, a MATLAB model implemented with the Johnson-Cook material model, the Cockcroft-Latham failure criterion and the Ritchie-Knott-Rice brittle fracture criterion was made. Here the stress triaxiality, strain rate and maximum stress intensification were varied to see how this affected the ductile to brittle transition temperature.

Tension tests were performed experimentally to study the behaviour of the steel. Smooth specimens, specimens with round notches of radii 2.0 mm (R2) and 0.8 mm (R0.8) and sharp-notched specimens were used to see the effect of stress triaxiality. The effect of strain rate was studied through quasi-static tests and dynamic tests using split-Hopkinson tension bar. Tests were run at room temperature,  $-30^\circ\text{C}$ ,  $-60^\circ\text{C}$  and  $-90^\circ\text{C}$ . The specimens that showed the least ductile behaviour, were studied using Scanning Electron Microscope, but none of them had fractured due to cleavage.

The Johnson-Cook material parameters were calibrated for the steel, and simulations imitating the experimental tests were performed using Abaqus/Standard and Abaqus/Explicit. The stress and strain of the experimental and numerical results were compared. It turned out that the model was able to produce the same results as in the experiments for the smooth specimen and R2, but it overestimated the stress level for R0.8 and the V-notch.

At last the graphs with stress triaxiality, Cockcroft-Latham failure criterion and Ritchie-Knott-Rice fracture criterion were made and compared with the preliminary simulations.

The material turned out to have a higher yield strength and a higher ductility than the material from the preliminary work. The results showed that it obtained a less ductile behaviour for low temperatures, high strain rates and high values of stress triaxiality. A combination of the factors seemed to lead to interaction effects, giving even lower ductility. Although the material showed a less ductile behaviour with lower fracture strains, cleavage did not occur. Further studies are needed to find the maximum stress intensification, and to find the ductile to brittle transition.

# CONTENTS

---

<b>1</b>	<b>Introduction</b>	<b>1</b>
1.1	Motivation . . . . .	1
1.2	Objective . . . . .	1
1.3	Scope . . . . .	2
1.4	Overview of Thesis . . . . .	2
<b>2</b>	<b>Theory</b>	<b>5</b>
2.1	Plasticity . . . . .	5
2.1.1	Von Mises Yield Criterion . . . . .	5
2.1.2	Engineering and True Stress and Strain . . . . .	6
2.1.3	The Notch Effect . . . . .	7
2.1.4	Work Hardening . . . . .	8
2.1.5	The Johnson-Cook Material Model . . . . .	8
2.2	Fracture Mechanisms . . . . .	10
2.2.1	Ductile Fracture . . . . .	10
2.2.2	Cleavage . . . . .	11
2.2.3	Ductile to Brittle Transition . . . . .	12
2.3	Failure Criteria . . . . .	14
2.3.1	The Johnson-Cook Fracture Criterion . . . . .	14
2.3.2	The Cockcroft-Latham Failure Criterion . . . . .	14
2.3.3	Ritchie-Knott-Rice Fracture Criterion . . . . .	15
<b>3</b>	<b>Preliminary Simulations</b>	<b>17</b>
3.1	Abaqus Simulations . . . . .	17
3.1.1	Material Model . . . . .	17
3.1.2	Geometry . . . . .	18
3.1.3	Mesh . . . . .	19
3.1.4	Boundary Conditions . . . . .	22
3.1.5	Results and discussion . . . . .	22
3.2	Analytical MATLAB Model . . . . .	30
3.2.1	Establishing the Model . . . . .	30
3.2.2	Transition Temperature . . . . .	32

<b>4</b>	<b>Experimental Work</b>	<b>39</b>
4.1	Quasi-Static Tension Tests . . . . .	40
4.1.1	Setup . . . . .	40
4.1.2	Results . . . . .	43
4.2	High Strain Rate Tension Tests . . . . .	48
4.2.1	Setup . . . . .	48
4.2.2	Results . . . . .	50
4.3	Scanning Electron Microscope . . . . .	55
4.4	Summary and Discussion . . . . .	57
<b>5</b>	<b>Numerical Simulations</b>	<b>63</b>
5.1	Calibrating the Johnson-Cook Material Model . . . . .	63
5.1.1	Strain Hardening Term . . . . .	63
5.1.2	Strain Rate Sensitivity Constant . . . . .	64
5.1.3	Temperature Sensitivity Constant . . . . .	67
5.2	Simulations . . . . .	68
5.2.1	Results and discussion . . . . .	68
<b>6</b>	<b>Concluding Remarks</b>	<b>77</b>
6.1	Summary and Conclusions . . . . .	77
6.2	Further Work . . . . .	79
	<b>References</b>	<b>80</b>
<b>A</b>	<b>Appendix</b>	<b>83</b>
A.1	Analytical MATLAB Model . . . . .	83





# NOMENCLATURE

---

$\beta_{TQ}$	Taylor-Quinney coefficient
$\dot{p}$	Equivalent plastic strain rate
$\dot{p}^*$	Dimensionless plastic strain rate
$\dot{p}_0$	Reference strain rate
$\dot{p}_{ad}$	Adiabatic limit strain rate
$\dot{p}_{iso}$	Isothermal limit strain rate
$\nu$	Poisson's ratio
$\omega$	Weighting function
$\rho$	Density
$\sigma^*$	Stress triaxiality
$\sigma_0$	Yield stress
$\sigma_{cr}$	Critical stress of Ritchie Knott Rice fracture criterion
$\sigma_{eq}$	Equivalent stress
$\sigma_e$	Engineering stress
$\sigma_f$	Critical stress of Ritchie Knott Rice fracture criterion
$\sigma_h$	Hydrostatic stress
$\sigma_{ij}$	Stress tensor
$\sigma_i$	Principal stresses, $i = 1, 2, 3$
$\sigma_t$	True stress
$\varepsilon^e$	Elastic strain
$\varepsilon^p$	Plastic strain
$\varepsilon_e$	Engineering strain

## Contents

---

$\varepsilon_l$	Logarithmic (true) strain
$\varepsilon_{lu}^p$	Equivalent plastic strain at the onset of necking
$\varepsilon_l^p$	Logarithmic (true) plastic strain
$\varphi(\sigma_{ij})$	Yield function
$A$	Constant of Johnson-Cook Material model
$A$	Cross-section area
$a$	Cross-sectional radius at neck
$A_0$	Initial cross-section area
$B$	Constant of Power hardening law
$C$	Strain rate sensitivity constant of Johnson-Cook material model
$C_i$	Constant of Voce hardening rule
$c_\varepsilon$	Heat capacity
$D$	Damage
$D_i$	Johnson-Cook fracture constants, $i = 1, 2, 3, 4, 5$
$D_x$	Cross-sectional diameter in thickness direction
$D_y$	Cross-sectional diameter in transverse direction
$dW_p$	Plastic work increment per unit volume
$E$	Young's modulus
$F$	Force
$f$	Yield criterion
$J_2$	Second invariant of $\sigma_{ij}$
$L$	Gauge length
$L$	Lode parameter
$L_0$	Initial gauge length
$m$	Temperature sensitivity constant of Johnson-Cook material model
$n$	Constant of Power hardening law
$p$	Equivalent plastic strain
$p_f$	Fracture strain



$Q_i$	Constant of Voce hardening rule
$R$	Hardening variable
$R$	Notch radius
$R$	Stress intensification
$R_{max}$	Maximum value of the stress intensification
$T$	Temperature
$T^*$	Homologous temperature
$T_0$	Reference temperature
$T_m$	Melting temperature
$W_c$	Cockcroft-Latham fracture parameter

# INTRODUCTION

---

## 1.1 Motivation

Under normal circumstances, most steels have a ductile behaviour. This means that they can obtain large amounts of plastic deformation before fracture occurs. At lower temperatures steels behave less ductile, and at a given temperature the material has a transition where the predominant fracture mode changes from ductile to brittle. A brittle fracture is a fracture that occurs with almost no plastic deformation, and therefore without any warning. This fracture mode is therefore important to prevent.

Offshore pipelines are from time to time subjected to impact loads from anchors, trawl gear, etc. The Petroleum Safety Authority Norway has published a list of reports on damage to and incidents in connection with pipeline systems the North Sea and the Norwegian Sea (Petroleumstilsynet, 2017). In the Arctic regions, the temperatures may stabilize at very low values. An anchor hitting a steel pipe in these regions, may lead to a brittle fracture if the wrong material is used.

Another example where low temperatures may occur is when transporting liquid nitrogen. Liquid nitrogen has a boiling temperature of  $-196^{\circ}\text{C}$ . Spilling it leads to a huge temperature decrease in the material hit, and may lead to a temporary brittle behaviour.

Other parameters that affects the ductile to brittle transition are the strain rate and the stress state. Large strain rates reduce the ductility, and may be obtained from collisions or explosions. A triaxial state of tensile stress also reduces the ductility, and may be obtained from cracks due to defects.

## 1.2 Objective

The objective of this thesis is to investigate experimentally the main effects and interaction effects of temperature, strain rate and stress triaxiality on the ductility of an offshore steel.

The sub-objectives are as follows:

1. Literature study on fracture of steels with emphasis on the ductile-brittle transition, including models for ductile and brittle fracture.

### 1.3. Scope

---

2. Numerical study with ABAQUS to design the tensile specimens with the desired levels of stress triaxiality.
3. Experimental study on the main effects and interaction effects of temperature, strain rate and stress triaxiality on the ductility of an offshore steel.
4. Parameter identification of material model (elastic/plastic) and failure criteria (ductile/brittle) based on the experimental data.
5. Numerical study on the influence of the model parameters on the predicted ductility.

## 1.3 Scope

1. The experimental work was performed on only one material, namely the X65 steel.
2. The experimental tests were only performed on four different geometries. Geometries with fatigue cracks were not used.
3. Only tension tests were performed. No fracture mechanics tests (e.g Charpy V-notch tests) or component tests were executed.
4. The tests were only done at a given set of temperatures. The lowest temperature at the quasi-static test was  $-90^{\circ}\text{C}$ . At dynamic tests, the lowest temperature was  $-60^{\circ}\text{C}$ .

## 1.4 Overview of Thesis

A brief description of each chapter of this thesis is found below.

**Chapter 2: Theory** Chapter 2 gives an overview of the plasticity theory used in this thesis, and describes ductile and brittle fracture mechanisms and fracture criteria.

**Chapter 3: Preliminary Simulations** In Chapter 3 quasi-static and dynamic tensile tests were simulated using Abaqus. A MATLAB script implemented with ductile and brittle fracture criteria was created to study the effects of stress triaxiality, strain rate and temperature. The material data used was expected to have similar properties as the material studied in this thesis.

**Chapter 4: Experimental Work** Chapter 4 explains the procedure, and discuss the results of the quasi-static and dynamic tension tests carried out in this thesis.

**Chapter 5: Numerical Simulations** In Chapter 5 the parameters of the Johnson-Cook Material Model are calibrated and used to simulate the experimental work using Abaqus. The results of the simulations are compared with the experimental results. The triaxiality and different fracture criteria are also studied.

**Chapter 6: Concluding Remarks** In Chapter 6 the most important results and conclusions of the thesis are summarised, and further work is suggested.



## 2.1 Plasticity

Figure 2.1.1 shows a typical engineering stress versus engineering strain curve from a tension test. In the start, the material behaves elastic, and the stress increases linearly. When the stress reaches the yield stress, the material gets a plastic behaviour. The stress continues to increase until diffuse necking. Henceforth it is implied that necking means diffuse necking. At necking, the deformation starts to localize, resulting in a no longer uni-axial stress state. Afterwards the force needed to deform the test specimen will decrease until fracture.

### 2.1.1 Von Mises Yield Criterion

The deformation of a specimen is elastic until the stresses reach the yield stress, and plastic deformation occur. As long as the response is elastic, the specimen returns to it's original form when it is unloaded. A general formulation of the yield criterion is

$$f = \varphi(\sigma_{ij}) - \sigma_0 = 0 \quad (2.1.1)$$

where  $f$  is the yield function,  $\varphi$  is the equivalent stress and  $\sigma_0$  is the yield stress. If  $f < 0$ , the material is in the elastic domain. When  $f = 0$  the material responds

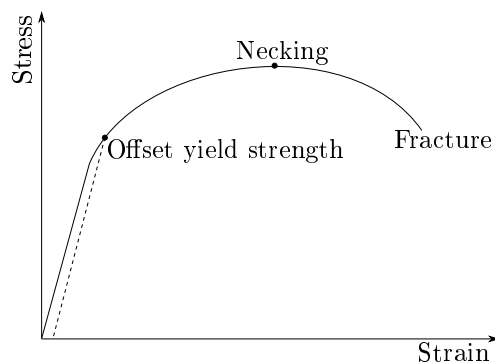


Figure 2.1.1: Typical engineering stress versus engineering strain curve

plastically.

For a situation of combined stresses, the yielding can be related to a combination of the principal stresses. Von Mises suggested that yielding occur when the second invariant of the stress deviator  $J_2$  exceeded some critical value (Dieter, 1988). This led to  $\varphi = \frac{1}{\sqrt{2}}[(\sigma_1 - \sigma_2)^2 + (\sigma_2 - \sigma_3)^2 + (\sigma_3 - \sigma_1)^2]^{\frac{1}{2}}$ , giving von Mises yield criterion:

$$\sigma_0 = \frac{1}{\sqrt{2}}[(\sigma_1 - \sigma_2)^2 + (\sigma_2 - \sigma_3)^2 + (\sigma_3 - \sigma_1)^2]^{\frac{1}{2}} \quad (2.1.2)$$

This criterion is independent of the component of hydrostatic stress, and the square terms makes it independent of the sign of individual stresses.

In a state of uniaxial tension the stress state is  $(\sigma_{11}, 0, \dots, 0)$ . If the equivalent stress is defined as the von Mises stress, the yielding starts when  $\sigma_{11} = \sigma_0$ .

### 2.1.2 Engineering and True Stress and Strain

After a tensile test, the results are often given as force and displacement. The engineering stress and engineering strain can be found by using the formulas below:

$$\sigma_e = \frac{F}{A_0} \quad (2.1.3)$$

$$\varepsilon_e = \frac{\Delta L}{L_0} \quad (2.1.4)$$

Where  $\sigma_e$  is the engineering stress,  $F$  is the force in the test machine,  $A_0$  is the initial cross-section area of the gauge area of the test specimen,  $\varepsilon_e$  is the engineering strain and  $L_0$  is the initial length of the gauge area. The engineering stress versus engineering strain curve is used to provide basic design information on the strength of materials. Yield strength, ultimate tensile strength, breaking stress and engineering strain at fracture are examples of parameters found from the engineering stress-strain curve.

In most materials, there is a gradual transition from elastic to plastic behaviour, and it can be hard to decide the yield strength. A common technique is to use the offset yield strength. This strength is determined by finding the stress at the intersection of the stress-strain curve and a line parallel to the elastic part of the curve offset by a specified strain (Dieter, 1988).

$$\sigma_0 = \frac{F_{(\text{strain offset}=0.002)}}{A_0} \quad (2.1.5)$$

The engineering stress versus engineering strain curve does not give a true indication of the characteristics of the material, since it is based on the materials original dimension. The true stress  $\sigma_t$  and logarithmic (true) strain  $\varepsilon_l$  are based on the actual cross-section area, and are given by:

$$\sigma_t = \frac{F}{A} \quad (2.1.6)$$

$$\varepsilon_l = \ln\left(\frac{L}{L_0}\right) = \ln\left(\frac{A_0}{A}\right) \quad (2.1.7)$$

### 2.1.3 The Notch Effect

Some of the test specimens used in this thesis have a notch in the gauge area. According to Dieter (1988) a notch has four important consequences that increases the probability of brittle fracture. It creates a local stress concentration at the root of the notch. It creates a triaxial tensile state of stress. It creates a locally concentrated strain and strain hardening that can lead to ductile void formation where the voids can be converted into brittle cracks. It creates a local strain rate that is much higher than the average strain rate. More about ductile and brittle fracture can be read in section 2.2 Fracture mechanisms.

The notch effect is also found at the diffuse neck of a smooth specimen in a tensile test. The radial and the transverse stresses in the triaxial stress state raise the value of the longitudinal stress required to cause plastic flow. The longitudinal true stress is not equal to the equivalent stress, and needs to be corrected for the triaxial effect. Bridgman (1944) made a mathematical analysis that makes this correction. The equivalent stress after necking is given by

$$\sigma_{eq} = \frac{\sigma_t}{(1 + 2R/a) \ln(1 + a/2R)} \quad (2.1.8)$$

where  $R$  is the notch radius and  $a$  is the specimen radius at the neck. Le Roy et al. (1981) proposed an empirical expression for  $a/R$  where

$$a/R = 1.1(p - \varepsilon_{lu}^p), \quad p > \varepsilon_{lu}^p \quad (2.1.9)$$

In this expression  $p$  is the equivalent plastic strain, and  $\varepsilon_{lu}^p$  is the equivalent plastic strain at the onset of necking. Bridgman's analysis is based on the following assumptions (Dieter, 1988):

- The contour of the neck is approximated by the arc of a circle.
- The cross section of the necked region remains circular through the test.
- The von mises' criterion for yielding applies.
- The strains are constant over the cross section of the neck.



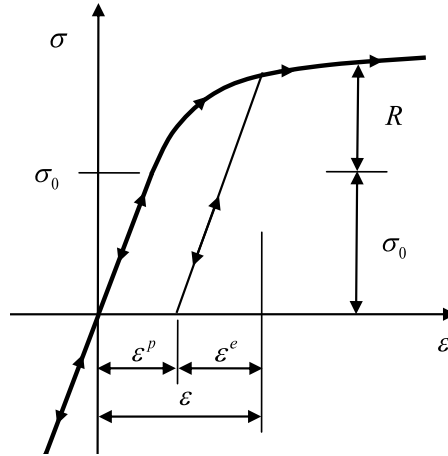


Figure 2.1.2: Stress versus strain curve showing the work hardening, (Hopperstad and Børvik, 2015)

### 2.1.4 Work Hardening

Figure 2.1.2 shows how steel can harden when deformed plastically. The yield criterion below (Hopperstad and Børvik, 2015) describes this behaviour:

$$f = \sigma_{eq} - (\sigma_0 + R) = 0 \quad (2.1.10)$$

$R$  is a hardening variable. For a uniaxial tension test, von Mises yield criterion is simplified to  $f = |\sigma_1| - (\sigma_0 + R)$  which leads to  $|\sigma_1| = \sigma_0 + R$ .

Power law and Voce rule, are two frequently used rules describing the work-hardening. Power law is given by

$$R(p) = Bp^n \quad (2.1.11)$$

where  $p$  is equivalent plastic strain, and  $B$  and  $n$  are constants. Voce rule is given by:

$$\sum_{n=1}^{N_R} Q_i(1 - \exp(-C_i p)) \quad (2.1.12)$$

where  $Q_i$  and  $C_i$  are constants.

### 2.1.5 The Johnson-Cook Material Model

Equation (2.1.10) gives a description of the work hardening of metals, but does not take into account the effect of rate dependence and temperature. The faster a material is loaded, the stronger it becomes, see Figure 2.1.3. The rate dependence increases with temperature, but the temperature also affects the yield stress and

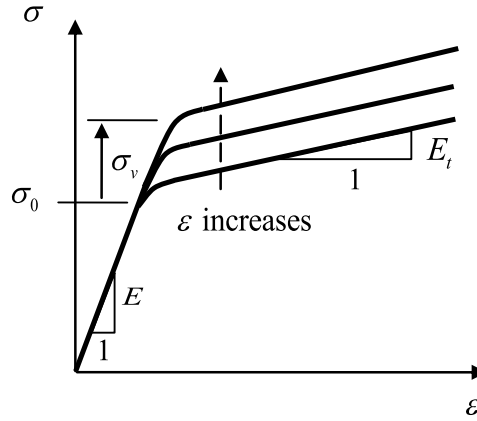


Figure 2.1.3: Effect of rate dependence, (Hopperstad and Børvik, 2015)

work hardening. These values decrease with increasing temperature. At the melting temperature the yield stress is zero, and the material has lost its load-carrying capacity.

Johnson and Cook (1983) suggested an empirical constitutive relation for metals subjected to large strains, high strain rates and high temperatures:

$$\sigma_{eq} = (A + Bp^n)(1 + C \ln \dot{p}^*)(1 - (T^*)^m) \quad (2.1.13)$$

$A$ ,  $B$ ,  $C$ ,  $n$  and  $m$  are constants to be determined. Further,  $p$  is the equivalent plastic strain.  $\dot{p}^* = \dot{p}/\dot{p}_0$  is the dimensionless plastic strain rate, where  $\dot{p}_0$  is the reference strain rate.  $T^*$  is the homologous temperature given by  $T^* = (T - T_0)/(T_m - T_0)$ , where  $T$  is the temperature,  $T_m$  is the melting temperature and  $T_0$  is the reference temperature. The first bracket in the model represents the strain hardening, where  $A$  denotes the yield stress, and  $Bp^n$  the work hardening described by power law. The second bracket describes the strain-rate sensitivity, and the third represents the temperature softening. This implies that the Johnson-Cook model assumes that the strain hardening, strain-rate hardening and temperature softening are independent of each other.

In processes with high strain rate the heat generated by plastic dissipation does not have time to diffuse. There is no thermal loss to the surroundings, and the temperature will increase locally at regions with high deformation (Hopperstad and Børvik, 2017). This is called adiabatic conditions, and the temperature increase is called adiabatic heating. The adiabatic heating is given by the differential equation

$$dT = \frac{\beta_{TQ}}{\rho c_\varepsilon} dW_p = \frac{\beta_{TQ}}{\rho c_\varepsilon} \sigma_{eq} dp \quad (2.1.14)$$

where  $\rho$  is the mass density,  $c_\varepsilon$  is the heat capacity and  $dW_p$  is the plastic work increment per unit volume and can be written as the equivalent stress multiplied

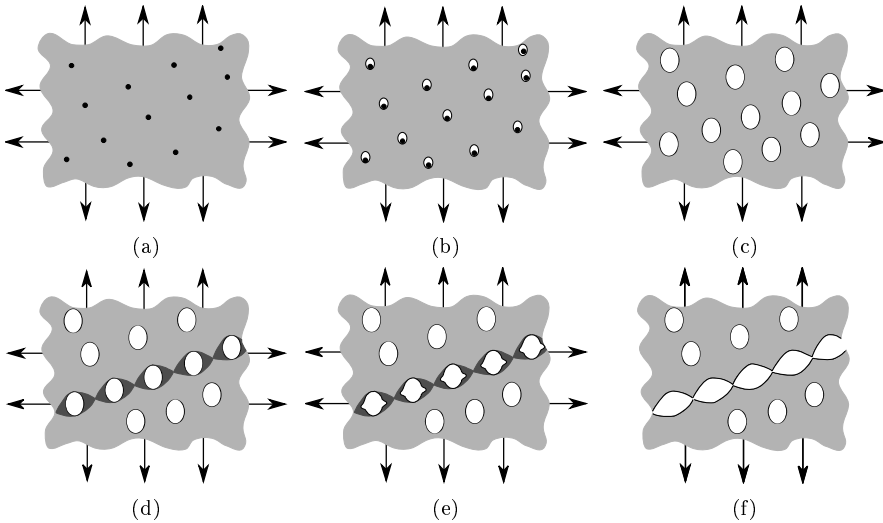


Figure 2.2.1: Void nucleation, growth and coalescence in ductile metals: (a) inclusions in a ductile matrix, (b) void nucleation, (c) void growth, (d) strain localization between voids, (e) necking between voids, and (f) void coalescence and fracture. Adapted from Anderson (2005).

with the strain increment.  $\beta_{TQ}$  is the Taylor-Quinney coefficient. This value varies with the strain rate, and it is normal to give it the value  $\beta_{TQ} = 0$  for low strain rates and  $\beta_{TQ} = 0.9$  for high strain rates. By dividing the deformation into strain increments, the temperature,  $T_{k+1}$ , at the next strain increment can be found by using the trapezoidal rule for numerical integration

$$T_{k+1} = T_k + \frac{1}{2} \frac{\beta_{TQ}}{\rho c_\varepsilon} (\sigma_{eq,k+1} + \sigma_{eq,k})(p_{k+1} - p_k) \quad (2.1.15)$$

where  $\sigma_{eq,k}$  is the equivalent stress at strain increment  $k$ . Assuming small plastic strain increments,  $\sigma_{eq,k+1}$  can be given by

$$\sigma_{eq,k+1} = (A + Bp_{k+1}^n) \left( 1 + C \ln \left( \frac{\dot{p}}{\dot{p}_0} \right) \right) \left( 1 - \left( \frac{T_k - T_0}{T_m - T_0} \right)^m \right) \quad (2.1.16)$$

By using this method, the temperature lags one step behind the equivalent stress and the equivalent plastic strain. This is sufficiently accurate for small plastic strain increments.

## 2.2 Fracture Mechanisms

### 2.2.1 Ductile Fracture

According to Anderson (2005), ductile fracture is characterized by void nucleation, growth and coalescence. The process is illustrated in Figure 2.2.1. When materials

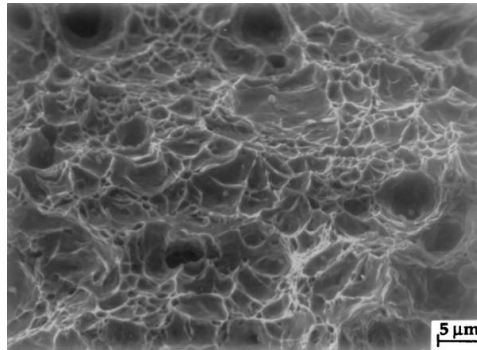


Figure 2.2.2: SEM fractograph of ductile fracture in a low carbon steel. (Anderson, 2005)

that contain impurities are applied a sufficient load, the interfacial bonds between the particles/inclusions and the matrix breaks or the particles crack. This forms voids, and if the particles are well-bounded to the matrix, fracture will follow soon. Otherwise the fracture properties are controlled by void growth and coalescence. Plastic strain and hydrostatic stress causes the voids to grow. As the voids grows, neighbouring voids interact, local necking occurs between the voids, they coalescence and the material fractures.

The fracture surface after a ductile fracture is typically a dimpled surface, see Figure 2.2.2. The "cup and cone" is also commonly observed after an uniaxial tensile test. Here the neck produces a triaxial stress state in the centre of the specimen. This leads to a penny-shaped ductile fracture in the middle. At the outer ring, there are fewer and smaller voids due to lower hydrostatic stress. Here the cross section will fail due to shear fracture, resulting in a fracture surface oriented  $45^\circ$  from the tensile axis.

### 2.2.2 Cleavage

Anderson (2005) defines cleavage, or brittle fracture, as a rapid propagation of a crack along a particular crystallographic plane. Under normal circumstances steel fail as a consequence of ductile fracture. If the plastic flow is restricted, it is harder for the steel to behave ductile, and cleavage may occur. The susceptibility to cleavage is increased by almost any factor that increases the yield strength. Some of the factors are low temperature, a triaxial stress state, radiation damage, high strain rate and strain aging.

To initiate cleavage, the local stress ahead of the crack must be sufficient to overcome the cohesive strength of the material. The macroscopic crack does not provide sufficient stress concentration alone, so there must be a local discontinuity ahead of the crack that provides sufficient stress. An example of a local discontinuity is a sharp microcrack. A microcrack can for instance form by intersecting slip planes by means of dislocation, interaction or if an inclusion or second-phase par-

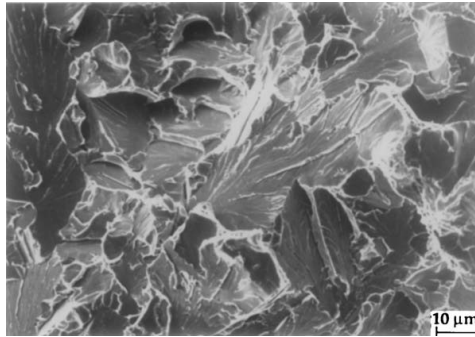


Figure 2.2.3: SEM fractograph of cleavage in a low-alloy steel. (Anderson, 2005)

ticle crack as a consequence of the plastic strain in the surrounding matrix. Since the location of a particle large enough to nucleate cleavage is random, a critical stress over a finite volume ahead of the macroscopic crack is necessary to nucleate cleavage. This volume is equal to the volume of two grains.

Figure 2.2.3 shows the fracture surface after cleavage fracture. The surface is multifaceted, and each facet corresponds to a single grain. The picture also shows a river-pattern, which also is characteristic for cleavage fracture. The pattern looks like multiple lines that convert into a single line.

### 2.2.3 Ductile to Brittle Transition

The probability of brittle fracture in steels can change drastically over a small temperature range. This change is called the ductile - brittle transition, and is illustrated in Figure 2.2.4. For low temperatures, the fracture will be pure cleavage. As the temperature increases and enter the transition region, both ductile and brittle fracture can occur in the same specimen. In the upper part of the region, the crack will start to grow by ductile tearing. While the crack is growing, more material is sampled near the crack tip. Eventually, the crack samples a critical particle, and cleavage occurs. For high temperatures the fracture will be ductile.

The temperature where the fracture changes from ductile to brittle is called the transition-temperature. Figure 2.2.4 shows the various definitions of this temperature according to Dieter (1988).

- *Fracture transition plastic* (FTP) is based on  $T_1$  and is the most conservative criterion. At this value, the fracture changes from partly brittle to pure ductile.
- *Fracture-appearance transition temperature* (FATT) is based on  $T_2$ . Here the fracture is 50 % brittle and 50 % ductile.
- The criterion based on  $T_3$  is found by taking the average of the upper and lower shelf values,  $T_1$  and  $T_5$ .

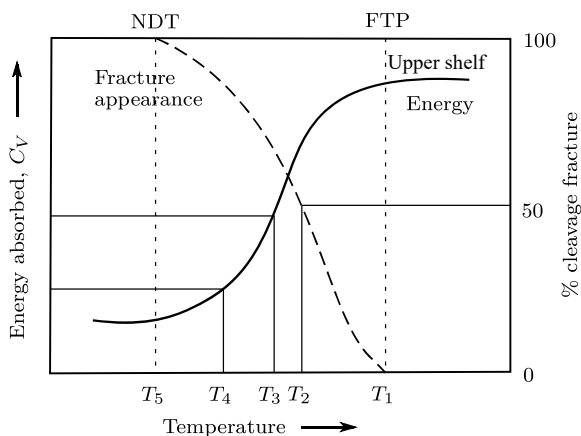


Figure 2.2.4: Various criteria of transition temperature (Dieter, 1988)

- *Ductility transition temperature* is a common criterion that is based on  $T_4$ . At this temperature the energy absorbed,  $C_v$ , must be equal to an arbitrary low value. For instance, a 20 J  $C_v$  transition temperature is an accepted criterion for low-strength ship steels.
- *Nil ductility temperature* (NDT) is a well-defined criterion based on  $T_5$ . This is the temperature where the fracture becomes pure brittle.

According to Dieter (1988) there are many factors affecting the transition temperature of steel. Some of these are mentioned below. The chemical composition has a great influence. The largest changes are found by varying the amount of carbon and manganese. The 20 J transition temperature for a specimen can for instance be raised by  $14^\circ\text{C}$  for each increase of 0.1 % carbon. Increasing the manganese by 0.1 % raises the transition temperature about  $5^\circ\text{C}$ . By going to higher Mn:C ratios, it is possible to decrease the transition temperature with about  $50^\circ\text{C}$ . Extending the Mn:C over 7:1 can lead to problems due to other factors, and should be avoided. The content of phosphorus also has a great influence on the transition temperature. It is raised by  $7^\circ\text{C}$  for each 0.01 %. Nickel in amounts up to 2 % lowers the transition temperature, while silicon and molybdenum raise it. Increasing the oxygen level increases the transition temperature, while deoxidizing the steel by silicon and aluminium gives a transition temperature around  $-60^\circ\text{C}$ .

The grain size is another important factor. Increasing the ferrite grain size decreases the transition temperature. Decreasing the austenite grain size also lower the transition temperature.

## 2.3 Failure Criteria

### 2.3.1 The Johnson-Cook Fracture Criterion

Johnson and Cook (1985) presented a fracture criterion that considers stress triaxiality, strain rate sensitivity and temperature softening. In this criterion, a damage  $D$  is defined, and fracture is assumed to occur when  $D$  reaches a critical value;  $D_{cr}$ . Most often, the value  $D_{cr} = 1$  is used. The damage is defined as:

$$D = \int_0^{p_f} \frac{1}{p_f} dp \quad (2.3.1)$$

where  $p_f$  is the strain at fracture and is given by

$$p_f = [D_1 + D_2 \exp(-D_3 \sigma^*)][1 + D_4 \ln p^*][1 + D_5 T^*] \quad (2.3.2)$$

$D_1, D_2, D_3, D_4, D_5$  are constants to be determined.  $\sigma^* = \sigma_H / \sigma_{eq}$  is the stress triaxiality where  $\sigma_H = \frac{1}{3}(\sigma_1 + \sigma_2 + \sigma_3)$  is the hydrostatic stress. Note that in the original model  $D_3$  is positive. Here a negative version is used, since it is given as negative in the Abaqus implementation of the model.

### 2.3.2 The Cockcroft-Latham Failure Criterion

Cockcroft and Latham (1968) presented a ductile fracture criterion which takes both the stress triaxiality and the Lode parameter into account. In this criterion, the damage is given by:

$$D = \frac{W}{W_c} = \frac{1}{W_c} \int_0^p \max(\sigma_1, 0) dp \quad (2.3.3)$$

By expressing  $\sigma_1$  in terms of invariants, the damage becomes

$$D = \frac{1}{W_c} \int_0^p \max\left(\sigma^* + \frac{3-L}{3\sqrt{3+L^2}}, 0\right) \sigma_{eq} dp \quad (2.3.4)$$

where  $W_c$  is the fracture parameter. The fracture parameter is said to be the "plastic work" to failure, and is calculated using the maximum principal stress. In the equation above,  $\sigma^*$  is the stress triaxiality and  $L$  is the Lode parameter given by

$$L = \frac{2\sigma_2 - \sigma_1 - \sigma_3}{\sigma_1 - \sigma_3} \quad (2.3.5)$$

In a uni-axial tension test  $L = -1$ , while it is 1 in a state of compression and 0 in a state of shear (Hopperstad and Børvik, 2017).

By using the Johnson-Cook constitutive relation to decide  $\sigma_{eq}$ , the criterion will depend on strain rate and temperature. The criterion has only one parameter to determine,  $W_c$ . This makes it easy to calibrate and widely used.

### 2.3.3 Ritchie-Knott-Rice Fracture Criterion

Ritchie et al. (1973) found a criterion for brittle fracture, where the material had to have a critical tension,  $\sigma_f$ , over a volume of two grain diameters ahead of a macroscopic crack tip for cleavage to occur. The magnitude of the maximum achievable stress depends on the yield stress and hardening properties. If the maximum achievable stress is less than  $\sigma_f$ , cleavage will not occur. Ritchie et al. (1973) defined the stress intensification  $R = \frac{\sigma_1}{\sigma_0}$ . If the maximum possible stress intensification was equal to a given value,  $\sigma_1$  would be close to  $\sigma_f$ , and cleavage would occur. For their material  $R_{max} = 5$  lead to cleavage.





# PRELIMINARY SIMULATIONS

---

In this thesis, tensile tests with different specimens were used to study the effects temperature, strain rate and stress triaxiality have on the ductility of a offshore steel. Before the experimental work, preliminary numerical simulations were performed to see which impact the geometry of the test specimen, the temperature and the strain rate had on the triaxiality and the stress intensification factor. This would be used to decide which specimens that would be used in the experimental work.

In the first part of the preliminary simulations, various test specimens were studied using Abaqus/Standard for quasi-static simulations and Abaqus/Explicit for dynamic simulations. In the second part, a MATLAB script implemented with ductile and brittle fracture criteria was made.

## 3.1 Abaqus Simulations

### 3.1.1 Material Model

The material used in this thesis is a X65 grade steel, which is a steel often used in offshore pipes. It is quite similar to the material used by Kristoffersen (2014), but while his tests were taken from pipes that were manufactured seamlessly using the Mannesmann effect, these specimens were taken from pipes that were formed from plates rolled into pipes and welded longitudinally. In this chapter, it is assumed that the material has the same properties as the material used by Kristoffersen (2014). These are shown in Table 3.1.1. The values of  $D_5$ ,  $m$  and  $T_m$  were not given, and were assumed to be  $D_5 = 1$ ,  $m = 1$ ,  $T_m = 1800$  K. The reference temperature  $T_0$  was set to 293 K.

In the quasi-static simulations, the material was described using the density  $\rho$ , the elastic constants Young's modulus  $E$  and Poisson's ratio  $\nu$  and with the Johnson-Cook material model. In the Johnson-Cook material model the values of  $A$ ,  $B$  and  $n$  were used. The dynamic model also had these properties, but it was described with some additional properties. In the Johnson-Cook material model the temperature sensitivity constant  $m$ , the melting temperature  $T_m$  and the transition temperature  $T_0$  were included. The material was modelled as a rate dependent material with strain rate sensitivity  $C$  and reference strain rate  $\dot{\rho}_0$ . The specific heat  $c_\epsilon$  and the inelastic heat fraction (Taylor-Quinney coefficient)  $\beta_{TQ}$

Table 3.1.1: Constants for the material model

Elastic constants and density				
$E$ [MPa]	$\nu$	$\rho$ [kg/m <sup>3</sup> ]		
208 000	0.3	7 800		
Johnson-Cook hardening				
$A$ [MPa]	$B$ [MPa]	$n$	$C$	$\dot{p}_0$ [1/s]
456.6	410.8	0.4793	0.0104	0.000806
Fracture strain constants				
$D_1$	$D_2$	$D_3$	$D_4$	$D_5$
0.42	2.25	1.87	-0.00239	1
Adiabatic heating and temperature softening				
$c_\varepsilon$ [mm <sup>2</sup> /s <sup>2</sup> K]	$\beta_{TQ}$	$T_m$ [K]	$T_0$ [K]	$m$
$452 \cdot 10^6$	0.9	1 800	293	1

were defined and the Johnson-Cook failure criterion was used with the constants  $D_1$ ,  $D_2$ ,  $D_3$ ,  $D_4$  and  $D_5$  and the values  $T_m$ ,  $T_0$  and  $\dot{p}_0$ .

### 3.1.2 Geometry

Figure 3.1.1 illustrates the geometry of the tensile specimens studied in the simulations. All the specimens were cylindrical, but to reduce the computational running time, they were modelled as axisymmetric deformable shells. This simplification made it possible to only draw a section of the specimens. Abaqus only had to do computations on this section, and then use axisymmetry to get the right values. This simplification assumed that all the loads and deformations were symmetric.

The specimens had an outer diameter of 5 mm and a diameter of 3 mm in the gauge area. Because an aim of these simulations was to study the effect of triaxiality, different specimens were modelled. The smooth specimen in Figure 3.1.1a was expected to have low triaxiality, while the specimens with round notches were expected to have high triaxialities and the specimens with sharp notches even higher. The round notches had radiuses of 0.4 mm, 0.8 mm and 2.0 mm. Henceforth these will be called R0.4, R0.8 and R2.0. The sharp notch will be called V-notch in some of the results. For manufacturing reasons the side faces of the notches in specimen R0.4 and R0.8 were inclined with a angle  $\alpha = 17.5^\circ$ . In Abaqus, the sharp notches were studied with different angles  $\alpha$ . The original length of the specimens was 35 mm, but 9 mm on each side was used to clamp the specimens to the testing-machines. In addition to this most of the deformation happened at the middle of the specimen's length, where the cross-section was smaller. Because of this, and to reduce the computational running time, the specimens were modelled

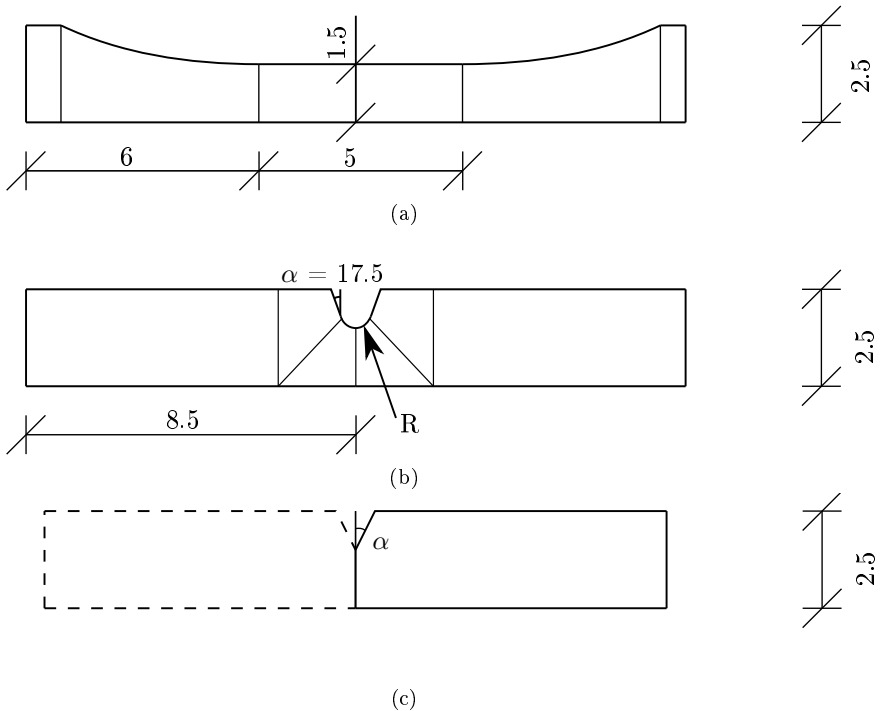


Figure 3.1.1: Geometry of the tensile specimens modelled.

with shorter lengths. For the specimens with sharp notches symmetry was used to reduce the length, and computational running time even more.

### 3.1.3 Mesh

The models were meshed as illustrated in Figure 3.1.2. To make the mesh structured and the elements in approximately quadratic shape, the models were partitioned as in Figure 3.1.1 and a structured mesh was used. The elements were modelled as 4-node bilinear axisymmetric quadrilateral with reduced integration and hourglass control (CAX4R).

To decide the mesh size, parameter studies concerning the effect the mesh has on the force versus displacement curves and on the stress intensification  $R = \sigma_1/\sigma_0$ , where  $\sigma_0 = 478$  MPa, were performed. Figure 3.1.3 shows the force versus displacement curve for dynamic tests of notched R0.4 specimens with 5, 15, 25 and 35 elements over the thickness in the gauge area. The mesh in the gauge area is illustrated in Figure 3.1.4. There is a big change between the force versus displacement curve of 5 and 15 elements over the thickness. More elements led to longer computational time but also more accurate results. 25 and 35 elements have almost

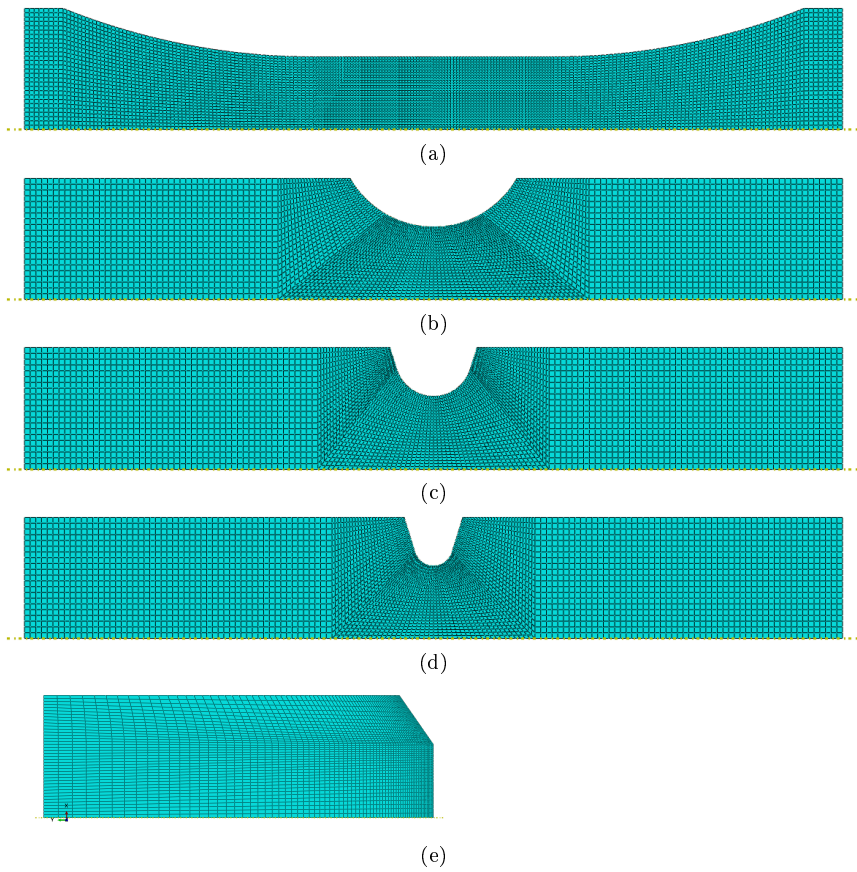


Figure 3.1.2: Mesh of tension test specimens: (a) smooth specimen, (b) R2.0, (c) R0.8, (d) R0.4 and (e) sharp notch.

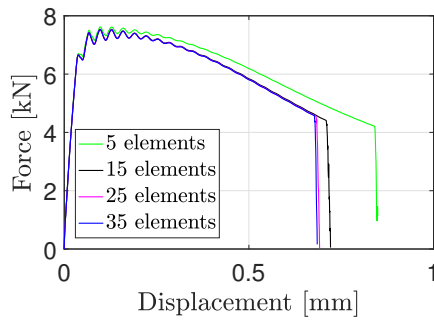


Figure 3.1.3: Force versus displacement for dynamic simulations of a R0.4 specimen with varying mesh.

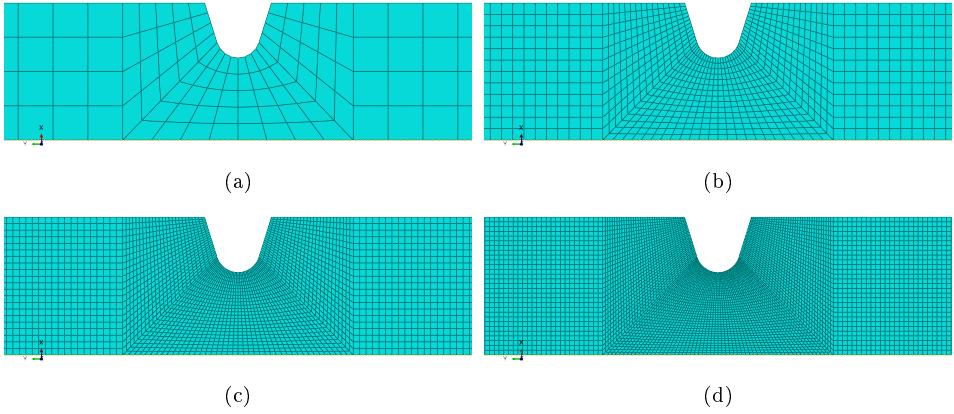


Figure 3.1.4: Mesh-study of R0.4 specimen. Inner radius divided into: (a) 5 elements, (b) 15 elements, (c) 25 elements and (d) 35 elements.

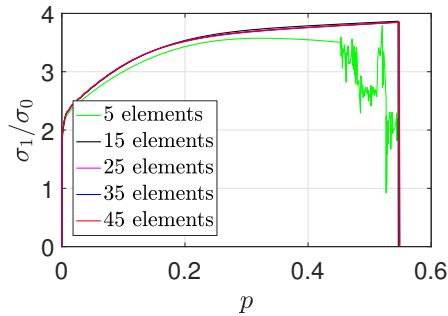


Figure 3.1.5: Stress intensification versus equivalent plastic strain for dynamic simulations of a R0.4 specimen with varying mesh.

the same curves, and a mesh with 25 elements over the thickness was chosen. This gave an element size of approximately  $0.06 \times 0.06 \text{ mm}^2 = 0.0036 \text{ mm}^2$ .

In the studies concerning the effect the mesh has on the stress intensification, 5 to 45 elements over the thickness in the gauge area were tested, see Figure 3.1.5. 5 elements gave lower stress intensification than the other curves, but the rest of the curves looked almost identical. 25 elements over the thickness were decided to be a reasonable size of the mesh.

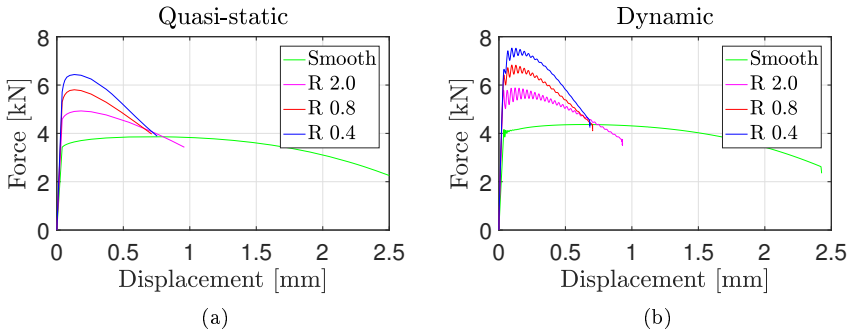


Figure 3.1.6: Force versus displacement curves for smooth specimen and specimen R2.0, R0.8 and R0.4 for (a) quasi-static and (b) dynamic analyses.

#### 3.1.4 Boundary Conditions

Boundary conditions giving axisymmetric properties were used in the symmetry axis to be sure that the specimens would deform the right way. In one end the specimen was fixed against displacement in the longitudinal direction and rotation. For the specimens with sharp notch, symmetry was used in the end representing the specimen instead. At the other end a load was applied. For quasi-static analyses this load was applied as a displacement in the longitudinal direction. By adjusting the time step for this displacement, the velocity of the load was set to 4 mm/s. In the dynamic analyses the load was applied as a velocity of 5000 mm/s. In explicit simulations, abrupt changes of velocity will introduce stress waves. These are artificial unless the velocity is the same as in the experiment. To avoid this, the velocity was ramped up at the start of the simulation. 10 % of the time period was used to ramp up the velocity. In the dynamic simulation, adiabatic heating was included. A predefined temperature field of 293 K was also added.

#### 3.1.5 Results and discussion

##### Force displacement

Figure 3.1.6 shows force versus displacement curves for the smooth specimen and specimen R2.0, R0.8 and R0.4 for (a) quasi-static and (b) dynamic analyses. For the dynamic simulations, a fracture criterion was used, and the curves were stopped at fracture. The quasi-static simulations were used without a fracture criterion, and the curves were stopped at approximately the same displacement as the fracture in the dynamic simulations. The curves show that the force is higher for the dynamic simulations than the quasi-static simulations. The notched specimens have higher force than the smooth, and when the notch radius decreases, the force increases. The notched specimens are also less ductile than the smooth.

Figure 3.1.7 shows the same curves for the specimens with sharp notches. The simulations were performed with notches of  $\alpha = 25$ ,  $\alpha = 35$  and  $\alpha = 45$ . These

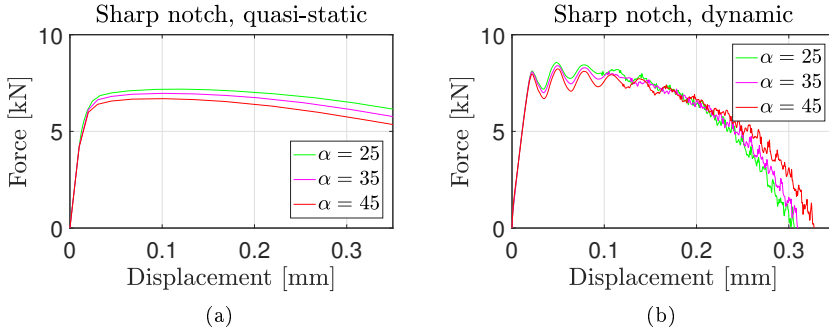


Figure 3.1.7: Force versus displacement curves for specimens with sharp notches of angle  $\alpha = 25^\circ$ ,  $\alpha = 35^\circ$  and  $\alpha = 45^\circ$  for (a) quasi-static and (b) dynamic analyses.

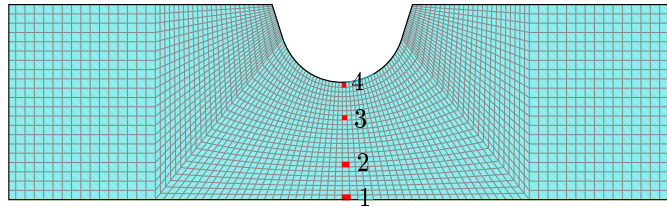


Figure 3.1.8: The four elements where the stress intensification factor and the stress triaxiality were studied.

curves also indicate that sharper notches leads to a stronger and less ductile response.

### Stress intensification factor

The stress intensification factor  $R_{max} = \sigma_1/\sigma_0$ , where  $\sigma_0 = 478$  MPa, was found in four elements spread over the cross-section of the gauge area. These elements are illustrated in Figure 3.1.8. Element number 1 is at the centre of the cross section, and element 4 is at the surface of the specimen. The factor was found for equivalent plastic strain up to 0.5, since cleavage was expected to happen at low values of strain.

Figure 3.1.9 shows the stress intensification factor  $R$  for the smooth specimen and specimen R2.0, R0.8 and R0.4 for quasi-static and dynamic simulations. These results show higher values for dynamic simulations than quasi-static, and the notched specimens have higher values than the smooth specimens.  $R$  is highest in the middle of the cross-section. The maximum value of element number 1 varies from approximately 2 for a smooth specimen in a dynamic simulation to nearly 4 for a R0.4 notched specimen at a dynamic simulation. The value  $R_{max}$  that leads to cleavage, is not determined for this material. A value of 3 would have resulted in



### 3.1. Abaqus Simulations

---

cleavage in both R0.8 and R0.4. If the value is about 4, specimen R0.4 would not be far away from cleavage at a dynamic simulation. If the value is about 5, fracture would not have been predicted by the chosen fracture model. At the surface of the specimen the highest value of  $R$  varies from 1.5 to 2. These are much lower values than in the centre of the specimen, and for tension tests corresponding to these simulations, cleavage was not expected to be initiated around element number 4.

Figure 3.1.10 shows the results for the V-notched specimens. The quasi-static results are not much higher than the results of R0.4, but the dynamic test reaches a stress intensification of 5. This is a value that was expected to lead to cleavage. The specimens were simulated at angles  $\alpha$  of  $25^\circ$ ,  $35^\circ$  and  $45^\circ$ . At the quasi-static simulations  $\alpha = 25^\circ$  gives the highest  $R$  while for dynamic simulations  $\alpha = 45^\circ$  gives the highest value. The values for the different angles are almost the same, and due to manufacturing reasons specimens with  $\alpha = 45^\circ$  was chosen to be produced to the experimental tests. A large angle would also make it easier to use lasers and other techniques to measure the diameter of the specimens during the tests.

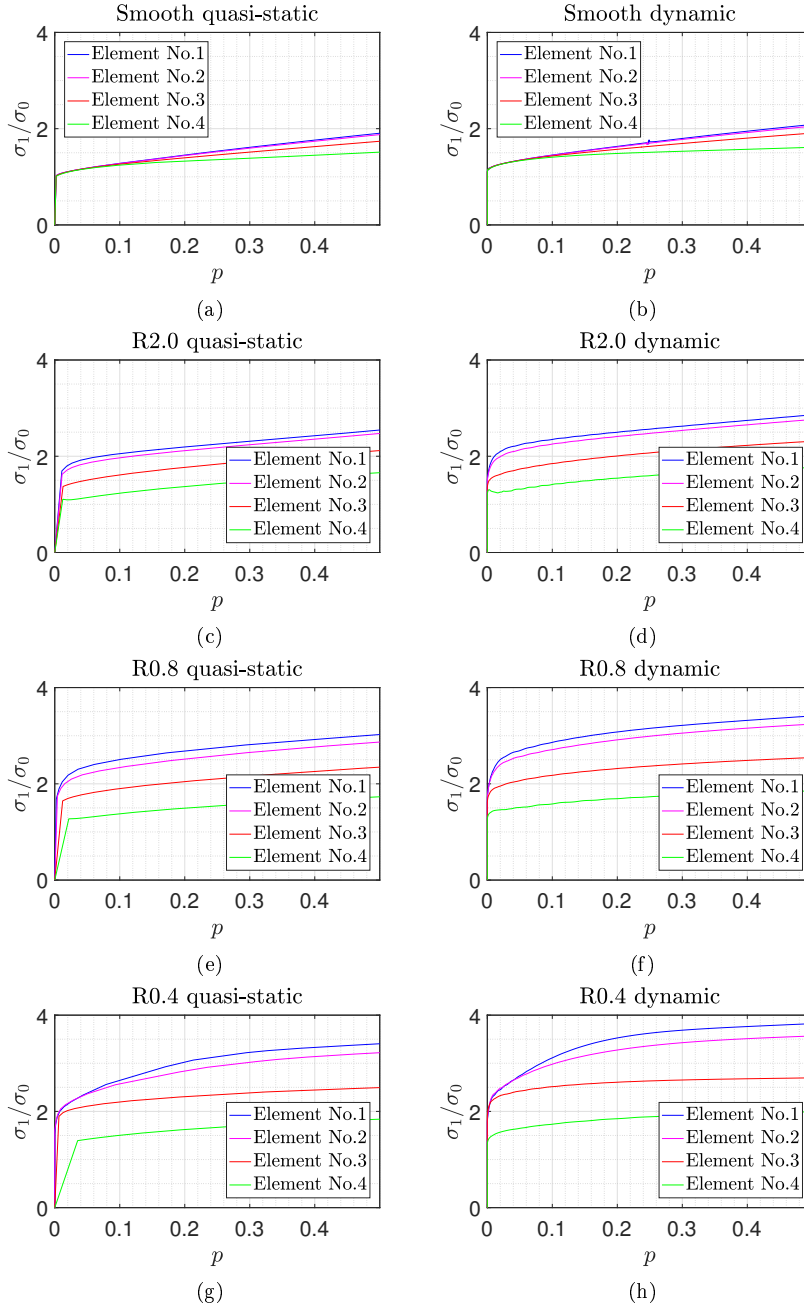


Figure 3.1.9: Stress intensification factor versus equivalent plastic strain for the different specimens at quasi-static and dynamic analyses.

### 3.1. Abaqus Simulations

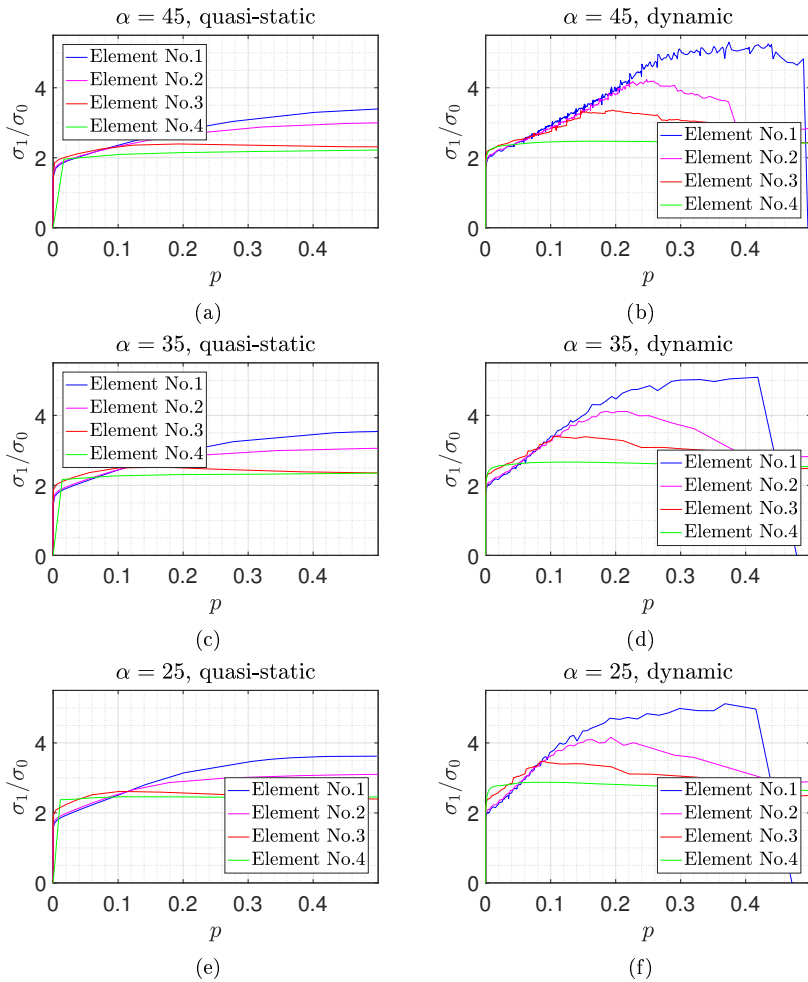


Figure 3.1.10: Stress intensification factor versus equivalent plastic strain for the V-notched specimens with an angle  $\alpha$  of  $45^\circ$ ,  $35^\circ$  and  $25^\circ$  at quasi-static and dynamic analyses.

Table 3.1.2

Specimen	Maximum stress triaxiality	
	Quasi-static	Dynamic
Smooth	0.53	0.55
R2.0	0.99	0.99
R0.8	1.34	1.32
R0.4	1.55	1.60
V, $\alpha = 45$	1.52	2.43
V, $\alpha = 35$	1.62	2.43
V, $\alpha = 25$	1.75	2.40

### Stress triaxiality

Figure 3.1.11 shows the stress triaxiality for the smooth specimen and specimen R2.0, R0.8 and R0.4 for quasi-static and dynamic analyses. Figure 3.1.12 shows similar graphs for the specimens with sharp notches. The highest triaxiality from each graph is given in Table 3.1.2. For the specimen with  $\alpha = 25^\circ$ , the high triaxiality value of 2.72 at the beginning of the dynamic simulation was ignored, since the value did not follow the tendency of the graph. This was obviously due to noise in the simulation. The triaxiality of the specimens increases as the notch radius decreases, but it is almost the same for the quasi-static and dynamic analyses for the smooth specimen and specimen R2.0, R0.8 and R0.4. For the quasi-static analyses of the sharp notches, the triaxiality increases some when  $\alpha$  decreases. It also seems like the strain rate has a much greater impact on the triaxiality for these specimens.

Henceforth, the geometry of the specimens will be used to study the effects of triaxiality. The smooth specimens will represent a low triaxiality. R2 and R0.8 will represent higher values. The V-notched specimen will represent the highest triaxiality obtained in the experiments.

### 3.1. Abaqus Simulations

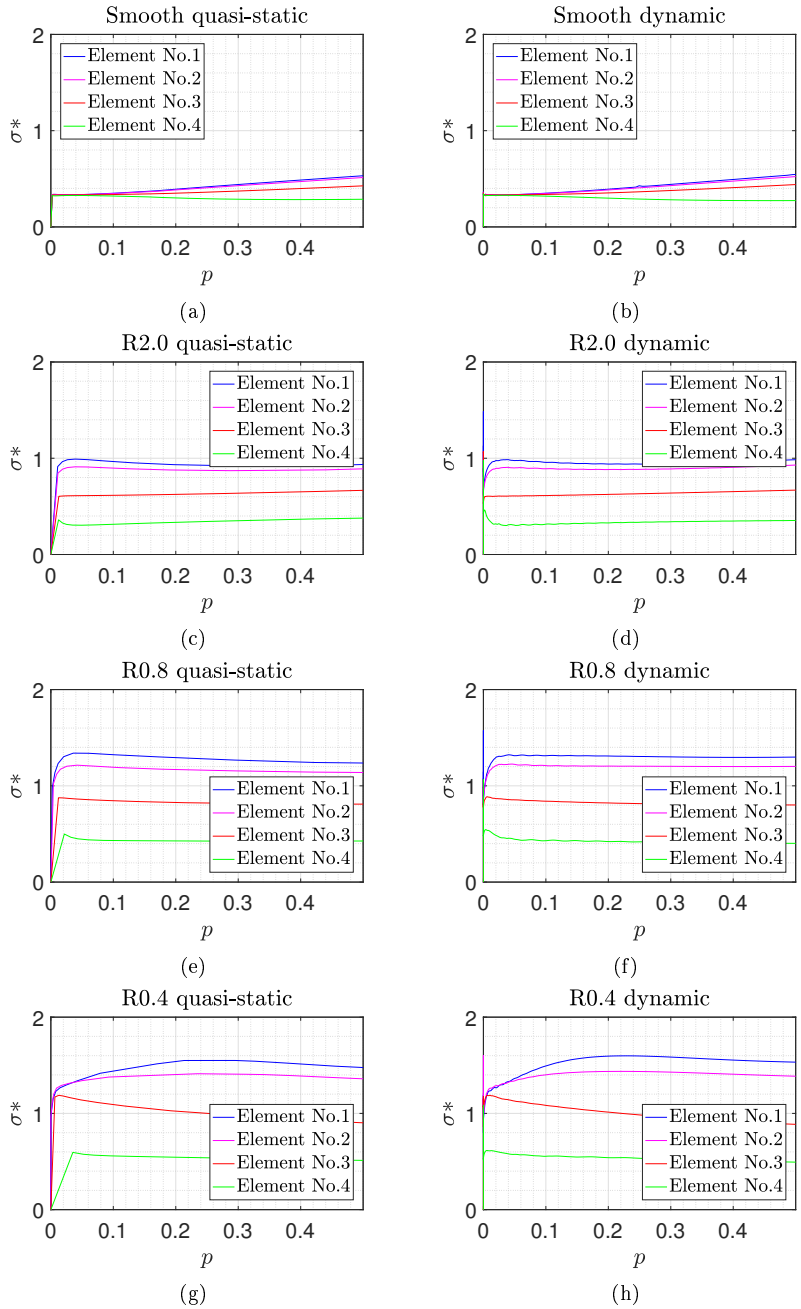


Figure 3.1.11: Stress triaxiality versus equivalent plastic strain for the different specimens at quasi-static and dynamic analyses.

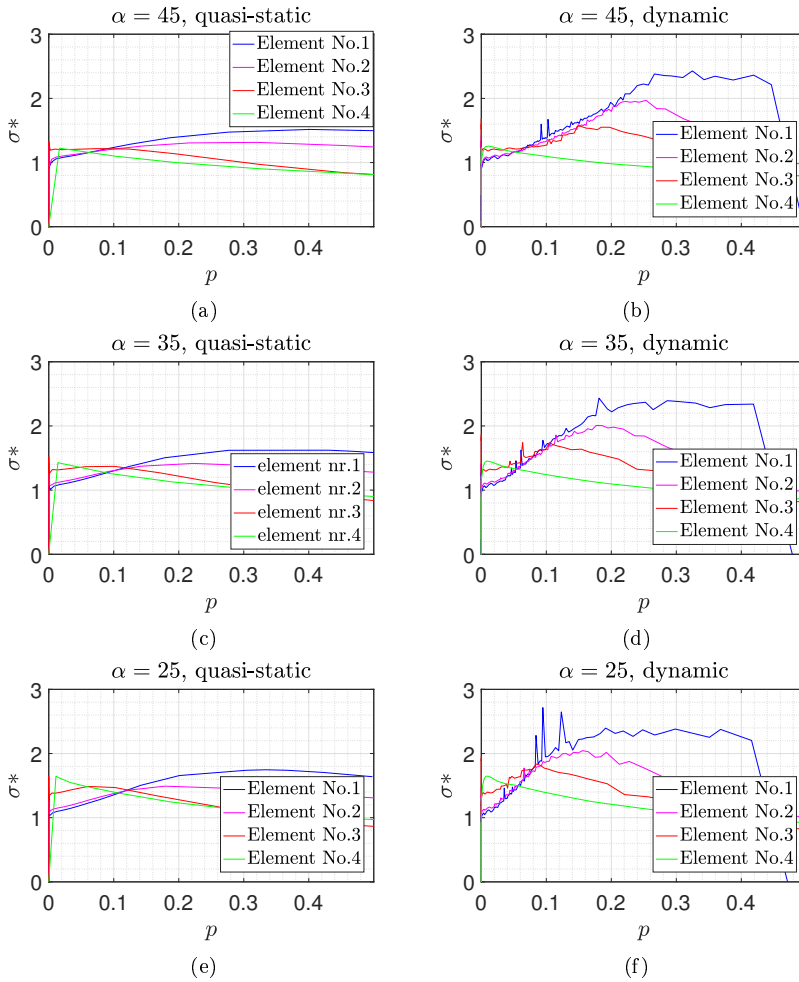


Figure 3.1.12: Stress triaxiality versus equivalent plastic strain for the V-notched specimens with an angle  $\alpha$  of  $45^\circ$ ,  $35^\circ$  and  $25^\circ$  at quasi-static and dynamic analyses.

## 3.2 Analytical MATLAB Model

In this study, an analytical MATLAB model implemented with the Cockcroft-Latham failure criterion for ductile fractures and Richie Knott Rice fracture criterion for brittle fractures was made. The model takes in the material parameters as input, and gives the strain at ductile and brittle failure as a function of temperature, strain rate and stress triaxiality. The model can also show the stress state in the material for different combinations of the factors mentioned above.

### 3.2.1 Establishing the Model

Both the ductile and brittle fracture criterion contains the highest principal stress  $\sigma_1$ . This stress can be calculated from  $\sigma_{eq}$ , which in this model is found using Johnson-Cook material model (Johnson and Cook, 1983).

$$\sigma_{eq} = (A + Bp^n)(1 + C \ln \dot{p}^*)(1 - (T^*)^m) \quad (3.2.1)$$

The reader is referred to Chapter 2 for a more thorough description of the formulas and theory used in this section. The constants used in the MATLAB model is given in Table 3.2.1. Since the MATLAB model is for temperatures from 0 K and higher,  $A$  is set to be the yield stress at 0 K. This is found as shown in equation (3.2.2) where  $T_r = 293$  K is the room temperature.

$$A = \frac{\sigma_0}{1 - \left(\frac{T_r - T_0}{T_m - T_0}\right)^m} \quad (3.2.2)$$

Table 3.2.1: Constants for the material model

Johnson-Cook hardening					
$\sigma_0$ [MPa]	$B$ [MPa]	$n$	$C$	$\dot{p}_0$ [1/s]	
456.6	410.8	0.4793	0.0104	0.000806	
Constants for fracture criteria					
$W_c$ [Nmm/mm <sup>3</sup> ]	$L$	$\sigma_{cr}$			
1562	-1	4A			
Adiabatic heating and temperature softening					
$c_e$ [mm <sup>2</sup> /s <sup>2</sup> K]	$\beta_{TQ}$	$T_m$ [K]	$T_0$ [K]	$\rho$ [kg/m <sup>3</sup> ]	$m$
$452 \cdot 10^6$	0.9	1 800	0	7 800	1

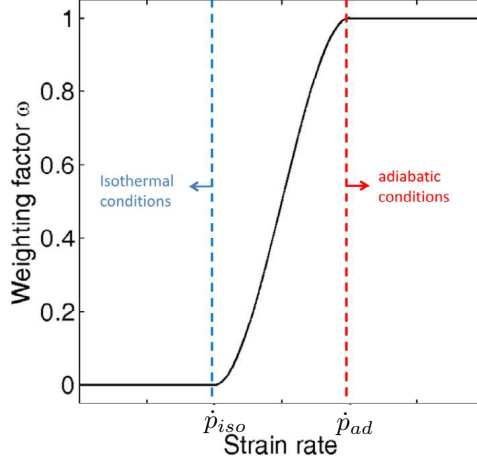


Figure 3.2.1: Illustration of the weighting function  $\omega$  (Roth and Mohr, 2014).

To implement the Johnson-Cook material model in MATLAB, user-defined vectors for temperature, strain, strain rate and stress triaxiality are made. Loops are used to find  $\sigma_{eq}$  for a given combination of the variables. The equivalent stress at a given index in the strain vector  $p_i$  is  $\sigma_{eq,i}$  and the equivalent stress for the next step is  $\sigma_{eq,i+1}$ .  $T_i$  is  $T$  at a given index in the strain vector. The adiabatic heating is included by the function below (Hopperstad and Børvik, 2017)

$$T_{i+1} = T_i + \frac{1}{2} \frac{\omega \beta_{TQ}}{\rho c_\varepsilon} (\sigma_{eq,i+1} + \sigma_{eq,i})(p_{i+1} - p_i) \quad (3.2.3)$$

where

$$\sigma_{eq,i+1} = (A + B p_{i+1}^n) \left( 1 + C \ln \left( \frac{\dot{p}}{\dot{p}_0} \right) \right) \left( 1 - \left( \frac{T_i - T_0}{T_m - T_0} \right)^m \right) \quad (3.2.4)$$

This is the same equations as in section 2.1.5, but instead of  $\beta_{TQ}$  changing from 0 to 0.9 at a given strain rate,  $\beta_{TQ}$  is set to 0.9 and is multiplied by the weighting function  $\omega$  (Roth and Mohr, 2014).  $\omega$  varies from 0 to 1 and is given by equation (3.2.5).

$$\omega(p) = \begin{cases} 0 & , \dot{p} < \dot{p}_{iso} \\ \frac{(\dot{p} - \dot{p}_{iso})^2 (3\dot{p}_{ad} - 2\dot{p} - \dot{p}_{iso})}{(\dot{p}_{ad} - \dot{p}_{iso})^3} & , \dot{p}_{iso} \leq \dot{p} \leq \dot{p}_{ad} \\ 1 & , \dot{p}_{ad} < \dot{p} \end{cases} \quad (3.2.5)$$

Figure 3.2.1 illustrates  $\omega$ . For strain rates below  $\dot{p}_{iso}$ ,  $\omega$  is zero, and the material deforms under isothermal conditions. For higher strain rates,  $\omega$  has a smooth transition until it reaches 1 at  $\dot{p} > \dot{p}_{ad}$  and the material deforms under adiabatic conditions. In the MATLAB model  $\dot{p}_{iso}$  was set to 10 [1/s] and  $\dot{p}_{ad}$  was set to 100 [1/s]. These values commonly used for steel (Mescall and Weiss, 1983).



### 3.2. Analytical MATLAB Model

---

The ductile criterion implemented in the model is the Cockcroft-Latham failure criterion (Cockcroft and Latham, 1968). By applying the trapezoidal rule for numerical integration, the damage is given by

$$D_{i+1} = D_i + \frac{1}{2W_c} \max\left(\sigma^* + \frac{3-L}{3\sqrt{3+L^2}}, 0\right)(\sigma_{eq,i+1} + \sigma_{eq,i})(p_{i+1} - p_i) \quad (3.2.6)$$

where  $\sigma^*$  is the triaxiality, and the Lode parameter  $L$  is set to -1.  $W_c$  is found from the results of tension tests for smooth specimens by Kristoffersen (2014). The model is set to find the strain when the damage becomes greater than unity for all combinations of triaxialities, strain rates and temperatures.

Ritchie-Knott-Rice fracture criterion is used as a brittle criterion. Fracture happens when  $\sigma_1$  reaches the critical value

$$\sigma_{cr} = R_{max}A \quad (3.2.7)$$

The maximum stress intensification factor  $R_{max}$  is an empirical value and is not known prior to the experimental work. In the basic model  $R_{max}$  is set to 4, but other values will be tested in a parameter study.  $\sigma_1$  is given by Equation (3.2.8).

$$\sigma_1 = \left(\sigma^* + \frac{3-L}{3\sqrt{3+L^2}}\right)\sigma_{eq} \quad (3.2.8)$$

The model is set to find the strain when  $\sigma_1$  reaches  $\sigma_{cr}$  for all combinations of triaxialities, strain rates and temperatures.

A copy of the MATLAB script is given in Appendix A.1.

#### 3.2.2 Transition Temperature

In this section, the behaviour of the transition temperature was studied by varying different parameters. A basic model was used where  $\dot{p} = 10^{-3}s^{-1}$ ,  $\sigma^* = 2.00$  and  $R_{max} = 4$ .

##### Consequence of strain rate

Figure 3.2.2 and Figure 3.2.3 shows the strain at failure for varying stress triaxialities and temperatures for strain rates of  $10^{-3}s^{-1}$  and  $10^3s^{-1}$ . Ductile and brittle failure are plotted together, and the fracture which requires the least strain will occur. The transition between ductile and brittle fracture happens in the line where the fracture planes intersect. For a strain rate of  $10^{-3}s^{-1}$  the transition happens at triaxialities between approximately 1.7 and 2.3. For a strain rate of  $10^3s^{-1}$  it happens at values between approximately 1.6 and 2.2. Both transition lines occur at a strain of approximately 0.8 and have the lowest triaxiality values for low temperatures and the highest for high temperatures. These results seems plausible since the tendency to brittle failure is expected to grow with the higher triaxialities, lower temperatures and higher strain rates.

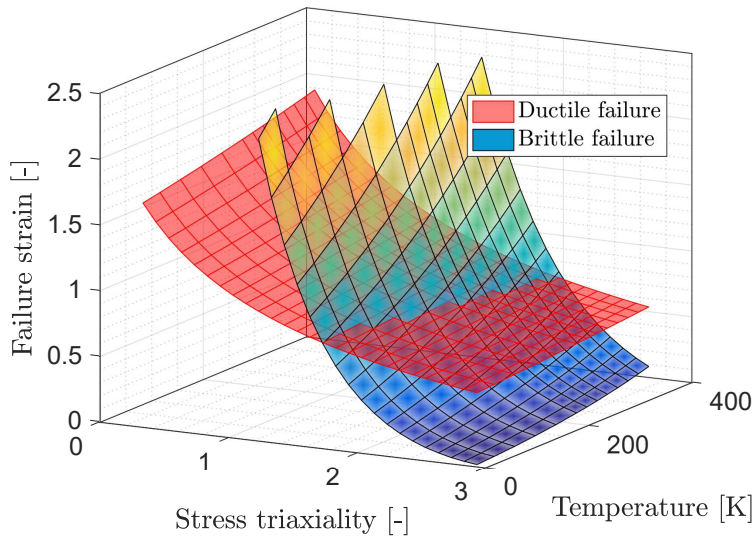


Figure 3.2.2: Stress triaxiality versus temperature and strain at failure for a strain rate of  $10^{-3}s^{-1}$ .

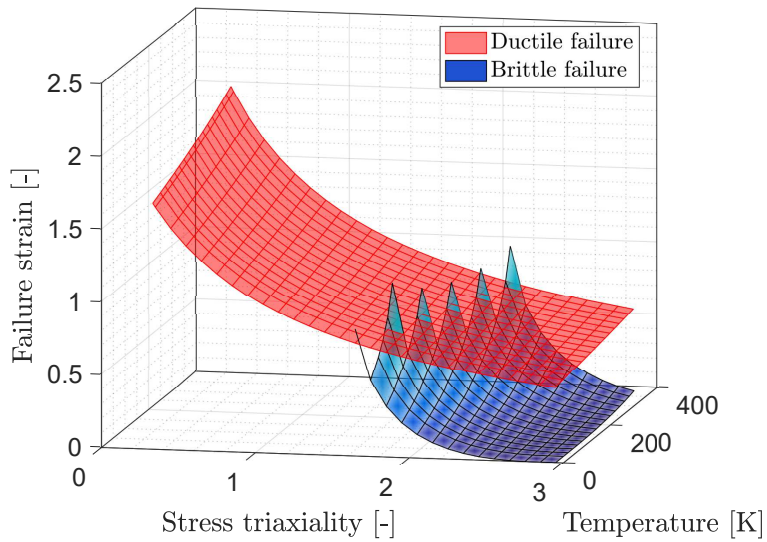


Figure 3.2.3: Stress triaxiality versus temperature and strain at failure for a strain rate of  $10^3s^{-1}$ .

### 3.2. Analytical MATLAB Model

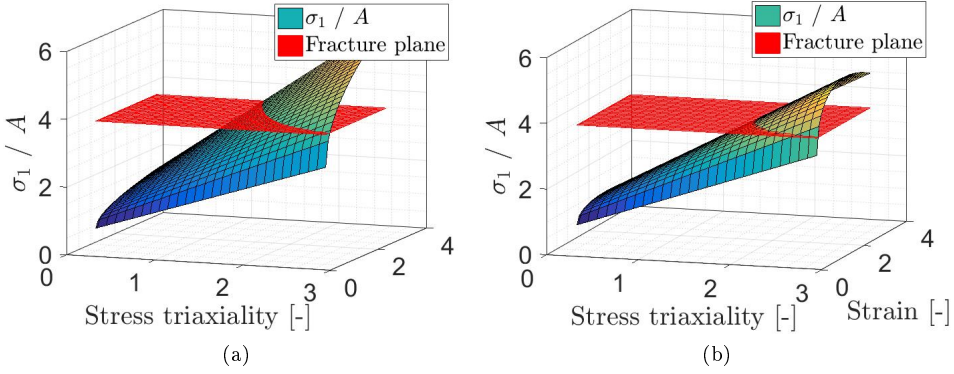


Figure 3.2.4:  $\sigma_1/A$  versus stress triaxiality and strain for a temperature of 293 K. a) Strain rate =  $10^{-3}s^{-1}$  b) Strain rate =  $10^3s^{-1}$

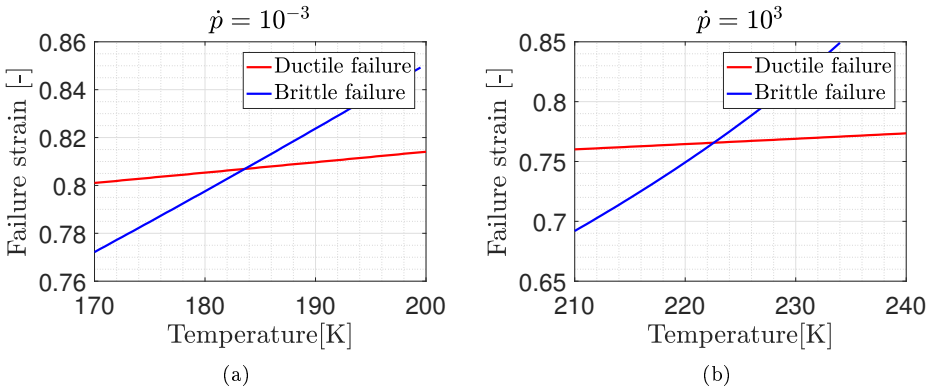


Figure 3.2.5: Temperature versus strain at failure for a strain rate of a)  $10^{-3}s^{-1}$  b)  $10^3s^{-1}$ .

Looking at Figure 3.2.3 for  $\dot{p} = 10^3s^{-1}$  it may seem like the brittle fracture plane behaves in the same way as in Figure 3.2.2 and that the failure strain has so high values that they are not shown in the graph. This is not the case. Figure 3.2.4 shows  $\sigma_1/A$  and the brittle fracture plane that is set to  $\sigma_1/A = 4$  for varying stress triaxialities and strains. The strain where the planes cross is the brittle fracture strain at a given triaxiality. In Figure 3.2.4a for  $\dot{p} = 10^{-3}s^{-1}$  the fracture strain increase with decreasing triaxialities and fracture happens at all strains. In Figure 3.2.4b for  $\dot{p} = 10^3s^{-1}$  the strain also increases with decreasing triaxialities until it reaches a maximum strain of 1.28 at a triaxiality of 2.06. For triaxialities lower than this, fracture does not happen.

Figure 3.2.5 shows the transition temperature for strain rates of  $10^{-3}s^{-1}$  and  $10^3s^{-1}$ . The transition temperature is the temperature where the fracture lines

cross. At  $\dot{p} = 10^{-3}s^{-1}$  the transition temperature is 184 K, while for  $\dot{p} = 10^3s^{-1}$  it is 223 K. This is an increase of 39 K. This transition is based on a stress triaxiality of 2.00. According to the results from the Abaqus simulations, this triaxiality will only be obtained with a sharp notched specimen at a dynamic simulation. This means that a sharp notched specimen at a dynamic simulation is expected to have a transition temperature higher than 223 K.

### Consequence of stress triaxiality

As mentioned earlier fracture happens at triaxialities between approximately 1.7 and 2.3 for low strain rates. In Figure 3.2.6 the transition temperatures for triaxialities from 1.75 to 2.25 at a strain rate of  $\dot{p} = 10^{-3}s^{-1}$  is found. The results are presented in the Table 3.2.2. Low triaxialities gives low transition temperatures,

Table 3.2.2: Transition temperature

$\sigma^*$	1.75	2.00	2.05	2.10	2.15	2.20	2.25
Kelvin	16	184	213	242	270	296	322
Degrees Celsius	-257	-89	-60	-31	-3	23	49

and the first relevant result is at a triaxiality of 2.00, where the transition temperature is 184 K. When triaxialities increases with 0.05, the transition temperature rise with about 27 K. For low triaxialities it rises more, and for high triaxialities it rises less. The transition happens at room temperature for a triaxiality of 2.20.

### Consequence of the stress intensification factor

Figure 3.2.7 shows the transition temperature when varying the maximum stress intensification  $R_{max}$  with a strain rate of  $10^{-3}s^{-1}$  and a triaxiality of 2.00.  $R_{max} = 3$  is a conservative assumption which requires low equivalent stress for brittle fracture. At this factor, the fracture is brittle for all temperatures, and the fracture strain is less than 0.25. The curves for ductile failure strain is the same for all values of  $R_{max}$ . For  $R_{max} = 4$  the brittle failure strain has increased, and the transition temperature is 184 K at a strain of 0.8. When  $R_{max} = 5$ , the equivalent stress needed for brittle fracture is so high that ductile fracture happens before brittle for all temperatures.

Figure 3.2.8 shows the strain at failure for varying stress triaxialities and temperatures for a strain rate of  $10^{-3}s^{-1}$  and  $R_{max}$  of 3 and 5. Although the material does not have a transition temperature when the triaxiality is 2.00 and  $R_{max}$  is 3 or 5, the transition happens at other triaxialities. For  $R_{max} = 3$  the transition happens for triaxialities in the range [1.0 - 1.4] at a fracture strain of 1.1. This means that the transition will happen for the notched specimens. At  $R_{max} = 5$  the transition happens at  $\sigma^* = 2.46$  and higher triaxialities. This indicates that it is hard to obtain cleavage for quasi-static simulations if  $R_{max} = 5$ .

### 3.2. Analytical MATLAB Model

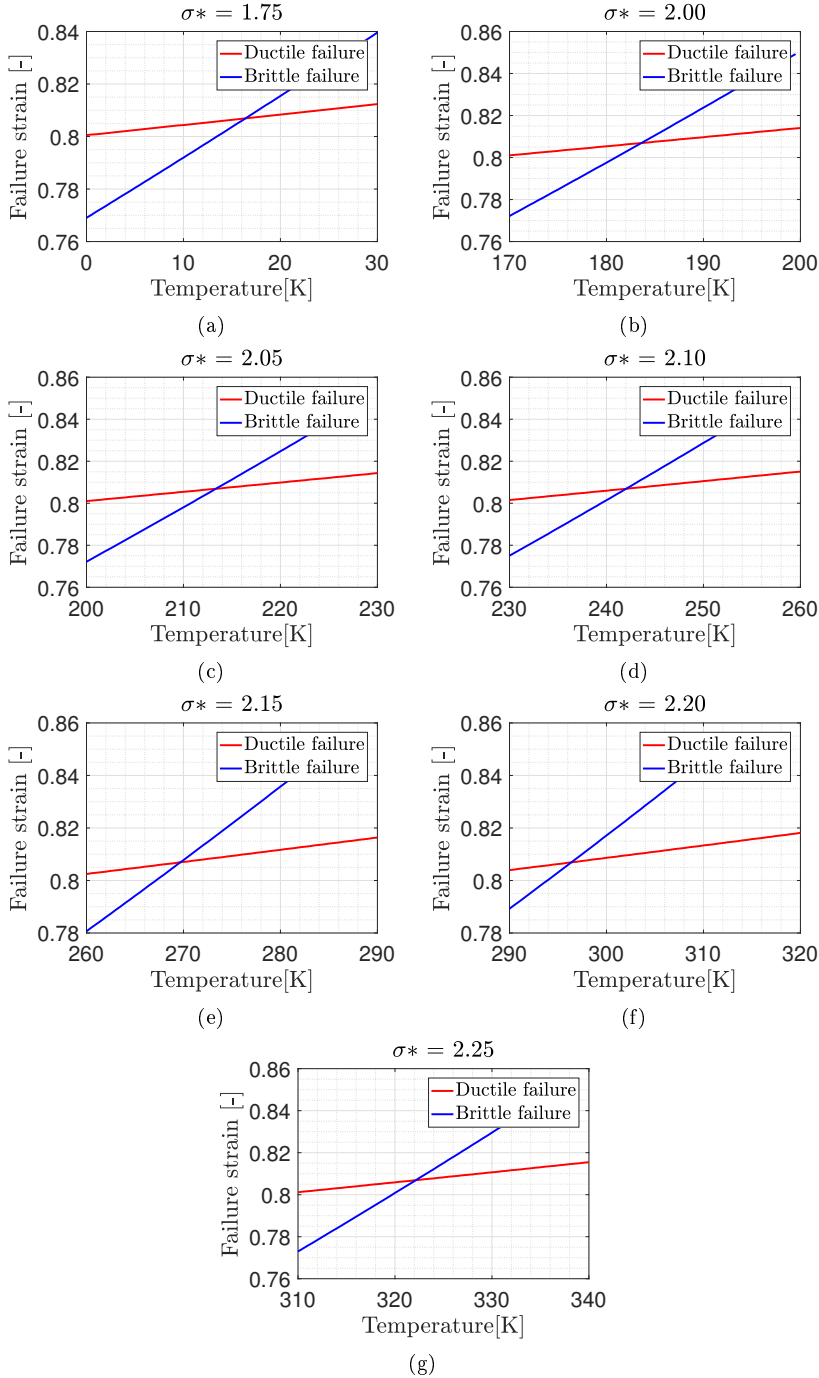


Figure 3.2.6: Temperature versus failure strain for triaxialities from 1.75 to 2.25.

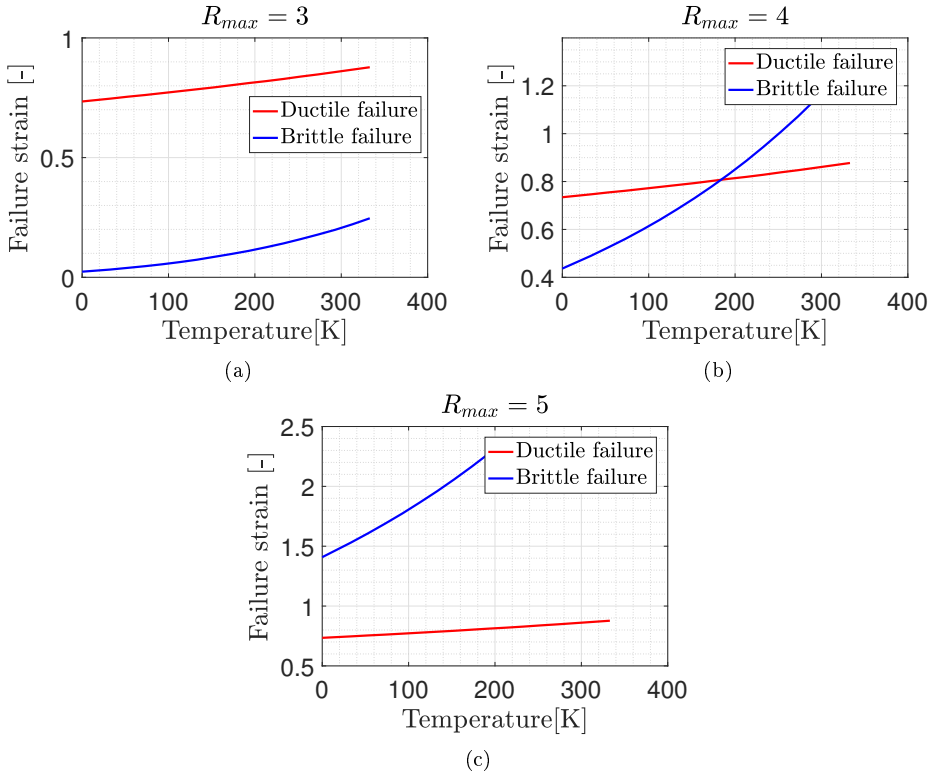


Figure 3.2.7: Temperature versus strain at failure for a strain rate of  $10^{-3} s^{-1}$ , a triaxiality of 2.00 and a  $R_{max}$  of a) 3 b) 4 c) 5.

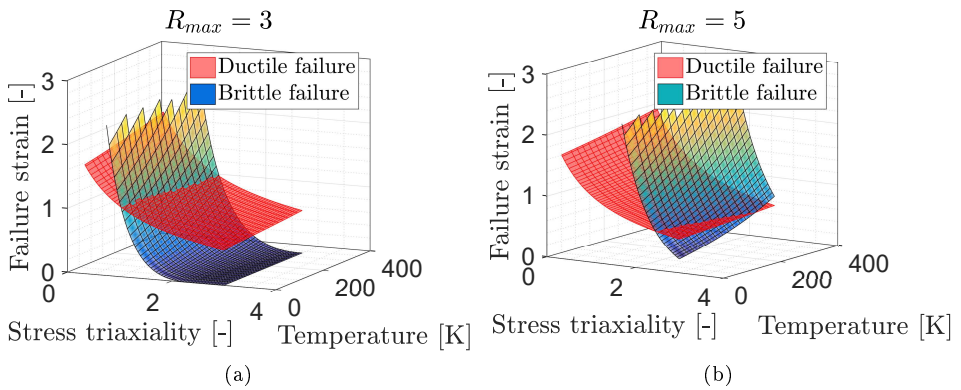


Figure 3.2.8: Stress triaxiality versus temperature and strain at failure for a strain rate of  $10^3 s^{-1}$  and a  $R_{max}$  of a) 3 b) 5.



# EXPERIMENTAL WORK

---

Tension tests were performed to study the material behaviour of a X65 steel and in particular the effects of triaxiality, strain rate and temperature. The exact chemical composition of the steel was not available. The specimens used in the tests were taken from a steel pipe that was formed from plates rolled into pipes and welded longitudinally. They were taken at 6 o'clock in the cross-section, which represents the side opposite to the weld, see Figure 4.0.1. This is the side that was exposed to the largest deformations under the rolling, and this may have led to anisotropic properties. The longitudinal direction of the specimens corresponds to the longitudinal direction of the pipe, and the thickness direction of the pipe was marked at the end of the test specimens.

The specimens are illustrated in Figure 4.0.2. The left side shows the geometry of the longitudinal direction of the specimens, while the cross-sections are shown to the right. These figures show that the outer diameter was 5 mm, while the diameter at the gauge area was 3 mm. The red line represents the thickness direction. The smooth specimens had a gauge length of 5 mm, the notched had notches of 2.0 mm and 0.8 mm radius and the specimens with sharp notches had notches with an angle of  $45^\circ$ . Henceforth these specimens will be called smooth, R2, R0.8 and V. For manufacturing reasons the side faces of the R0.8 notches were inclined with an angle  $\alpha = 17.5^\circ$ . After manufacturing, a more accurate diameter of each specimen was found using lasers and each specimen was given names. The

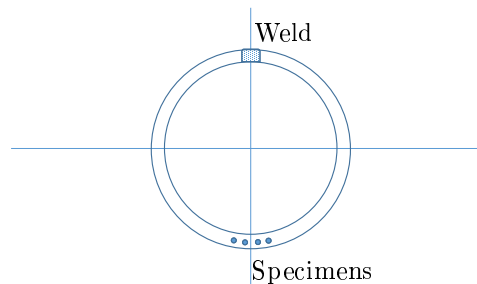


Figure 4.0.1: Cross-section of offshore pipe. Specimens taken from the side opposite to the weld.



smooth specimens were given the names Smooth No.1, Smooth No.2 and so on. The notched got names like R2 No.1, R0.8 No.1 or V No.1.

The smooth specimens were used to calibrate the material model, while the notched specimens would show the effect of triaxiality. To study the effect of strain rate, both quasi-static and dynamic tests were performed. A temperature chamber was used to perform tests at lower temperatures. An optical microscope was used to find the gauge diameter after fracture, and a scanning electron microscope (SEM) was used to study the fracture surface.

## 4.1 Quasi-Static Tension Tests

### 4.1.1 Setup

The quasistatic tension tests in room temperature were performed with a 100 kN Instron test machine (see Figure 4.1.1a) while the tests at low temperatures were performed with a 250 kN Instron test machine (see Figure 4.1.2a). These machines are screw-driven, and the load adjusts itself to the displacement to get a constant velocity.

In the tests at room temperature, the velocity was set to 0.15 mm/min for the smooth specimens. The notched specimens had a shorter gauge area than the smooth. This led to a higher strain rate. To get similar strain rate in the smooth and notched specimens, the velocity was decreased to 0.10 mm/min for the notched specimens. The test machine registered the force and displacement applied by the machine. Lasers were used to find the diameter reduction, see Figure 4.1.1b. The laser creates two perpendicular beams. By placing the thickness direction parallel to one of the laser beams, the anisotropy due to the rolling could be detected. The height of the laser beams was adjusted during the tests to make sure that the minimal diameter always was detected.

For tests at lower temperatures the temperature chamber in Figure 4.1.2 was used. Liquid nitrogen was used to lower the temperature, and thermometers measured the temperature and controlled the amount of liquid nitrogen added. Due to the temperature chamber, lasers could not be used to measure the diameter during these tests. Instead a camera was used, and a mirror with an angle was used to see the reflection of the thickness direction and the transverse direction.

Edge-tracing could have been used on the pictures to get the diameter during the tests and to find the true strain and stress. This was not within the scope of this thesis, but will be done in further studies of the material. In this thesis the force and displacement data from the machine were used to find the engineering stress and a normalized elongation.

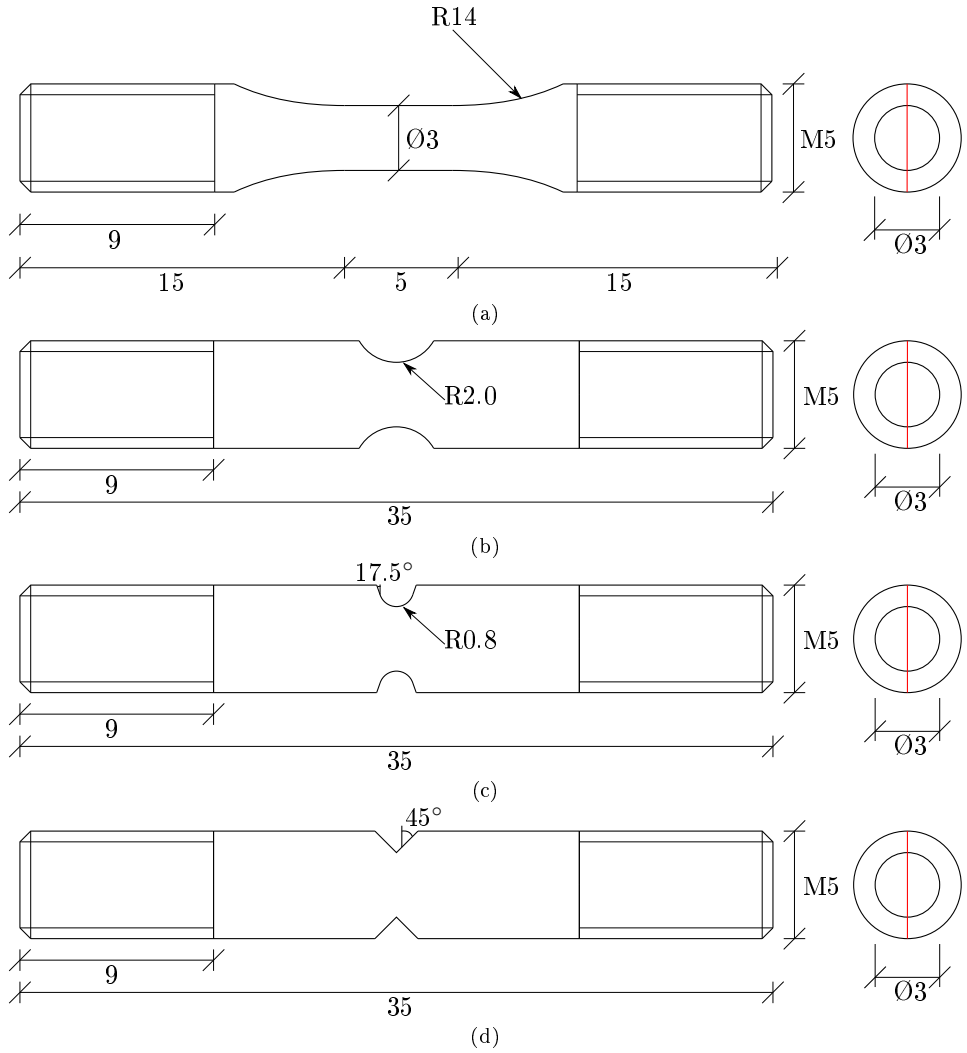


Figure 4.0.2: Geometry of the tensile specimens. (a) Smooth, (b) R2, (c) R0.8, (d) V. The red lines represents the thickness direction.

#### 4.1. Quasi-Static Tension Tests

---

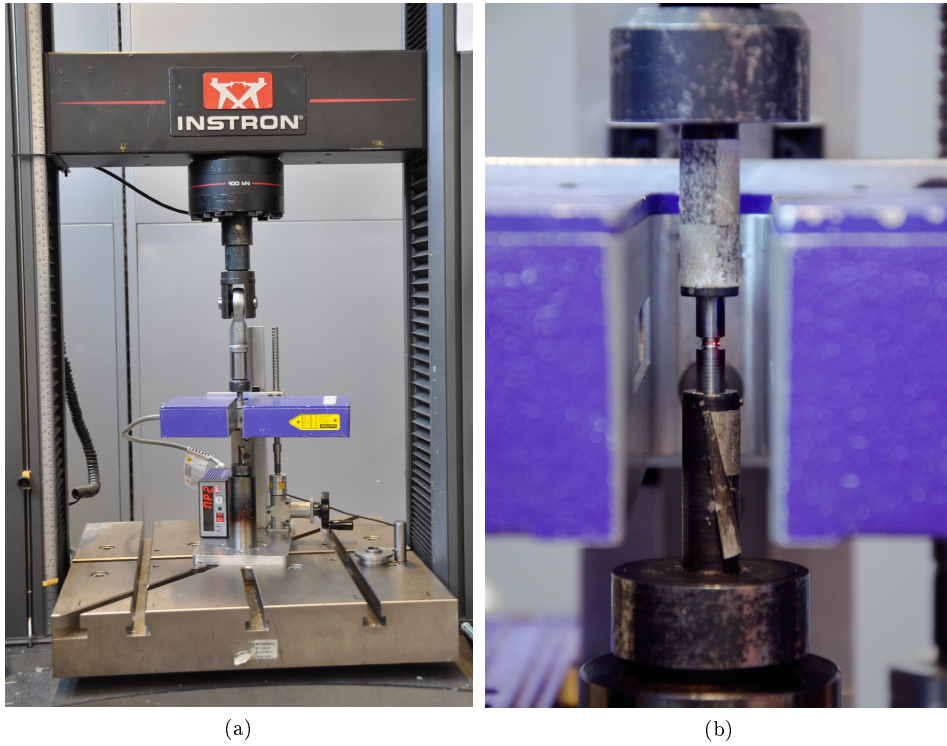


Figure 4.1.1: 100 kN Instron test machine.

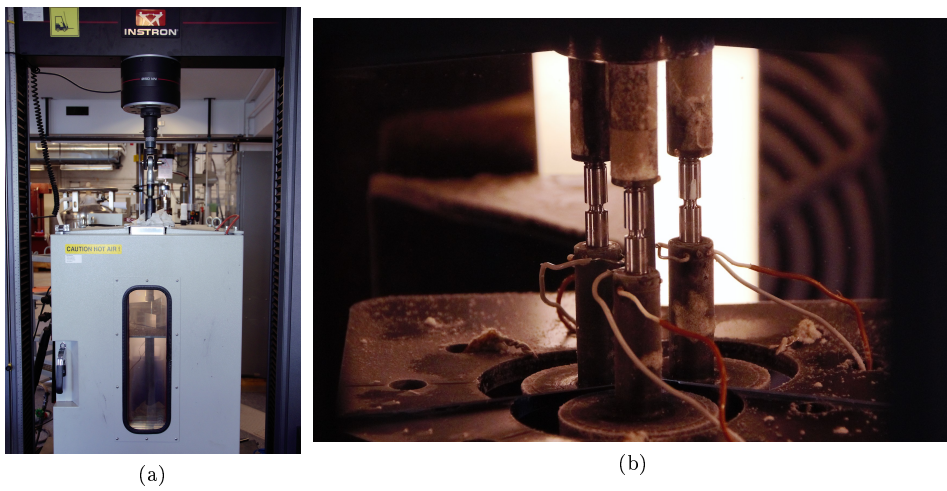


Figure 4.1.2: 250 kN Instron test machine.

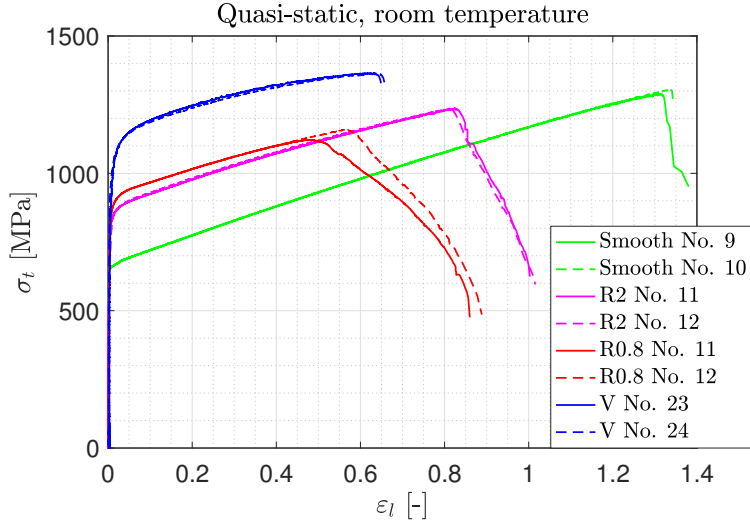


Figure 4.1.3: True stress versus logarithmic strain for the specimens deformed quasi-statically at room temperature.

## 4.1.2 Results

### Room temperature

The quasi-static tests were conducted by Tore Andre Kristensen, Engineer at SINTEF. The data from the tests were given in spreadsheets containing time, force, position, diameter  $D_x$  and diameter  $D_y$ .  $D_x$  is the diameter in the thickness direction, while  $D_y$  represents the transverse direction.

During the tests the height of the lasers was adjusted continuously to get the value of the smallest diameter. This led to a great variation in the diameter and the data needed to be edited to get the right results. The corrected diameter at a given time was set to be the smallest of the diameter measured and the previous corrected diameter. This led to a smooth, decreasing curve.

The cross-section at the neck was assumed to have the shape of an ellipse. The area at a given time was found by the equation:

$$A = \frac{\pi D_x D_y}{4} \quad (4.1.1)$$

The true stress and logarithmic strain were found by the equations:

$$\sigma_t = \frac{F}{A} \quad \varepsilon_l = \ln\left(\frac{A_0}{A}\right) \quad (4.1.2)$$

This gave the results shown in Figure 4.1.3. The curves were cut at fracture where the stress drops straight to zero. It is evident that the stress level increases as the notches get smaller and the triaxiality gets higher. The fracture strain on the

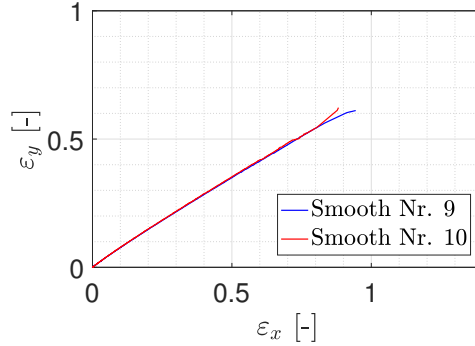


Figure 4.1.4: True strain in x- versus y-direction for the smooth specimens deformed quasi-statically at room temperature.

other hand, decreases for smaller notches. The R0.8 specimens show a behaviour where the stress level is not much higher than for the R2 specimen, but the failure strain is much lower. The V-notched specimen has a stress level approximately 200 MPa higher than R0.8, but the failure strain is actually higher. The fracture strain of R0.8 is much higher than the failure strain. The strain after failure may be an example of void growth and coalescence, see Figure 2.2.1d, 2.2.1e and 2.2.1f. When the voids starts to grow together, the true stress decreases. The growth and coalescence continues until fracture.

To study if the material has a isotropic behaviour, strains in the thickness direction  $\varepsilon_x$  and transverse direction  $\varepsilon_y$  can be compared, see the equations below.

$$\varepsilon_x = -\ln \frac{D_x}{D_0} \quad \varepsilon_y = -\ln \frac{D_y}{D_0} \quad r = \frac{\varepsilon_y}{\varepsilon_x} \quad (4.1.3)$$

Figure 4.1.4 shows the relation between  $\varepsilon_x$  and  $\varepsilon_y$ . From the figure it is clear that the material deforms much more in the thickness direction. The  $r$ -value, which tells the ratio between the strains in the two directions, has a value between 0.7 and 0.8 for most of the experiment.

Figure 4.1.5 and Table 4.1.1 show the failure strain and the fracture strain for the quasi-static tests at room temperature. The failure strain is the true strain at the highest true stress. The fracture strain was found by measuring the diameters  $D_x$  and  $D_y$  after fracture using an optical microscope, and using the equations for areal and true strain below:

$$A = \frac{\pi D_x D_y}{4} \quad \varepsilon_l = \ln\left(\frac{A_0}{A}\right) \quad (4.1.4)$$

$A_0$  was found from the diameter measured by a laser before the tests started.

A good way to measure the fracture diameter of the specimen is putting it back together and measure the diameter from the side. This is a way to ensure that the smallest diameter is measured. Figure 4.1.6 shows an example where the diameter

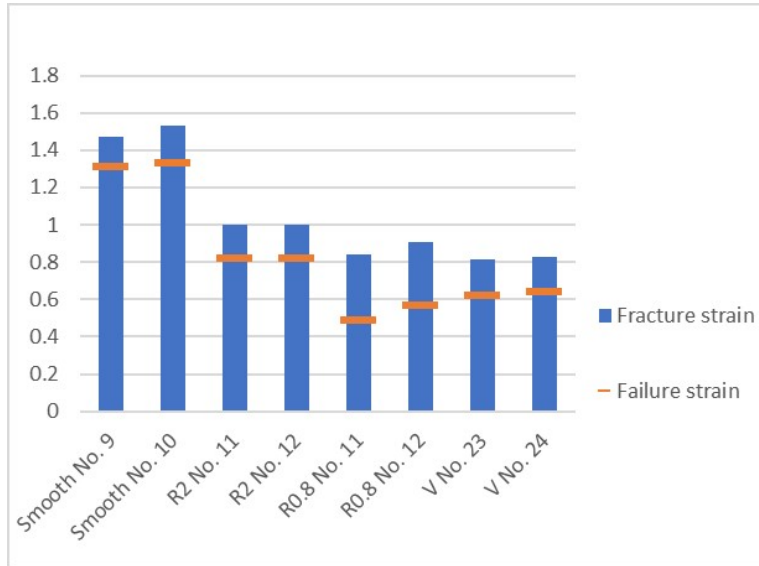


Figure 4.1.5: Failure strain and fracture strain for the quasi-static tests at room temperature.

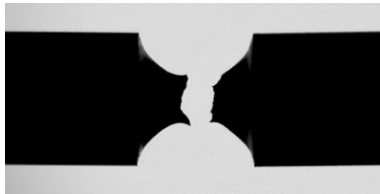


Figure 4.1.6: Example of a fracture where it is difficult to measure the fracture diameters using an optical microscope.

should be measured from the side. The disadvantage with this technique is that the fracture surfaces may damage each other. Since these surfaces were going to be studied with SEM later, this technique was not used. Instead the diameters were measured while considering the fractured ends. This technique measures the diameter at the fracture, and as seen in Figure 4.1.6 this is not necessarily the smallest diameter. Another disadvantage is that it sometimes was hard to see the boundary of the fracture surface. This led to that some of the diameters, especially for the notched specimens, were measured to big, leading to smaller fracture strains than in the reality.

From the results it looks like the fracture strain decreases when the triaxiality increases. The failure strain also decreases for higher triaxiality, but as seen in the true stress and logarithmic strain graph, the failure strain is lowest for the R0.8 specimen.

## 4.1. Quasi-Static Tension Tests

---

Table 4.1.1: Failure strain and fracture strain for the quasi-static tests at room temperature

Specimen	Failure strain [-]	Fracture strain [-]
Smooth No.9	1.31	1.47
Smooth No.10	1.33	1.53
R2 No.11	0.82	1.00
R2 No.12	0.82	1.00
R0.8 No.11	0.49	0.84
R0.8 No.12	0.57	0.91
V No.23	0.62	0.82
V No.24	0.64	0.83

### Low temperature

The quasi-static tests at low temperatures were also conducted by Tore Andre Kristensen. The plan was to test two of each type of specimen at 243 K and two of the V-notched specimens at 213 K and 183 K. In the first tests, much time was used to be certain that there was no icing on the gauge area and on the mirror. After the smooth specimens and some of the notched specimens were tested, it was decided to open the chamber and let the temperature get back to room temperature before placing a specimen in the machine between every test. This would prevent icing from appearing on the specimen when it was placed inside the chamber. This procedure would make the testing of each specimen take much longer time, and it was decided to just test one V-notched specimen at each temperature.

The data from the tests were given in spreadsheets containing time, force and displacement of the machine. The engineering stress and engineering strain are given by the equations below:

$$\sigma_e = \frac{F}{A_0} \quad \varepsilon_e = \frac{\Delta L}{L_0} \quad (4.1.5)$$

Since the displacement were taken from the machine,  $L_0$  was set to 17 mm, which is the length of the specimen when the clamped ends are neglected. The engineering stress and a normalized elongation given by  $\Delta L/L_0$  mm was found.

The results at 243 K are shown in Figure 4.1.7. The V-notched specimens at 183 K, 213 K and 243 K are compared in Figure 4.1.8. The curves are cut at fracture, where the stress drops to zero. Since normalized elongation is used, and not logarithmic strain or engineering strain, the deformations of different specimens are not comparable. The stress of R2 and R0.8 is higher than for the smooth specimens, and the V-notch has even higher stress. From the figure of the V-notched specimens, it seems like the only consequence of the decreasing temperature is that the stress level increases.

Table 4.1.2 gives the fracture strain obtained by using an optical microscope. This strain is therefore approximately the true fracture strain. Since this is the local strain in the neck, the value is much higher than the normalized elongation

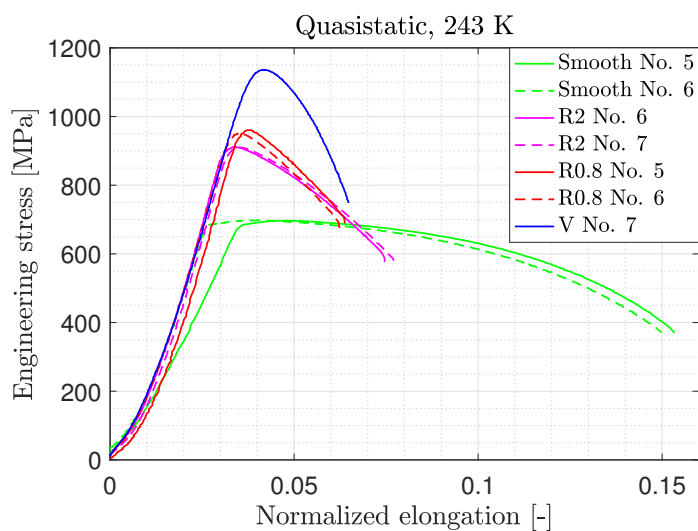


Figure 4.1.7: Engineering stress versus normalized elongation for the specimens deformed quasi-statically at 243 K.

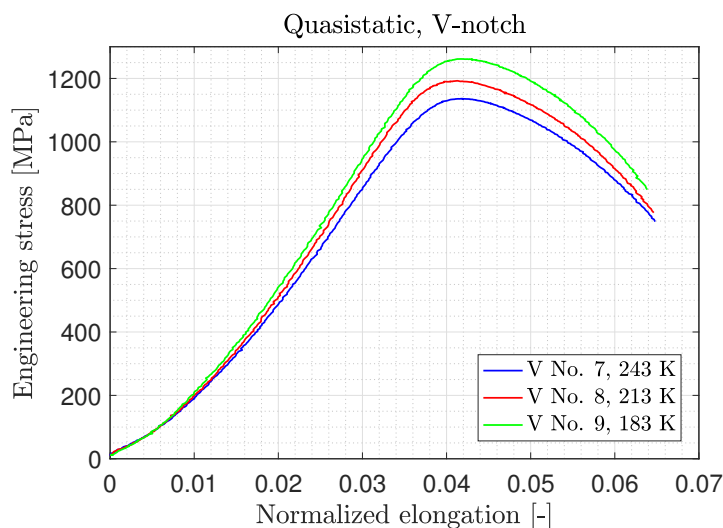


Figure 4.1.8: Engineering stress versus normalized elongation for the V-notched specimens deformed quasi-statically at 183 K, 213 K and 243 K



## 4.2. High Strain Rate Tension Tests

Table 4.1.2: Fracture strain for the quasi-static tests at 183 K, 213 K and 243 K.

Specimen	Temperature [K]	Fracture strain [-]
Smooth No.5	243	1.45
Smooth No.6	243	1.47
R2 No.6	243	0.99
R2 No.7	243	1.04
R0.8 No.5	243	0.84
R0.8 No.6	243	0.92
V No.7	243	0.67
V No.8	213	0.69
V No.9	183	0.61

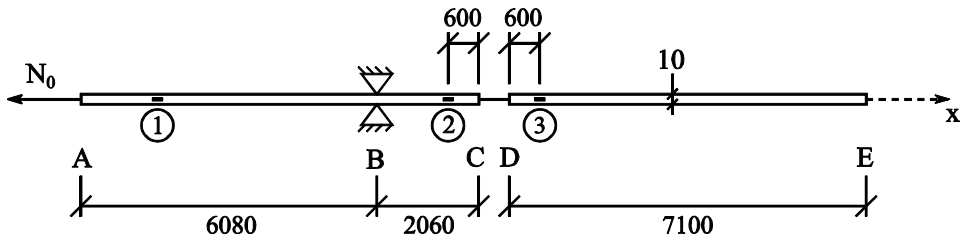


Figure 4.2.1: Outline of split-Hopkinson tension bar at NTNU, measures in mm (Langseth et al., 2016).

given in Figure 4.1.7 and Figure 4.1.8. The table indicates that specimen geometry has a great impact on the fracture strain, while the temperature does not influence it that much in quasi-static tests.

## 4.2 High Strain Rate Tension Tests

### 4.2.1 Setup

The dynamic tension tests were performed using a split-Hopkinson tension bar (SHTB). This is a machine used in tension tests at strain rates of order  $10^2$  to  $10^4$   $s^{-1}$ . The SHTB at NTNU is illustrated in Figure 4.2.1. The machine consists of two steel bars with a cross-sectional diameters of 10 mm. The input bar ABC has a length of 8140 mm and the output bar DE a length of 7100 mm. They are made of steel quality Tibnor 52SiCrNi5 and have a Young's modulus  $E$  of 204 GPa and a yield stress of approximately 900 MPa (Langseth et al., 2016).

At the start of a test, the specimen is attached to the bars between point C and D. The input bar is locked in point B and the output bar in the end E. Part AB of the input bar is stretched by applying a load using a hydraulic jack in point A. To ensure an elastic behaviour of the bar, the load must be less than 70 kN. When

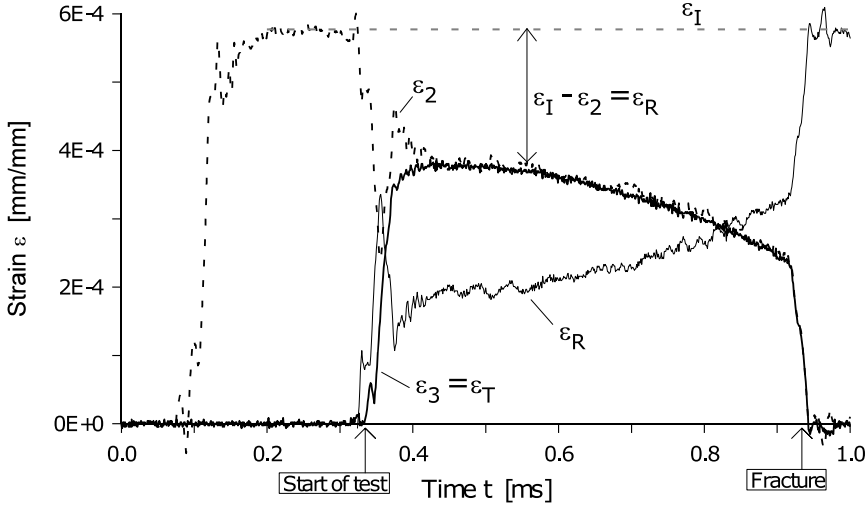


Figure 4.2.2: Example of data registered by strain gauge 2 and 3 (Langseth et al., 2016).

the load reaches the value  $N_0$ , the lock at B is broken manually. The strain energy stored in AB is released, and a stress wave propagates through bar AC towards the specimen. The impedance mismatch between the steel bar and the specimen leads to the stress wave partly being transmitted into the output bar and partly being reflected back (Langseth et al., 2016).

The split-Hopkinson tension bar has three pairs of strain gauges placed at point 1, 2 and 3 in Figure 4.2.1. The strain gauge in point 1 monitors the force  $N_0$ , while the two others measure the strain-time history. Figure 4.2.2 shows an example of data registered by strain gauge 2 and 3, where  $\varepsilon_2$  represents gauge 2 and  $\varepsilon_3$  gauge 3.  $\varepsilon_I$  is the incoming strain,  $\varepsilon_R$  the reflected strain and  $\varepsilon_T$  the transmitted strain. A detailed explanation of how to understand the strain-time history is given in the Lecture notes of Langseth et al. (2016).

The engineering stress and engineering strain in the specimens are given in the equations below.

$$\sigma_s = \frac{E_0 A_0}{A_s} \varepsilon_T \quad \varepsilon_s = -2 \frac{c}{L_s} \int_0^t \varepsilon_R d\tau \quad (4.2.1)$$

$E_0 A_0$  is the axial stiffness of the bar,  $A_s$  is the area of the specimens cross-section in the gauge area,  $L_s$  is the length of the specimen's gauge area,  $c$  is the wave propagation velocity and  $\varepsilon_R$  is integrated over the time  $\tau$ . In this thesis, specimens with notches were used. These did not have a gauge length. To be able to calculate a normalized elongation,  $L_s$  was set to 17 mm for all the specimens.  $L_s$  was the length of the specimen when the clamped ends were neglected.

Another way to get data from a SHTB test is to use a high-speed camera. Edge-tracing can be used on the pictures to get the diameter as the specimen

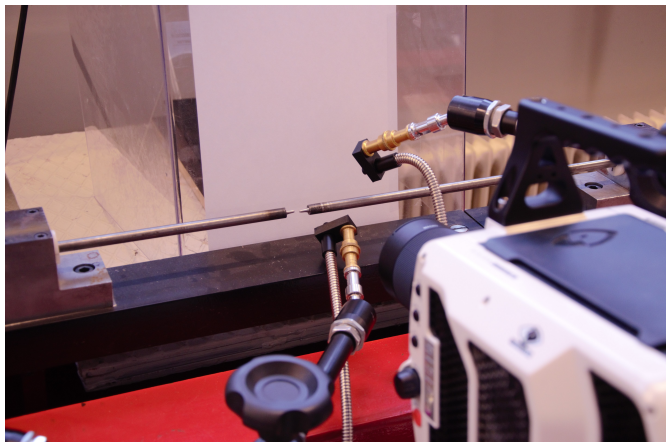


Figure 4.2.3: Split-Hopkinson tension bar with a high-speed camera and a fractured specimen.

deforms, and the diameter can be used to get the true stress and strain. Figure 4.2.3 shows the SHTB with a fractured specimen and a high-speed camera. The white background and the two lights are used to make a better contrast at the edges of the specimen.

In the tension tests with SHTB in this thesis, a high-speed camera was used, but edge-tracing was not within the scope, and the results were taken from the strain gauges. For lower temperatures, the temperature chamber in Figure 4.2.4 was used. Liquid nitrogen was used to lower the temperature. Thermometers measured the temperature in the chamber and at the input bar, and controlled the amount of liquid nitrogen added. During this tests, frost mist appeared in the chamber, frost appeared on the wall of the chamber and icing appeared on the specimens, see Figure 4.2.5. Various attempts were done to reduce this, but some of the specimens still got some icing.

### 4.2.2 Results

#### Room temperature

The high strain rate tension tests were conducted by Trond Auestad at NTNU. All tests at room temperature were successful. Figure 4.2.6 gives the engineering stress versus the normalized elongation described previously in section 4.2. It is clear that the stress level increases at higher triaxialities. The stress level of R0.8 is almost the same as R2. Due to the use of normalized elongation, the deformation of different specimens cannot be compared from this figure.

Table 4.2.1 gives the average elongation rate and the fracture strain for the specimens tested. The average elongation rate is for the whole length and found with the same assumptions as the normalized elongation. Due to these assumptions,

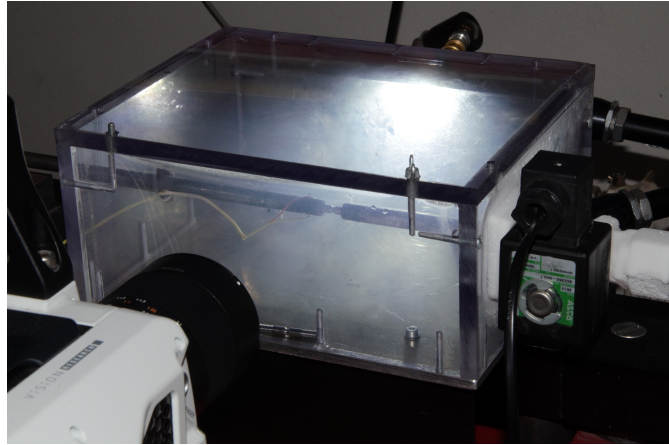


Figure 4.2.4: Split-Hopkinson tension bar with a temperature chamber.

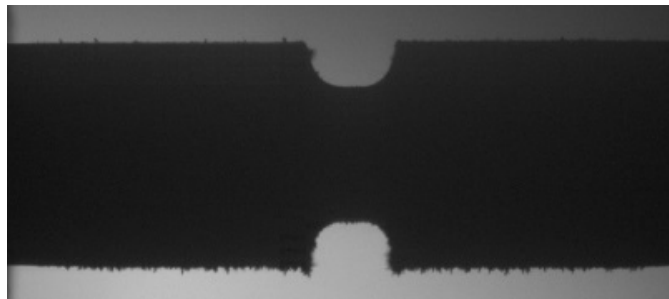


Figure 4.2.5: Specimen with icing.

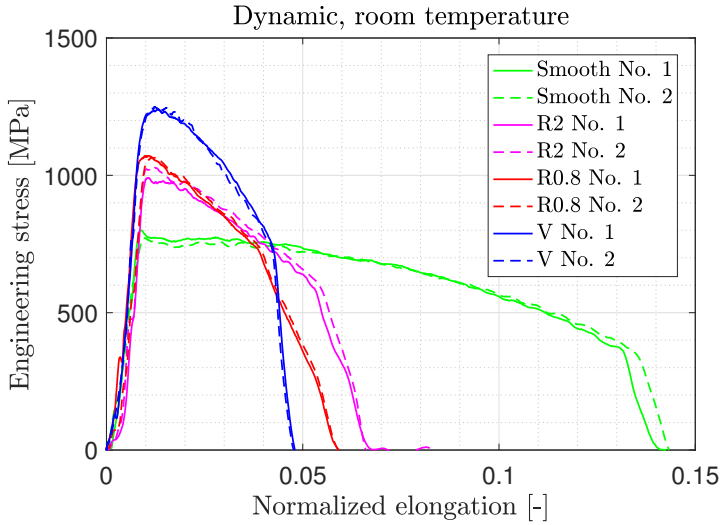


Figure 4.2.6: Engineering stress versus normalized elongation for the dynamic tests at room temperature.

the average elongation rate can be much higher locally in the specimens. The fracture strain was found using an optical microscope for the quasi-static test. Since the fracture strain is the local strain at the neck, the value is much higher than the elongation given in Figure 4.2.6. The table indicates that the fracture strain decreases for higher triaxialities.

Table 4.2.1: Average strain rate and fracture strain for the dynamic tests at room temperature.

Specimen	Average elongation rate [ $s^{-1}$ ]	Fracture strain [-]
Smooth No.1	222.7	1.31
Smooth No.2	215.3	1.17
R2 No.1	89.1	1.04
R2 No.2	148.1	0.94
R0.8 No.1	134.6	1.01
R0.8 No.2	140.2	0.87
V No.1	72.5	0.80
V No.2	55.5	0.85

Table 4.2.2: Average strain rate and fracture strain for the dynamic tests at 213 K and 243 K.

Specimen	Temperature [K]	Average elongation rate [ $s^{-1}$ ]	Fracture strain [-]
Smooth No.3	243	190.3	1.26
Smooth No.4	243	190.6	1.33
R2 No.3	243	129.5	0.95
R2 No.4	243	-	0.84
R2 No.5	243	123.1	0.78
R0.8 No.3	243	116.6	0.81
R0.8 No.4	243	100.2	0.43
V No.3	243	28.4	0.40
V No.4	243	58.4	0.12
V No.5	213	50.1	0.30
V No.6	213	52.7	0.20

### Low temperature

All tests except of R2 No.4 were successful. The part of the machine collecting the data was triggered at the wrong time during R2 No.4, and the results were not saved.

Figure 4.2.7 shows the engineering stress versus normalized elongation for dynamic tests at 213 K and 243 K. The results show the same tendency as earlier, where the stress increases with increasing triaxiality and decreasing temperature, but there is more variation in the results. Looking at V No.3 and V. No.4, the maximum strain is almost the same, but it looks like part of the cross section goes to fracture earlier for V No.4. This may be due to a less ductile behaviour where small defects can lead to fracture.

Table 4.2.2 gives the average elongation rate and the fracture strain for the spesimens tested. The specimens fracture at lower strains for high triaxialities and low temperatures, but the data is scattered, which is often the case for specimens exhibiting a less ductile behaviour.

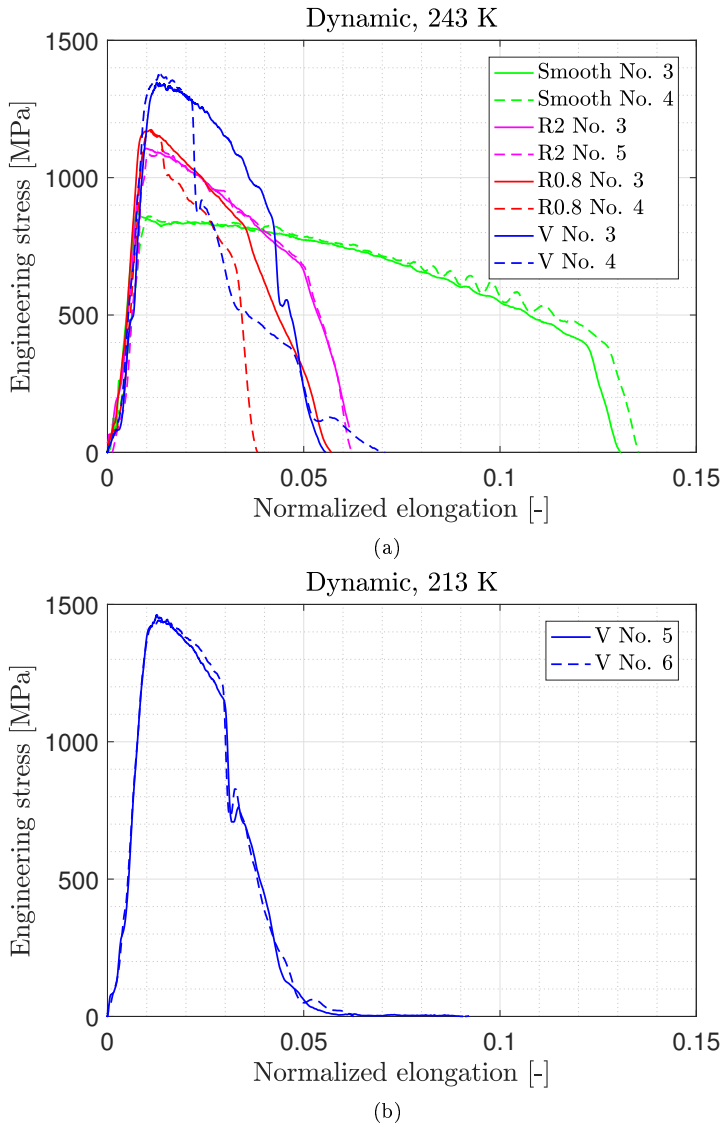


Figure 4.2.7: Engineering stress versus normalized elongation for the dynamic tests at (a) 243 K and (b) 213 K.

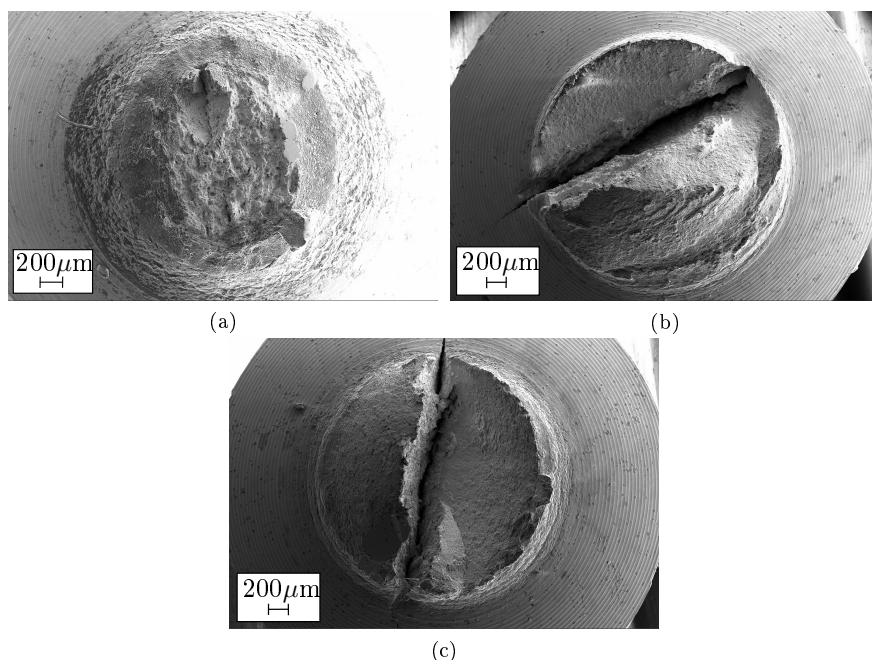


Figure 4.3.1: Overview of the fracture surface of V-notched specimens deformed at: (a) Room temperature, (b) 243 K and (c) 213 K.

### 4.3 Scanning Electron Microscope

Scanning electron microscope (SEM) is a microscope often used to study specimens with rough surfaces. SEM has a good depth of field which makes it a good tool studying the topography of the fracture surface of the specimens.

A brief description of how SEM works is given below. For a more detailed description the reader is referred to the book by Hjelen (1989). The machine sends a focused beam of electrons towards the surface. The electrons interact with atoms in the surface, and various signals are sent back. These signals give information of the surface's chemical composition, topography and crystallography.

In this thesis the topography of some of the specimens was studied to see if the fractures had been ductile, or if it happened due to cleavage. The work was performed by Christian Oen Paulsen at NTNU. He used a Zeiss Gemini SUPRA 55VP. Since the chance of cleavage was expected to be higher at high strain rates, high triaxialities and low temperatures, V-notched specimens from the split Hopkinson tension bar test at 213 K, 243 K and 293 K were studied. Figure 4.3.1 shows an overview of the fracture surfaces of the three specimens studied. The specimens at 243 K and 213 K have a big crack in the direction transverse to the thickness. This type of crack was seen on all the V-notched specimens at 243 K, 213 K and 183 K, and on R0.8 No.4, which was deformed dynamically at 243 K. The reason for



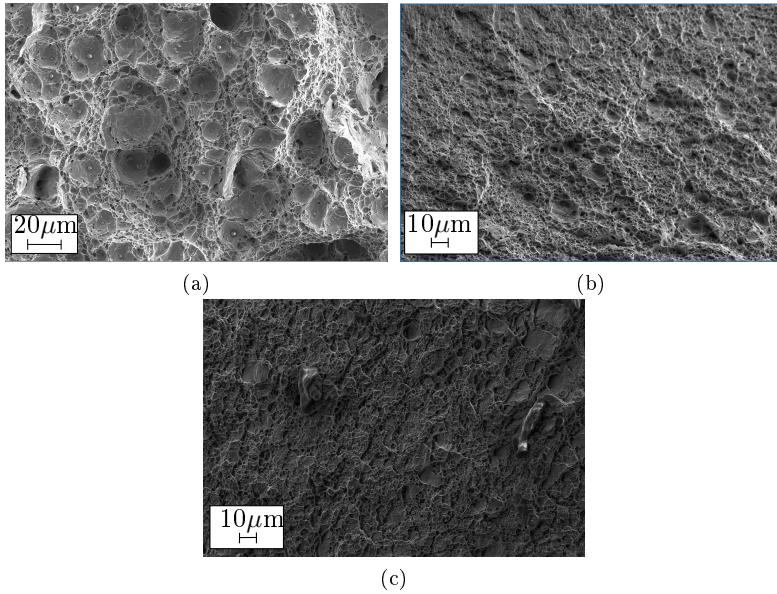


Figure 4.3.2: Fractured surface of V-notched specimens magnified 500x, and deformed at: (a) Room temperature, (b) 243 K and (c) 213 K.

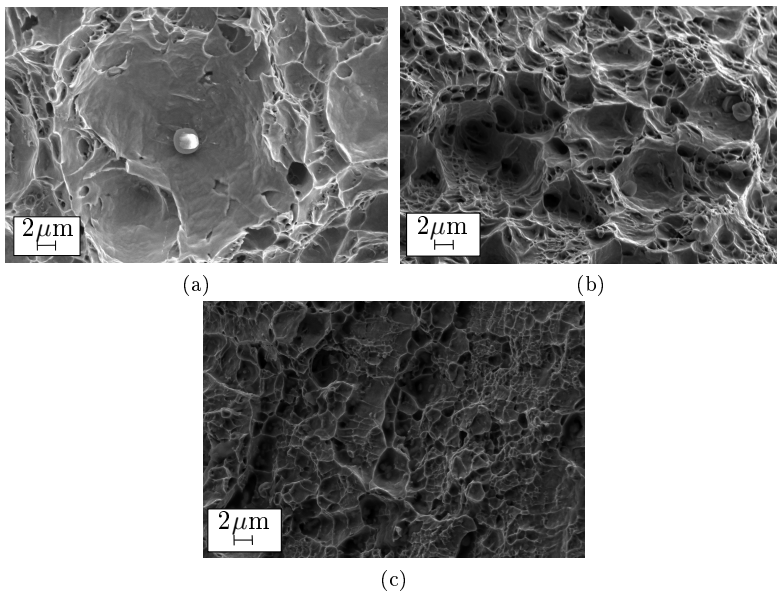


Figure 4.3.3: Fractured surface of V-notched specimens, magnified 2750x, and deformed at: (a) Room temperature, (b) 243 K and (c) 213 K.

this crack is unknown, but a possible reason may be a combination of high stress triaxiality and low ductility.

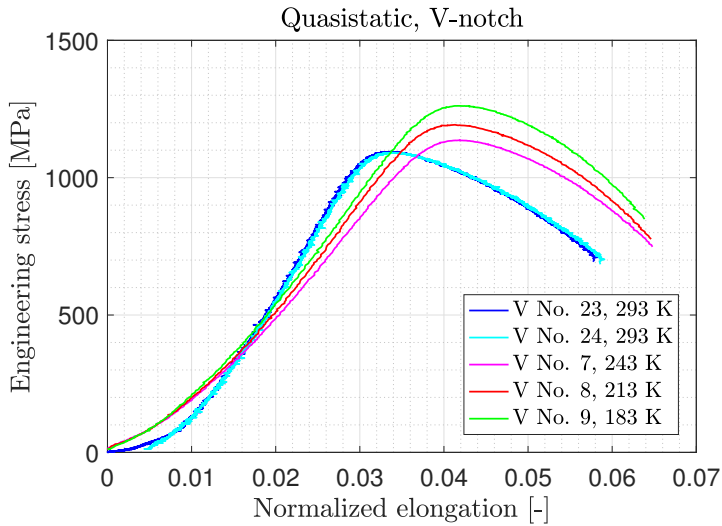
Figure 4.3.2 shows a 500x enlargement of the three specimens. In the picture at room temperature, particles can clearly be seen inside dimples. The pictures for lower temperatures also have dimples, but these have smaller size. Figure 4.3.3 shows the same tendency. Here the specimens is enlarged 2750x. The figure at room temperature shows a big dimple, while the other temperatures has smaller dimples. It seems like the specimen at room temperature has a ductile behaviour, where voids grow and coalesce into bigger voids, resulting in Figure 4.3.3a. The pictures at lower temperatures do not show cleavage, but they show a less ductile behaviour. The surface is still dimpled, but they are much smaller. Here the voids have grown much less before fracture.

## 4.4 Summary and Discussion

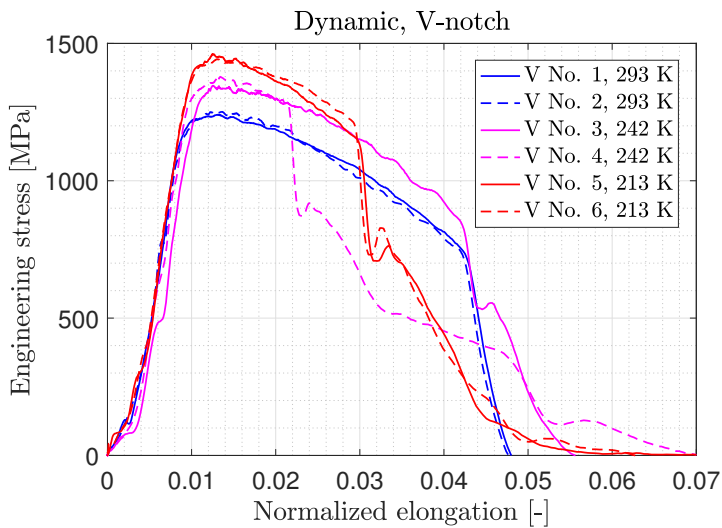
The stress from all the tests had lowest values for the smooth specimen. The specimens with round notches had higher values, and the V-notched even higher. Figure 4.4.1 shows the engineering stress versus normalized elongation for all the V-notched specimens. The initial stiffness of the quasi-static test at room temperature, quasi-static test at lower temperatures and dynamic test are different due to use of different machines and the machine flexibility. From the graphs it is clear that the stress level increases with increasing strain rate and decreasing temperature. Quasi-static tests at 293 K, 243 K, and 213 K have lower maximum stress than the dynamic test at 293 K. The quasi-static test at 183 K has a maximum stress between the maximum stress of a dynamic test at 293 K and 243 K. According to Anderson (2005) the susceptibility to cleavage is enhanced by almost any factor that increases the yield strength. The temperature at a quasi-static test has to be somewhere between 213 K and 184 K to get the same yield strength as a dynamic test. This implies that the strain rate has a greater impact on the susceptibility to cleavage. A combination of low temperature and high strain rate gives an even higher maximum stress.

Figure 4.4.2 shows the fracture strain for all the specimens. These values were found using an optical microscope, and were assumed to be lower than in reality. For low triaxialities, the temperature does not seem to have a considerable impact on the fracture strain. For smooth specimens, one of the dynamic tests at 243 K actually has a higher fracture strain than both dynamic test at 293 K. Based on the figure, it seems like a combination of strain rate, temperature and triaxiality gives the greatest impact. For a dynamic test at 293 K, the difference between R2, R0.8 and V is not that big, but at 243 K the difference is large. When combining all these factors, the results also seem more scattered, which may imply a less ductile behaviour.

Figure 4.4.3, Figure 4.4.4, Figure 4.4.5 and Figure 4.4.6 show the dynamic tests of smooth specimen No.2 (293 K), smooth specimen No.4 (243 K), V No.1 (293 K) and V No.4 (243 K). Both smooth specimens show a ductile behaviour, with a



(a)



(b)

Figure 4.4.1: Engineering stress versus normalized elongation for the V-notched specimens from (a) quasi-static tests and (b) dynamic tests.

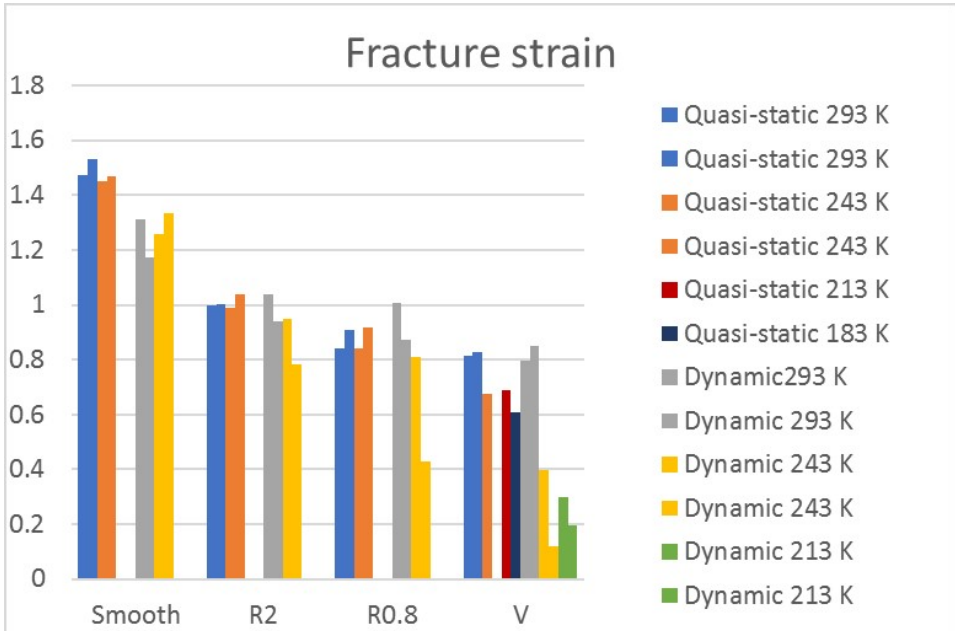


Figure 4.4.2: Fracture strain for all specimens.

high strain. For the V-notched specimens, the effect of the temperate is different. The specimen at 293 K has some more strain, but the fracture is totally different. This fracture is the same type as seen in the SEM-picture in Figure 4.3.1b, and may be due to a combination of low ductility and high triaxiality.

None of the specimens tested failed due to cleavage, but the results show a reduced ductility when combining different factors.

When studying the results, it is important to remember that most of the test were only done with two specimens for each geometry. This gives an idea of how different specimens respond, but if the results are going to be used, more tests have to be done.

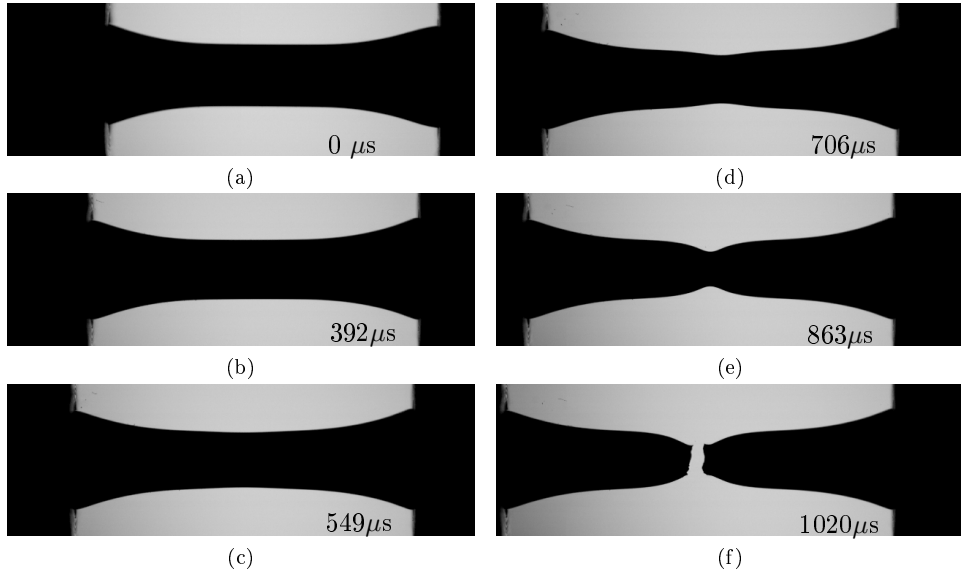


Figure 4.4.3: Pictures from the dynamic test of smooth specimen No.2 at 293 K.

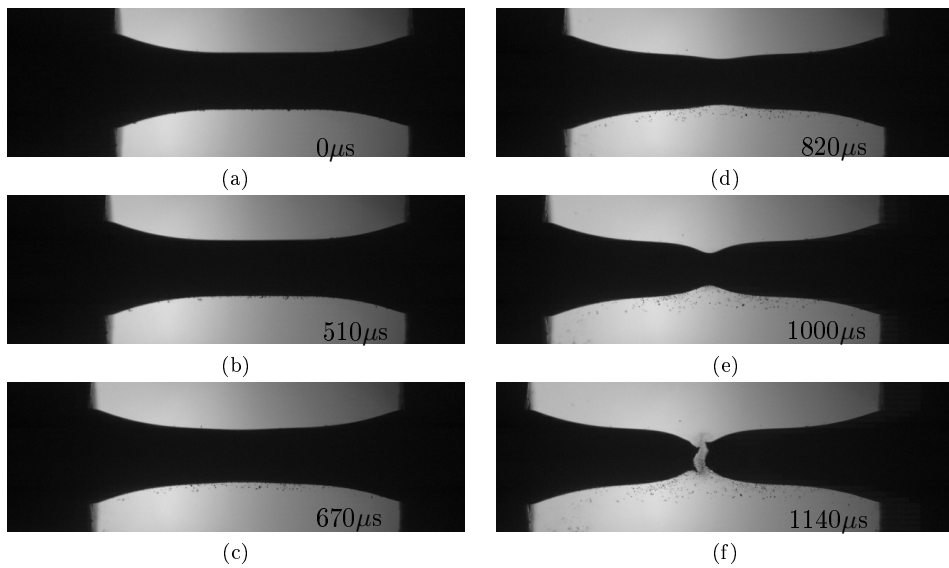


Figure 4.4.4: Pictures from the dynamic test of smooth specimen No.4 at 243 K.

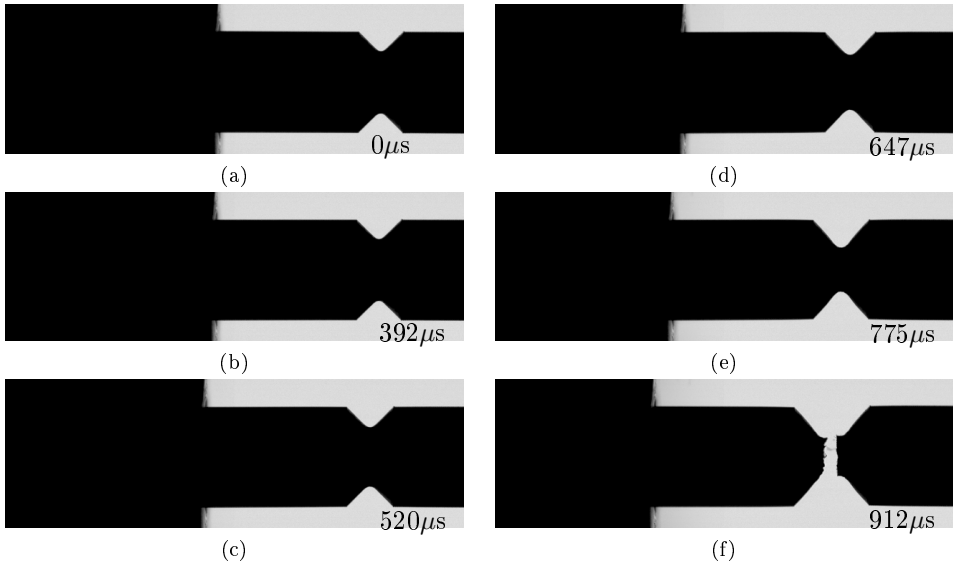


Figure 4.4.5: Pictures from the dynamic test of V No.1 at 293 K.

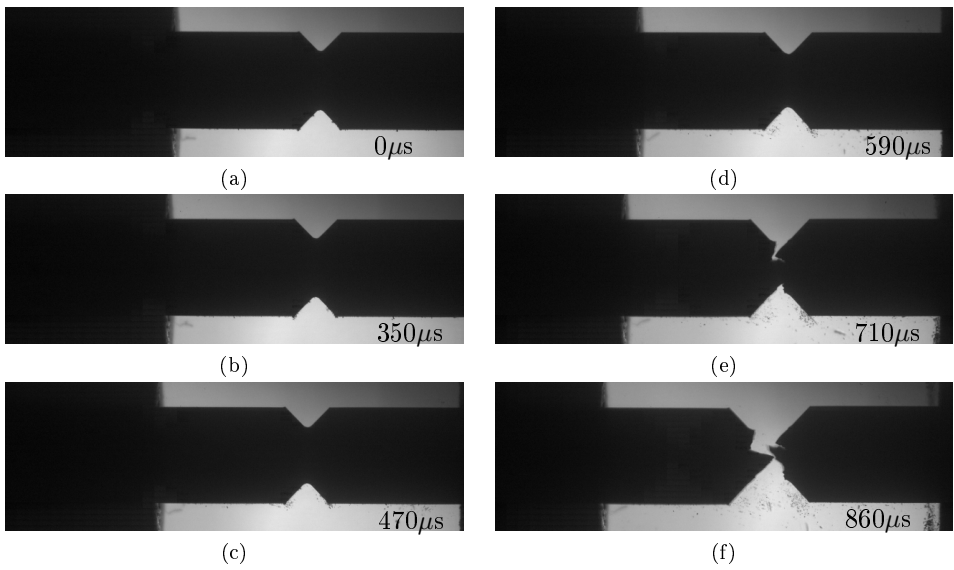


Figure 4.4.6: Pictures from the dynamic test of V No.4 at 243 K.



# NUMERICAL SIMULATIONS

---

## 5.1 Calibrating the Johnson-Cook Material Model

In the preliminary simulations material parameters from the thesis of Kristoffersen (2014) were used. This material was also a X65 steel, but while the yield stress of the material studied in the preliminary simulations was 478 MPa, the results from the experiments in this thesis gave a yield stress of 659 MPa. The materials seemed quite different, and the Johnson-Cook material model was calibrated before further numerical simulations.

### 5.1.1 Strain Hardening Term

When calibrating the strain hardening term, results from the smooth specimens tested under quasi-static conditions at room temperature were needed. The two tests gave quite similar results, and the results of specimen No.10 were used.

In order to calibrate the Johnson-Cook material model, the equivalent plastic strain  $p$  and the equivalent stress  $\sigma_{eq}$  were needed. The equivalent plastic strain is equal to the logarithmic plastic strain  $\varepsilon_l^p$  during uniaxial tension. This gives the relation:

$$p = \varepsilon_l^p = \varepsilon_l - \frac{\sigma_t}{E} \quad (5.1.1)$$

Due to the neck in the gauge area during the experiment, the longitudinal true stress was not equal to the equivalent stress. Bridgman-Le Roy correction were used to get the the equivalent stress after necking. This correction is explained in section 2.1.3. The true stress and the Bridgman-Le Roy corrected equivalent stress are compared in Figure 5.1.1a. From the figure, it is clear that the triaxial stress conditions at the neck increase the measured stress levels compared to the equivalent stress.

The Johnson-Cook model was calibrated from the Bridgman-Le Roy corrected equivalent stress. Since the specimen was deformed under quasi-static conditions, the strain rate dependent term of the Johnson-Cook model could be neglected. The reference temperature was set to room temperature which led to the Johnson cook material model being given by:

$$\sigma_{eq} = A + Bp^n \quad (5.1.2)$$



## 5.1. Calibrating the Johnson-Cook Material Model

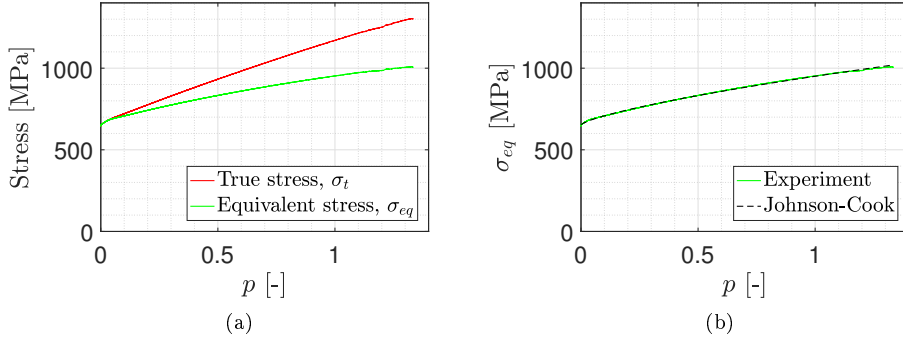


Figure 5.1.1: Curves comparing: (a) the true stress and the Bridgman-Le Roy corrected equivalent stress (b) the equivalent stress and the Johnson-Cook model.

Table 5.1.1: Material constants for the strain hardening term of Johnson-Cooks material model.

$A$ [MPa]	$B$ [MPa]	$n$ [-]
652.5	297.8	0.7281

The parameters  $A$ ,  $B$  and  $n$  are given in Table 5.1.1 and were found in Excel using problem solver to find a least square fit. Figure 5.1.1b shows the fitted Johnson-Cook curve along with the experimental curve.

To test the material parameters, they were used in the implicit smooth Abaqus model from the preliminary simulations. The force in the end and the diameter at the neck were used to find the true stress and logarithmic strain. In Figure 5.1.2 the true stress versus logarithmic strain from the experiment are compared with the values from Abaqus. These values are very close, but there are some differences for higher strains. This may be due to weak points or damages in the specimens.

### 5.1.2 Strain Rate Sensitivity Constant

When finding the strain rate sensitivity constant  $C$ , the results from the high strain rate tests at room temperature and the quasi-static result of smooth specimen No.10 were used. To make the quasi-static and dynamic results comparable, the true stress and strain from smooth specimen No.10 were converted to engineering values. The temperature dependent term of the Johnson-Cook model was neglected since the tests were done at room temperature. The term remaining could be written as:

$$\sigma_{dynamic} = \sigma_{quasi-static} \times (1 + C \ln \dot{p}^*) \quad (5.1.3)$$

Where  $\dot{p}^* = \dot{p}/\dot{p}_0$ . The reference strain rate was set to  $10^{-3} s^{-1}$ , and  $\dot{p}$  was set to the average true strain rate for the dynamic test.  $C$  was calculated for both the dynamic tests, smooth No.1 and smooth No.2. For smooth No.1,  $\sigma_{dynamic}$  was set

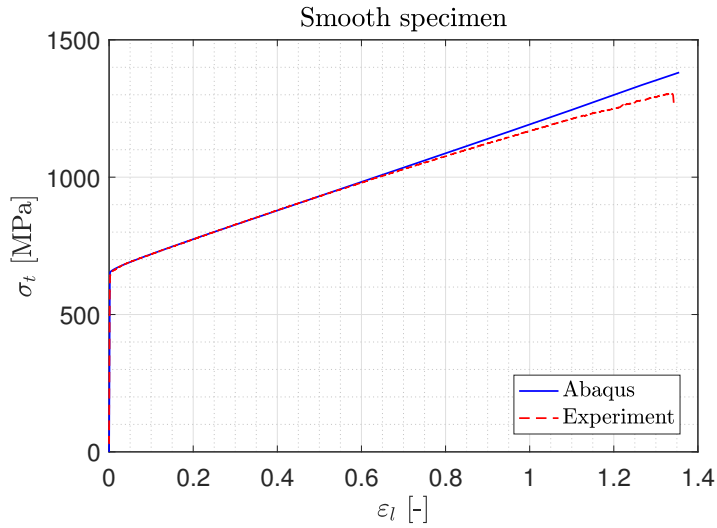


Figure 5.1.2: True stress versus logarithmic strain from the experiment and the numerical simulation of the smooth specimen under quasi-static deformation.

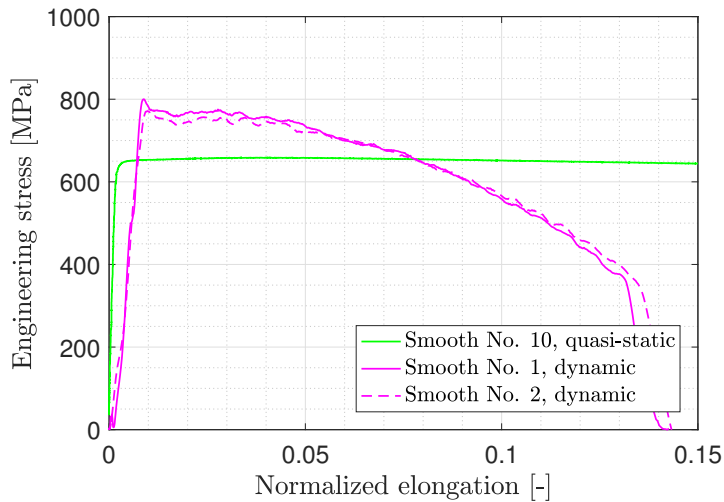


Figure 5.1.3: Curves used to find  $\sigma_{dynamic}$  and  $\sigma_{quasi-static}$ .

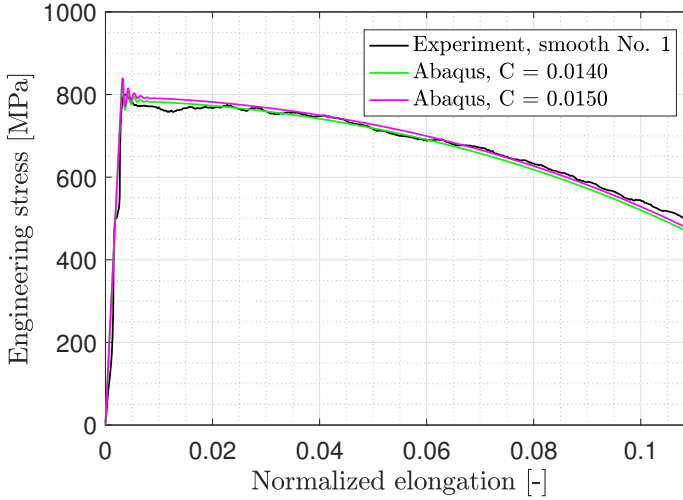


Figure 5.1.4: Experimental results compared to the numerical results with  $C = 0.0140$  and  $C = 0.0150$

to the maximum stress of smooth No.1, see Figure 5.1.3, while  $\sigma_{quasi-static}$  was set to the value of smooth No.10 at the same elongation. Solving the equation for  $C$  gave  $C_1 = 0.184$ . Doing the same for smooth specimen No.2 gave  $C_2 = 0.0148$ . A parameterstudy was done in Abaqus to see which values of  $C$  that gave the results that were closest to smooth specimen No.1. Force and displacement of the end of the specimen were taken from the results of the simulations and converted into engineering stress and normalized elongation in the same way as the dynamic experiments. To make the results comparable with the experimental results, the Young's modulus of the experimental results was adjusted to the numerical results with the formula:

$$\varepsilon_c = (\varepsilon_m - \Delta\varepsilon) - \left( \frac{E_c - E_m}{E_c E_m} \right) \sigma \quad (5.1.4)$$

where  $c$  represents the corrected values,  $m$  the measured values and  $\Delta\varepsilon$  is the difference in normalized elongation at  $\sigma = 0$ . The parameter study indicated that the stress values are lifted when the value of  $C$  is higher. Values around 0.0140 and 0.0150 gave results close to the experiment, see Figure 5.1.4.  $C$  was chosen to be 0.0150.

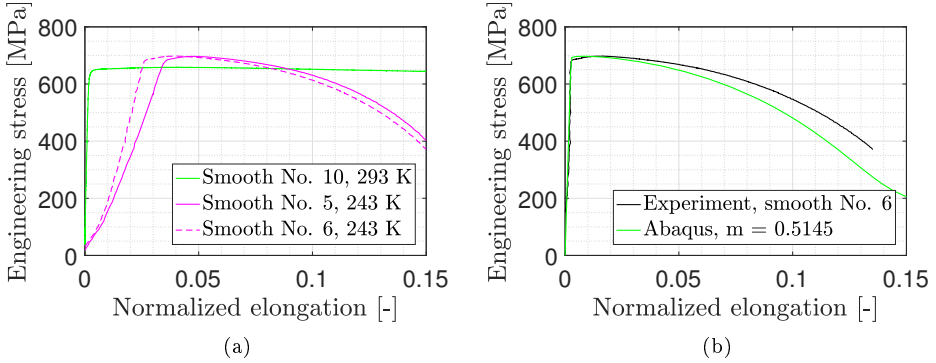


Figure 5.1.5: (a) Curves used to find  $\sigma_{243}$  and  $\sigma_{293}$ . (b) Experimental results compared to the numerical results where  $m = 0.5145$ .

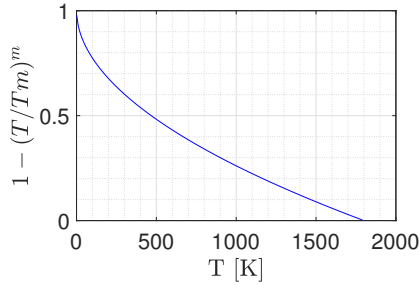


Figure 5.1.6: Value of the temperature dependent term for different temperatures when the reference temperature is 0 K and  $m = 0.5145$ .

### 5.1.3 Temperature Sensitivity Constant

When deciding the temperature sensitivity constant  $m$ , data from quasi-static tests at room temperature and 243 K were used, see Figure 5.1.5a. As a result of this, the strain rate sensitive term in the Johnson-Cook material model could be neglected. The reference temperature was now set to zero. By dividing the maximum stress at 243 K by the stress at room temperature for the same elongation, the following equation was obtained:

$$\frac{\sigma_{243}}{\sigma_{293}} = \frac{A + Bp^n}{A + Bp^n} \times \frac{1 - (243/T_m)^m}{1 - (293/T_m)^m} \quad (5.1.5)$$

The strain hardening term was the same for both temperatures, and could be neglected. By inserting the values of  $\sigma_{243}$ ,  $\sigma_{293}$  and  $T_m = 1800$  K, the temperature sensitivity constant became 0.523 for smooth specimen No.5 and 0.506 for No.6. The average of these values was  $m = 0.5145$ .

The new value of the temperature sensitivity constant led to the values of the temperature dependent term shown in Figure 5.1.6. The term is 1 at 0 K, 0.643 at

243 K and 0.607 at 293 K. Since the reference temperature was set to 0 K to find  $m$ ,  $A$  and  $B$  had to be calibrated for the new reference temperature. To do this, the values found from the quasi-static test at room temperature had to be divided by the temperature dependent term at room temperature:

$$A = \frac{A_{293}}{1 - (293/T_m)^m} = 1074.9 \quad B = \frac{B_{293}}{1 - (293/T_m)^m} = 490.66 \quad (5.1.6)$$

The temperature sensitivity constant was tested by inserting it and the new values of  $A$  and  $B$  in Abaqus, and running an implicit analysis at 243 K. The force and the displacement at the end of the specimen were used to find the engineering stress and normalized elongation in the same way as in the experiment. Young's modulus of the experiment was adjusted in the same way as when testing the strain rate sensitivity constant. A comparison of the experiment and the numerical simulation is shown in Figure 5.1.5b. The curves have approximately the same maximum stress, but do not look exactly alike. This may be because the results were taken from the machine and not from an extensometer or by using edge-tracing.

## 5.2 Simulations

In this section, numerical simulations were performed on models representing smooth, R2, R0.8 and V-notched specimens. The Abaqus models from section 3.1 were used with some exceptions. The Johnson-Cook material parameters found in section 5.1 were used, and no fracture criteria was added. Simulations were also performed at 243 K for all specimens, at 213 K for the V-notched specimens and at 183 K for a V-notched specimen.

In the first part of the simulations the results from the experiments and the numerical simulations were compared. The second part studied the Cockcroft-Latham damage, the stress intensification and the stress triaxiality of the different specimens.

### 5.2.1 Results and discussion

#### Comparison between experimental and numerical results

Figure 5.2.1 shows the true stress versus logarithmic strain for the numerical simulations and experimental work. The graphs from the simulations were cut at approximately the same strain as the fracture strain of the experimental graphs. For the graphs of the smooth specimen and R2, the results from the simulations and the experiments are almost identical. For R0.8 and the V-notch, the results from the simulations have higher strain values than in the experiments.

The rest of the figures in this section show engineering stress versus normalized elongation for the numerical simulations and experimental work. To make the results comparable with the experimental results, the Young's modulus of the experimental results was adjusted in the same way as in section 5.1.2.

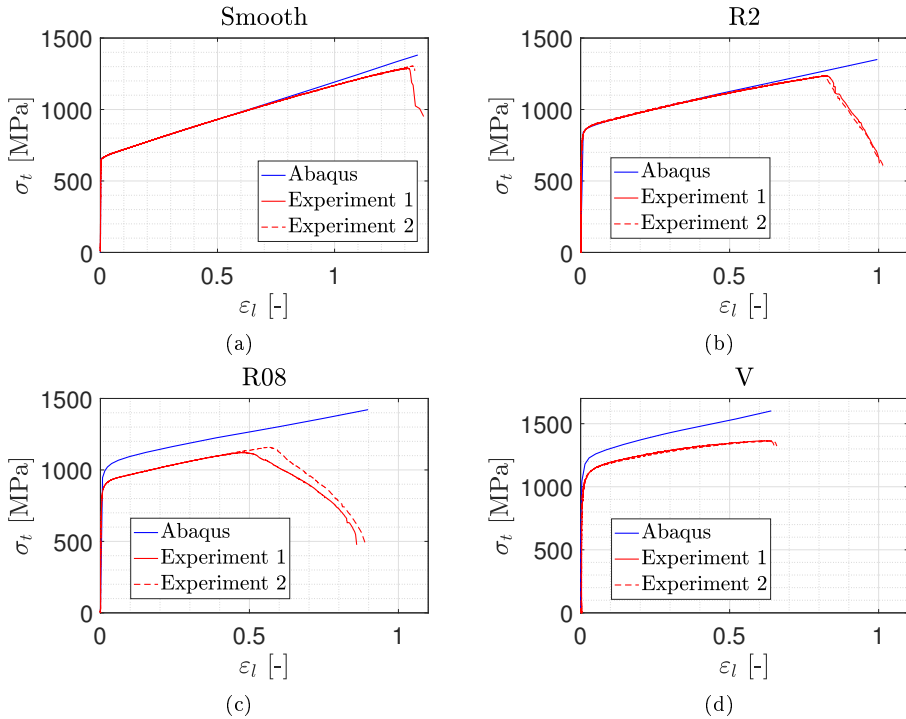


Figure 5.2.1: True stress versus logarithmic strain from the quasi-static experiments and the numerical simulations at 293 K for the test specimens: (a) smooth, (b) R2, (c) R08 and (d) V.

Figure 5.2.2 shows the results of the quasi-static simulations at 243 K, while Figure 5.2.3 shows the results for the V-notched specimens at 213 K and 183 K. The dynamic results at 293 K are in Figure 5.2.4, at 243 K in Figure 5.2.5 and at 213 K in Figure 5.2.6. All the simulations of the smooth specimen and R2 have approximately the same maximum stress as the experiments. R0.8 and the V-notch have higher stress values than the experiments for all the simulations.

A reason for this overestimation may be that the numerical simulations were done using von Mises yield criterion. R0.8 and The V-notch has high hydrostatic stress values, but Von Mises is independent of hydrostatic stress. This may be one of the reasons that the simulations started yielding at higher stress values than the corresponding experiments.

## 5.2. Simulations

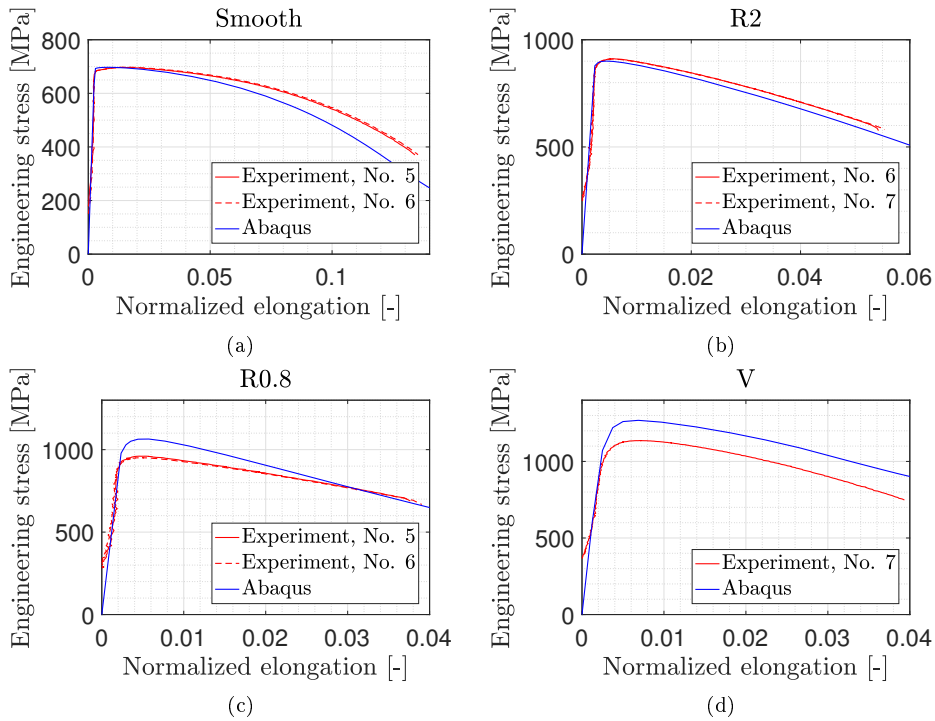


Figure 5.2.2: Engineering stress versus normalized elongation from the quasi-static experiments and numerical simulations at 243 K for the test specimens: (a) Smooth, (b) R2, (c) R08 and (d) V.

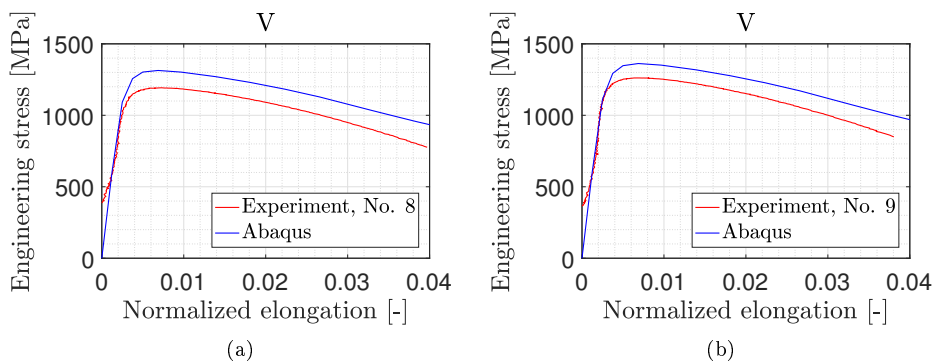


Figure 5.2.3: Engineering stress versus normalized elongation from the quasi-static experiments and numerical simulations for V-notched specimens at (a) 213 K and (b) 183 K

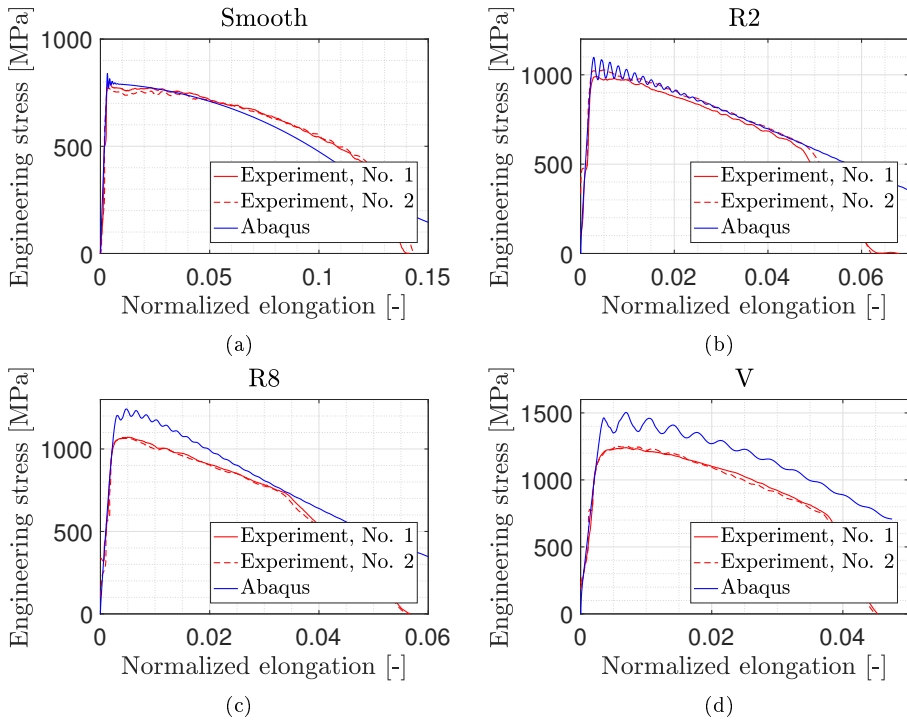


Figure 5.2.4: Engineering stress versus normalized elongation from the dynamic experiments and numerical simulations at 293 K for the test specimens: (a) Smooth, (b) R2, (c) R08 and (d) V.



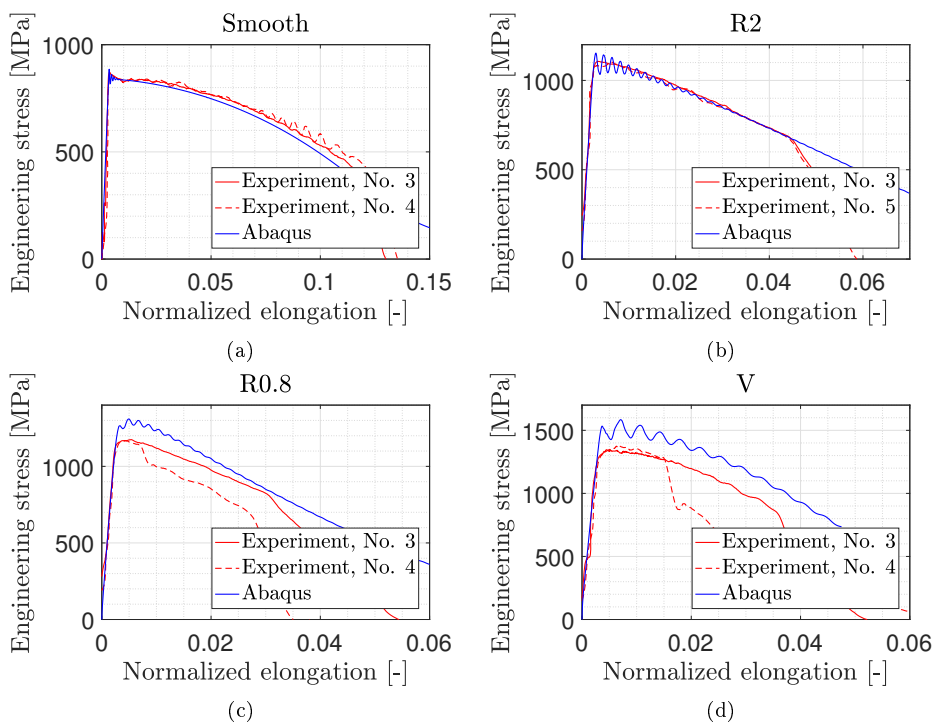


Figure 5.2.5: Engineering stress versus normalized elongation from the dynamic experiments and numerical simulations at 243 K for the test specimens: (a) Smooth, (b) R2, (c) R08 and (d) V.

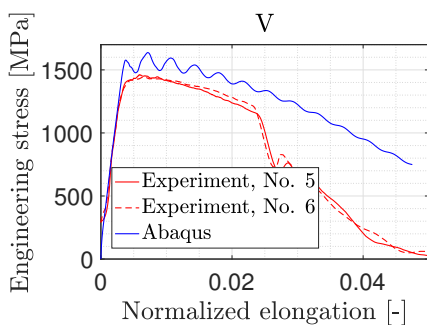


Figure 5.2.6: Engineering stress versus normalized elongation from the dynamic experiments and numerical simulations at 213 K for a V-notched specimen.

**Damage, stress intensification and stress triaxiality**

In this section, the Cockcroft-Latham damage  $D = W/W_c$ , the stress intensification  $R = \sigma_1/\sigma_0$  and the stress triaxiality  $\sigma^* = \sigma_H/\sigma_{eq}$  were studied. The values were found in element 1, at the middle of the cross-section of the specimens. The obtained  $R$ -values may be higher than in reality for R0.8 and the V-notch, since Abaqus overestimated their stress levels, and  $\sigma_0$  was found from the experiments.

$W_c$  is the plastic work to failure using the maximum principal stress. It was found using the principal stress from the simulations. The failure strain was not found for all the experiments, so the fracture strain found using optical microscope was used instead. Since the elastic strain of the specimens was so low, it was not subtracted from the fracture strain.

The results are shown in Figure 5.2.7 (293 K), Figure 5.2.8 (243 K) and Figure 5.2.9 (213 K and 183 K). The curves are stopped at the fracture strain, where  $D = 1$ . The stress intensification factor  $R$  shows the same tendencies as in section 3.1.5, where the value increases for high strain rate and high stress triaxiality. For the smooth specimen at 293 K,  $R$  is higher at the quasi-static simulation due to higher strain before fracture.  $R$  in this section is lower than in section 3.1.5 due to new material properties. In this section the maximum value of  $R$  is 3.4. This value is obtained at a dynamic simulation at 213 K of a V-notched specimen. Since none of the specimens obtained cleavage, it is clear that  $R_{max}$  is higher than 3.4.

The triaxiality also varies in the same way as in 3.1.5. The temperature do not have a great impact on the triaxiality, and the highest triaxiality was obtained for a V-notch at a dynamic simulation, and had the value 1.76.

## 5.2. Simulations

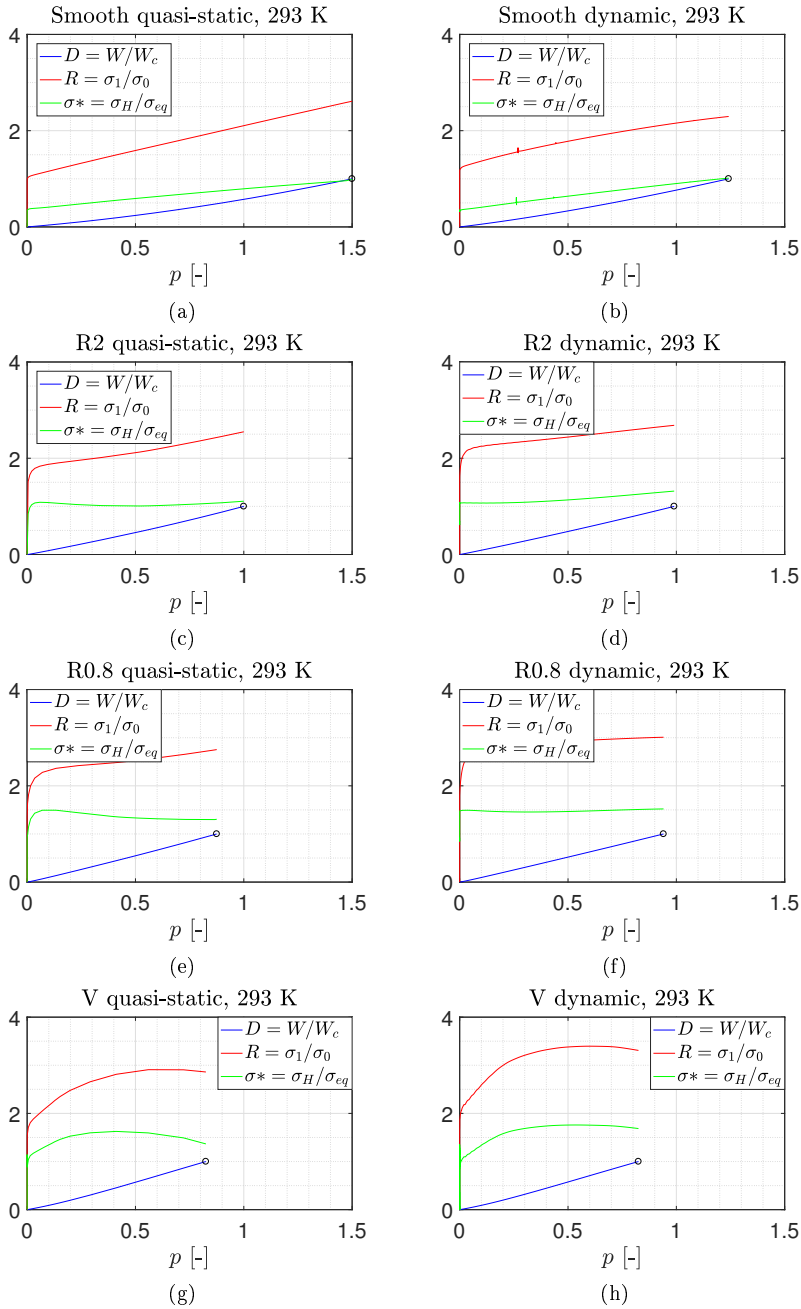


Figure 5.2.7: Damage, stress intensification and stress triaxiality for the quasi-static and dynamic simulations at 293 K.

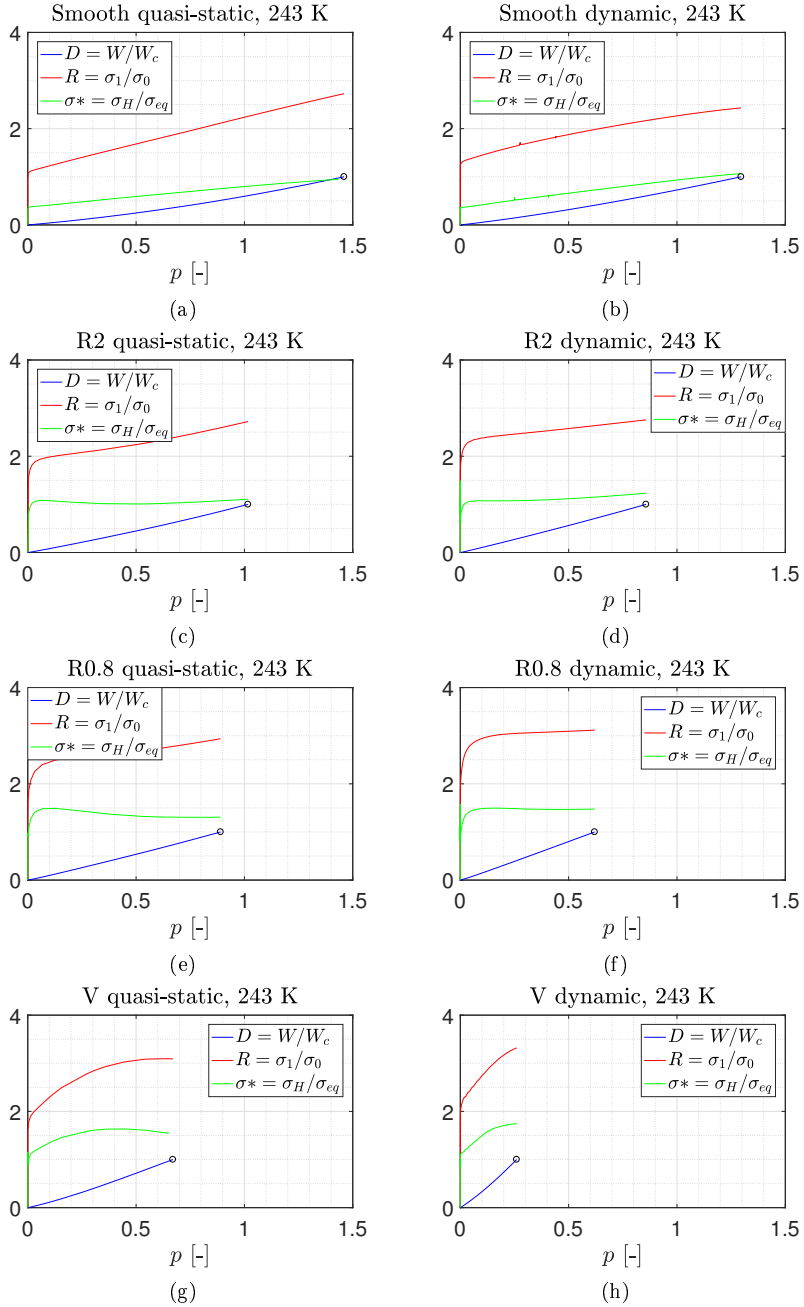


Figure 5.2.8: Damage, stress intensification and stress triaxiality for the quasi-static and dynamic simulations at 243 K.

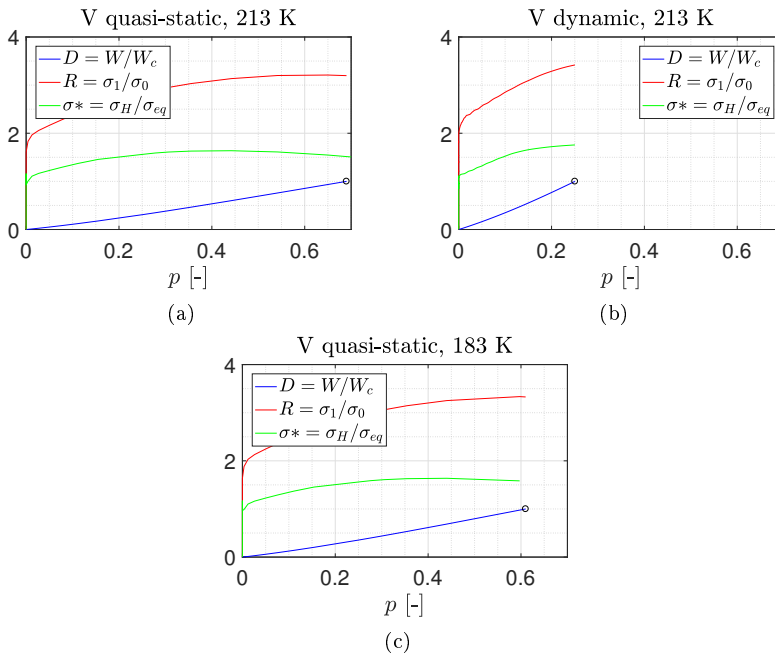


Figure 5.2.9: Damage, stress intensification and stress triaxiality for the quasi-static and dynamic simulations at 213 K and 183 K.

# CONCLUDING REMARKS

---

## 6.1 Summary and Conclusions

This chapter summarises the most important results and states the conclusions of this study.

### Preliminary simulations

In the first part of the preliminary simulations, Abaqus models simulating tension tests were made. Material parameters expected to have the same properties as the material of the thesis were used. Different geometries of test specimens were made to obtain different states of stress triaxiality. The results showed as expected that the smooth specimens had the lowest values of triaxiality. The specimens with round notches had higher values, and smaller notch radius led to higher triaxiality. The specimens with sharp notches had the highest values. The effect of triaxiality could therefore be studied by using different specimens.

The stress intensification  $R = \sigma_1/\sigma_0$  was plotted for each specimen.  $\sigma_1$  and  $\sigma_0$  were found using Abaqus. Brittle fracture was assumed to happen if  $R$  reached the maximum stress intensification  $R_{max}$ . If  $R_{max}$  was set to 5, brittle fracture was expected to happen for all sharp-notched specimens in the dynamic tension tests. Due to manufacturing reasons, it was decided to use specimens with notches of angle  $\alpha = 45^\circ$  (meaning a notch-angle of  $90^\circ$ ) as the specimens representing high triaxiality in the experimental work.

In the second part of the preliminary simulations a MATLAB model implemented with the Johnson-Cook material model, the Cockcroft-Latham failure criterion and the Ritchie-Knott-Rice brittle fracture criterion was made. Here the stress triaxiality, strain rate and maximum stress intensification were varied to see how this affected the ductile to brittle transition temperature. As expected, higher stress triaxiality, higher strain rates and lower maximum stress intensification led to higher transition temperatures. Due to a bad choice of parameters for the basic model, it was difficult to compare the results with the numerical simulations. The results did show that the transition would happen for triaxialities between 1.6 and 2.3, and that the transition temperature was expected to be higher than  $-50^\circ\text{C}$  for a dynamic test of a sharp-notched specimen.

### Experimental work

The experimental work was performed with smooth specimens, specimens with round notches of radii 2.0 mm and 0.8 mm and a sharp-notched specimen. Quasi-static tension tests were performed at room temperature,  $-30^{\circ}\text{C}$ ,  $-60^{\circ}\text{C}$  and  $-90^{\circ}\text{C}$ . Dynamic tests were done using split-Hopkinson tension bar at room temperature,  $-30^{\circ}\text{C}$  and  $-60^{\circ}\text{C}$ . It turned out that the material had a higher yield stress than the material from the preliminary simulations. Cleavage did not happen in any of the test even though the preliminary simulations predicted cleavage. It is assumed that this is because of different material properties.

Even though cleavage did not occur, different fracture strains were obtained for different tests. As expected higher stress triaxiality, higher strain rate and lower temperature led to less ductility. Stress triaxiality seemed to have the greatest impact on the ductility. When combining the factors, interaction effects seemed to give a major addition to the reduction of ductility.

### Numerical work

The Johnson-Cook material model was calibrated from the test data. Simulations with the new material properties were run using Abaqus, and compared with the experimental work. The results showed that the Johnson Cook-material model was able to produce the same results as in the experiments for the smooth specimen and R2. The model overestimated the stress level for R0.8 and the V-notch. This may be because of the high values of hydrostatic stress in the notches. The Abaqus model used von Mises yield criterion. This criterion is independent of hydrostatic stress, which may have led to yield at higher stress values.

Graphs with stress triaxiality, Cockcroft-Latham failure criterion and Ritchie-Knott-Rice fracture criterion were made. The triaxiality showed the same trends as in the preliminary simulations, but the highest triaxiality had a value of 1.76. The stress intensification also showed the same tendencies, but the values were much lower. Here the highest stress intensification obtained was 3.4. Since the maximum stress intensification leading to cleavage was unknown, it is difficult to know how close the specimens from the experiments were to obtain cleavage. The ductility is clearly reduced for high triaxiality, high strain rate and low temperature, but further work is needed to find the maximum stress intensification, and to study the ductile to brittle transition of this material.

From the results, it is clear that if some of the specimens from this thesis are going to obtain cleavage, it is the notched specimen at a high strain rate, and a lower temperature. The studies show that the triaxiality has a great impact on the ductility. A fatigue crack would lead to a higher triaxiality, and may be a good way to initiate cleavage.

## 6.2 Further Work

Based on the results of this thesis, the following work is suggested:

- Perform edge-tracing on the results that are lacking the values of true stress and logarithmic strain.
- Dynamic tests of the V-notched specimens at lower temperatures.
- Tests of specimens with fatigue cracks at different strain rates and different temperatures.
- Performing a study in the MATLAB script, where the correct material parameters are inserted.
- Simulations in Abaqus with other geometries, to find a geometry that gives higher stress intensification.
- Simulations in Abaqus with Drucker-Prager yield criterion, to take into consideration the effect of hydrostatic stress.





# BIBLIOGRAPHY

---

- Anderson, T. (2005). *Fracture mechanics: fundamentals and applications*. CRC press, third edition.
- Bridgman, P. (1944). *Trans. Am. Soc. Met.*, 32:553.
- Cockcroft, M. and Latham, D. (1968). Ductility and the workability of metals. *Journal of the Institute of Metals*, 96(1):33–39.
- Dieter, G. (1988). *Fracture mechanics: fundamentals and applications*. McGraw-Hill Book Company.
- Hjelen, J. (1989). *Scanning electron-microskopi*. Metallurgisk institutt, NTH.
- Hopperstad, O. and Børvik, T. (2015). *Material Mechanics*.
- Hopperstad, O. and Børvik, T. (2017). *Impact Mechanics - Part 1: Modelling of plasticity and failure with explicit FEM*.
- Johnson, G. and Cook, W. (1983). A constitutive model and data for metals subjected to large strains, high strain rates and high temperatures. *Proceedings of the 7th International Symposium on Ballistics*, pages 541–547.
- Johnson, G. and Cook, W. (1985). Fracture characteristics of three metals subjected to various strains, strain rates, temperatures and pressures. *Engineering fracture mechanics*, 21(1):31–48.
- Kristoffersen, M. (2014). *Impact against X65 offshore pipelines*. PhD thesis, Norwegian University of Science and Technology.
- Langseth, M., Clausen, A., and Børvik, T. (2016). *Lecture Notes in TKT4128, Impact Mechanics: Impact and Energy Absorption*. SIMLab/Department of Structural Engineering, Norwegian University of Science and Technology.
- Le Roy, G., Embury, J., Edwards, G., and Ashby, M. (1981). A model of ductile fracture based on the nucleation and growth of voids. *Acta Metallurgica*, 29(8):1509–1522.
- Mescall, J. and Weiss, V. (1983). *Material behaviour under high stress and ultrahigh loading rates*, volume 29. Plenum Press, New York.

## Bibliography

---

- Petroleumstilsynet (2017). Rørledningsskader - skader og hendelser fra petroleumstilsynets codam database. <http://www.psa.no/getfile.php/1343764/PDF/Roerledningsskader> Obtained in June 2017.
- Ritchie, R., Knott, J., and Rice, J. (1973). On the relationship between critical tensile stress and fracture toughness in mild steel. *J. Mech. Phys. Solids*, 21:395–410.
- Roth, C. and Mohr, D. (2014). Effect of strain rate on ductile fracture initiation in advanced high strength steel sheets: Experiments and modeling. *International Journal of Plasticity*, 56:19–44.

APPENDIX **A**  
**APPENDIX**

---

## **A.1 Analytical MATLAB Model**

Figure A.1.1 and Figure A.1.2 show the MATLAB script from section 3.2.1.

## A.1. Analytical MATLAB Model

---

```

close all; clear all; clc;

%% MODEL CONSTANTS
sigma0 = 465.5; % Yield stress [MPa]
B = 410.8; % Constant of Johnson-Cook Material model [MPa]
n = 0.4793; % Constant of Johnson-Cook Material model [-]
C = 0.0104; % Strain rate sensitivity constant [-]
p0dot = 8.06e-4; % Reference strain rate [s^-1]
m = 1; % Temperature sensitivity constant [-]
Tm = 1800; % Melting temperature [K]
T0 = 0; % Reference temperature [K]
rho = 7.8e-9; % Density [ton/mm^3]
c = 452e6; % Heat capacity [mm^2/s^2*K]
Wc = 1562; % Cockcroft-Latham fracture parameter [Nmm/mm^3]
Lode = -1; % Lode parameter [-]
pdot_iso = 10; % Isothermal limit strain rate [s^-1]
pdot_ad = 10^2; % Adiabatic limit strain rate [s^-1]
beta = 0.9; % Taylor-Quinney coefficient [-]

%% CALIBRATING A
Tr = 293;
A = sigma0 / ( 1 - ( (Tr - T0)/(Tm - T0)^m));
sigma_cr = 4*A;

%% VECTORS
pdot = [1e-3 1e-2 1e-1 1 1e1:1e2 1e3]; % Strain rate
T = [0 40 80 120 160 200 213 233 253 273 293]; % Temperature
sigma_tri = [1/3 2/3 1 3/2 3]; % Triaxiality
p = [0 : 0.001 : 2.5]; % Equivalent plastic strain
I = length(p);
K = length(T);
J = length(pdot);
L = length(sigma_tri);
sigma_eq = zeros(I,J,K); % Equivalent stress
T_ad = zeros(I,J,K); % Temperature increase due to adiabatic
heating
w = zeros(I,J,K,L); % Cockcroft-Latham damage
pf_ductile = zeros(J,K,L); % Gives p at ductile fracture
pf_brittle = zeros(J,K,L); % Gives p at ductile fracture
pf_brittle(pf_brittle == 0) = NaN;
pf_ductile(pf_ductile == 0) = NaN;

% sigma_l(I,j,k,l) is the maximum principal stress
% v(j) is the weighting function (Roth and Mohr, 2014)

%% LOOPS
for l = 1 : L % loop over triaxiality
for k = 1 : K % loop over temperature
for j = 1 : J % loop over strain rate
for i = 1 : I-1 % loop over equivalent strain

T_ad(1,j,k) = T(k);

sigma_eq(1,j,k) = (A+B.*p(1)^n)*(1+C*log(pdot(j)/p0dot))*(1-((T(k)-T0)/(Tm-T0))^m);

if pdot(j) < pdot_iso % Isothermal condition
v(j) = 0;

elseif pdot(j) >= pdot_iso && pdot(j) <= pdot_ad % Transition zone

v(j) = ((pdot(j)-pdot_iso)^2*(3*pdot_ad-2*pdot(j)-pdot_iso))/((pdot_ad -
pdot_iso)^3);

else % Adiabatic condition
v(j) = 1;
end

```

Figure A.1.1: MATLAB model, part 1

```

sigma_eq(i+1,j,k)=(A+B*p(i+1)^n)*(1+C*log(pdot(j)/p0dot))* (1-((T_ad(i,j,k)-T0)/(Tm-
T0))^m);
T_ad(i+1,j,k)=T_ad(i,j,k)+0.5*(betta*v(j)/(c*rho))*(sigma_eq(i+1,j,k)+sigma_eq(i,j,k))*
(p(i+1)-p(i));
sigma_1(1,j,k,l) = (sigma_tri(1)+((3-Lode)/(3*sqrt(3+Lode^2))))* sigma_eq(1,j,k);
sigma_1(i+1,j,k,l)= (sigma_tri(1)+((3-Lode)/(3*sqrt(3+Lode^2))))* sigma_eq(i+1,j,k);
w(i+1,j,k,l)=w(i,j,k,l)+(1/(2*Wc))*max((sigma_tri(1)+((3-Lode)/(3*sqrt(3+Lode^2))))
),0)*(sigma_eq(i+1,j,k)+sigma_eq(i,j,k))* (p(i+1)-p(i));

if w(i,j,k,l) == 1 % Ductile failure
    pf_ductile(j,k,l) = p(i);
elseif w(i,j,k,l) < 1 && w(i+1,j,k,l) > 1
    pf_ductile(j,k,l) = 0.5*(p(i) + p(i+1));
end

if sigma_1(i,j,k,l) == sigma_cr % Brittle failure
    pf_brittle(j,k,l) = p(i);
elseif sigma_1(i,j,k,l) < sigma_cr && sigma_1(i+1,j,k,l) > sigma_cr
    pf_brittle(j,k,l) = 0.5*(p(i) + p(i+1));
elseif sigma_1(1,j,k,l) > sigma_cr
    pf_brittle(j,k,l) = 0;
end
end
end
end
end

```

Figure A.1.2: MATLAB model part 2